EXPERIMENTAL AND THEORETICAL INVESTIGATIONS ON THE GENERAL FLOW PATTERNS IN AXIAL FLOW COMPRESSORS

Thesis by

Rolf Heinrich Sabersky

In Partial Fulfillment of the Requirements

For the Degree of

Doctor of Philosophy

California Institute of Technology

Pasadena, California

1949

Acknowledgment

It is with great pleasure that the writer welcomes this opportunity to express his gratitude to, and deep respect for Professor W. D. Rannie. Through his continued interest in the writer's work and through his own high scientific standards, he has influenced in a most important way the writer's progress during his graduate studies at the California Institute of Technology.

The writer also wishes to thank Mr. J. T. Bowen for the pleasant years of cooperation and for the very fruitful exchange of ideas concerning the research as well as general scientific problems. Thanks is also due to Messrs. L. J. Downs, T. Linton, and T. Taniguchi for their untiring assistance in all phases of the project.

Furthermore, the writer wishes to acknowledge gratefully the support of the Office of Naval Research, under whose auspices the research was conducted.

ABSTRACT

1. An axial flow compressor and the corresponding test facilities including instrumentation have been designed and constructed. The compressor has a blade tip diameter of 36 inches, is designed for a top speed of 2000 rpm, and is powered by a 125 hp dynamometer. The unit is in operation and has been used extensively for the experiments of this thesis.

2. A number of blade types were designed, all having the same overall performance. Criteria were established characterizing the individual properties of each type and a comparison was made on this basis. It was shown that some of these blade types are often more suitable than the "free vortex" blading which is most commonly used at present.

3. Two sets of blades were constructed, the types having been selected from the blade study. Single stage experiments were carried out with each type and detailed measurements of flow patterns as well as overall performance measurements were made at various flow conditions. The experimental data were compared to those calculated by means of the compressor theory of Professor W. D. Hannie. Excellent agreement was obtained; this was interpreted as a verification of the theory. As a further result, measurements of the maximum efficiency of each blade type have established that a blading with an essentially three-dimensional flow pattern can equal the efficiency of the conventional "free vortex" blading which has a two-dimensional flow pattern.

TABLE OF CONTENTS

I. Introduction

Interest in the air compressor has been intimately connected with the development of the gas turbine power plant. In such a power plant air is compressed by a compressor. Heat is then added, and the air is allowed to expand through the gas turbine proper. The difference between the power produced by the turbine and the power consumed by the compressor is the net output of the machine. This power may be used in the form of "shaft power" taken off the turbine shaft, or it may be used in the form of kinetic energy in a jet issuing from a nozzle behind the turbine. The first form of power is used in the case of stationary engines; the second in the case of jet engines for propulsion. With the temperature limits of present day materials and with air as a working substance the power required by the compressor is of the same order of magnitude as that obtained from the turbine. The net power output being the difference between those two is, therefore, very sensitive to changes in the efficiency of either the turbine or the compressor. At the time gas turbine development was started, turbines with satisfactory efficiencies could be designed owing to available steam turbine experience and to the fact that the flow in a turbine takes place with a decrease in pressure. (This feature promotes flow with small losses.) Compressor experience, however, was

largely lacking, and the development of an efficient air compressor became one of the important problems in gas turbine power plant development.

The first phase of gas turbine power plant development was principally concerned with stationary plants. These units were particularly suitable for a medium range of power (5,000 - 10,000 kw). The main application of these units was for standby power and for power production in locations where condenser water is unavailable. This size and type of power plant was in only limited demand in this country. For this reason possibly, most of the early development took place abroad, particularly in Switzerland. With the advent of interest in jet-propelled planes, however, intensive study of gas turbine power plants was begun in this country and in Great Britain. Again compressor studies were in the foreground. The initial work was done with centrifugal compressors, and the first propulsion units were built along those lines. With the requirement of higher pressure ratios the necessity for staging became apparent. For this purpose the axial compressor has proved to be much more suitable, and investigations on this type were intensified. The axial flow compressor also can be designed with a comparatively small frontal area; this is of importance because of drag considerations in flight. The efficiency of a properly

designed axial flow compressor is somewhat higher than that of a single stage centrifugal compressor. If more than one stage is required by the centrifugal compressor, the axial compressor is considerably more efficient.

The detail properties of the compressor depend, of course, on its particular design. The design of compressor blading for particular performance and flow pattern is quite complicated, and no very adequate general solution of the problem was available at the beginning of the axial flow research program. There was, however, one type of blading, the so-called "Free Vortex Blading" which simplified the flow pattern sufficiently for satisfactory analytical treatment. For this reason this design was very frequently used. Nevertheless, other designs may have some advantages over the "free vortex" design for particular applications. As to test results, a fairly large amount of overall performance data was available, but systematic results on detail surveys were infrequent.

In the course of the gas turbine development in this country, a general theory for the flow through an axial compressor (referred to as "the theory" in the following) was proposed by W. D. Rannie. The theory yields detailed information about the flow, yet it is quite readily usable for engineering work.

The project described in this thesis was started

when research on the axial flow compressors was in about the stage just described. It was felt that for further progress, detailed experimental measurements would be of service. For this reason it was decided to undertake the design and construction of extensive test facilities. The installation was intended to allow overall performance measurements as well as detailed surveys behind blade rows. In addition, it was to be designed with an amount of flexibility sufficient to make it suitable for a large variety of experiments that might interest future investigators. It was also decided to limit the present tests to subsonic speeds, because compressors for power plants were to be principally investigated. For satisfactory operation, these compressors must have a high efficiency, and in the case of aircraft engines, they must allow a large flow per unit frontal area. Since it is believed that these requirements will always be met best by a subsonic compressor, the above restriction to low speed tests was adopted. Adequate correction factors to compensate for compressibility effects within the subsonic range are available.

Two research projects which would make use of these test facilities were then initiated. The first consisted in studying a number of blade types by means of the proposed theory. From this group two blade sets of special

interest were to be selected for manufacture, and detailed experiments were to be performed. From a comparison of the experimental results with the values predicted by the theory, conclusions on the applicability of the theory were to be drawn. In this study the portion of air which is lightly affected by friction was to be emphasized. The second project dealt with the portion of the fluid which is greatly affected by friction, i.e., the blade wakes and boundary layers; these were to be studied analytically and experimentally. The latter problem was to be undertaken by J. T. Bowen (Ref. 1), whereas the former problem was to be investigated by the writer. The design and construction of the test installation was done as a joint project.

This thesis consists of three principal parts:

(a) The design and installation of the compressor test facilities.

(b) A study of the characteristics of various blade designs for given performance conditions.

(c) The experimental investigation of flow patterns of two types of blades and the comparison of these data with the results obtained from the compressor theory.

II. Description of Test Facilities

2:1 The Compressor Installation

2:1.1 General Consideration

As the first step in the design of the test installation, the compressor diameter and blade tip speed had to be selected. In accordance with the purpose of the experiments, conditions in subsonic flow only were to be investigated.

The following considerations were kept in mind: The speed should be high enough to produce pressure differences that could be measured with good accuracy and to give Reynolds' numbers higher than the critical one for the blades. On the other hand, a low speed was desirable, because it reduces considerably the mechanical difficulties inherent in the design. As a further requirement, the dimensions of the compressor should be sufficiently large to permit the placing of instruments of reasonable size into the compressor without seriously disturbing the flow. The hub ratio (%) was to be fairly small to allow the investigation of three-dimensional flow.

On the basis of these considerations a compressor of 36" diameter, having 7" blades and turning at a speed of 1500 rpm was selected.

The complete test installation required for the

operation of the compressor is shown in Figure 1.

In addition to the axial flow compressor proper the principal equipment consists of an electric driving motor (Fig. 1-F9 and Fig. 2) and two air ducts. The air enters at the bell mouth (Fig. 1-F2) passes through the inlet duct (Fig. 3) and the compressor (Fig. 1-F5), and is exhausted through a 90° elbow (Fig. 1-F8 and Fig. 4). The discharge from the elbow is controlled by a throttle (Fig. 5) which can be adjusted to obtain various flow rates through the compressor. The electric motor is operated on direct current so that good speed control can be obtained, and it is cradled in such a manner that its torque output can be measured. The direct current is supplied from a "Motor-generator" set located on a balcony above the test installation (See Fig. 1-A8). The specifications of the electrical equipment are given in table 1.

2:1.2 Design of the Compressor

The selection of the compressor dimensions was discussed in the previous section. The selection of a suitable number of stages was determined by the desire to make possible the attaining of essentially equilibrium flow at the last stage. To accomplish this, three stages were believed necessary. As a further requirement, the unit was to be designed to allow for the exchange and pitch

adjustment of the blades, so that experiments with several blade types might be carried out.

Various views of the compressor are shown in Figures 6 to 9, and a cross-sectional drawing is given in Fig. 10. The compressor consists of the rotor and the stator. The rotor is made up of a 5" diameter shaft to which the three rows of moving blades are fastened like wheels to an axle. The stator is split longitudinally into two halves for assembly, and the halves are held together by bolts. At each side of the machine there is a circular end bell which serves as bearing support for the rotor bearings. The bearings themselves are standard grease lubricated ball bearings. No oil lubrication is required, and the discharge of the compressor is free of oil mist.

The blades of both the rotor and stator are made integral with a threaded stud and are bolted in place. The blades are therefore exchangeable as well as adjustable. Accurate angular adjustment is secured by an indexing arrangement (Fig. 11) which is fastened partly to the blade and partly to the blade carrier (the compressor case or the rotor hub). With this design it is of course also possible to remove some of the rows of blades entirely so that the compressor may also be used as a two or a one stage machine. For many investigations such stage by stage tests, in particular single stage tests will be most

suitable.

The measuring instruments to be used inside the compressor can be introduced through ports in the upper half of the stator. When measurements are to be made, a special instrument carriage can be inserted into the ports (Fig. 12) at the section in question. The remaining ports can be closed off by inserts. These inserts are so designed that stator blades can be fastened to them at the proper locations.

If the compressor is operated with two stages and the blades of both the third rotating and third stationary row are removed, the instrument holder is inserted in the second port and the other ports are closed off by the inserts. Of these, the ones covering the ports of the first and second stage contain the proper stator blades.

2:1.3 Construction of Blades

The determination of the inlet and outlet angle at each radius of a blade row is described in section 3:4.1. Having determined the air inlet and outlet angles, suitable cascade solidities (such that the section lift coefficients are permissible) are selected. With this information, the rule of Constant (see Sec. 3:4.2) is applied to determine the required section camber angle. To insure low cascade losses, the camber line at the leading edge is made tangent

to the inlet velocity direction. A circular arc camber line is then fitted to these cascade angles. The basic geometry being determined, the thickness distribution of a known airfoil is distributed about the camber using a suitable maximum thickness ratio. The thickness distribution used in this case is shown in Fig. 13. The airfoil outline thus obtained is given in the form of coordinates in a Cartesian system in which the airfoil chord forms the abcissa and the origin is located at the leading edge. A typical table of coordinates for one cross-section is shown in table 2. Such a table is prepared for about 5 to 8 blade cross-sections (depending on the blade shape). The orientation of the different cross-sections with respect to each other, is given by the angle that the chord makes with the chord of some reference cross-section, as e.g., the center section. The table of coordinates and the chord angles are the basic data used for the manufacture of the blades.

The cross-sections are then oriented to their proper direction and located radially above each other so that some definite points, e.g., the centers of gravity of the sections, are in a radial line. This method of aligning brings about smooth blade contours. Any systematically selected point is satisfactory as far as the blade contours are concerned, the center of gravity is, however, particularly suitable, as it provides uniform distribution

of the centrifugal force.

For the manufacture of the blades, the selected cross-sections are plotted on steel plates to an enlarged (10 times) scale (Fig. 14). (Steel plates are used instead of drawing paper to avoid shrinkage resulting from changes in moisture.) These drawings are then photographed and printed at full scale (reduced 10 times from the drawing) on template stock. The templates are filed from this stock by hand. The blade itself is then cast (either in sand or in a permanent mold) and finished by hand to fit the templates (Figs. 15 and 16). As a spot check, one blade is sectioned (Fig. 17) at the specified radii and each section is photographed. These photographs are then enlarged 10 times and compared to glass contact prints of the original steel drawings (Fig. 18). In all cases the agreement was extremely good. A machine drawing of a blade is shown in Fig. 19. The blades were manufactured by the Aerolab Development Co., Pasadena, California.

2:2 Instrumentation

The measurements for which the compressor installation is intended consist of two general types, those for the determination of the overall performance of the compressor and those for detailed surveys of velocity and pressure profiles near the blade rows. The instrumentation

provided for this purpose is described in the following sections.

(a). Tachometer (Compressor Speed Measurement)

The rotational speed of the compressor is measured by means of a meter manufactured by the Standard Electric Time Company. The meter consists of a small synchronous generator which is directly coupled to the dynamometer shaft. The generator drives a synchronous motor which operates the indicators of the meter. Two indications of speed may be obtained: first, the instantaneous speed is indicated in rpm on the center dial; second, a revolution counter and timer is provided (see Fig. 20). The counter is switched off and on automatically by the timer so that the number of revolutions in a given period is obtained. The instantaneous indicator is accurate within about 2 rpm. The accuracy of the other method depends on the period over which the count is taken. In the work done so far it was found satisfactory to use one minute intervals. The speed (as observed by the instantaneous dial) remained practically constant during this time, and the accuracy obtained in this way is better than one rpm.

The accuracy of the meter as well as the constancy of the rotational speed was checked by taking simultaneous oscillograph records of the output of the synchronous

generator and of a standard tuning fork. The accuracy figures given above were obtained from these comparisons. It may be mentioned here that instead of using the signal from the tuning fork the radio frequency signal from the Bureau of Standards (WWV, 2.6 MC) may be used conveniently.

(b). Torquemeter (Dynamometer Torque)

When the motor speed is known, the driving power may be calculated, once the torque is determined. Torque is measured by measuring the force on the cradled motor case at a given distance from the center of rotation (Fig. 2). The force in turn is measured by a diaphragm type force meter manufactured by the Hagan Corporation. This device consists essentially of a diaphragm which is loaded by the unknown force on one side and balanced by air pressure on the other side. The balance is effected by a check valve actuated by the diaphragm. The air pressure is then measured by a mercury manometer, and this pressure is an indication of the torque. The unit is calibrated by dead weights, with the dynamometer detached from the compressor. Calibrations are made before and after each run. A typical calibration curve is shown in Fig. 21. The maximum torque measurement anticipated is of the order of 300 ft. lbs. To obtain better accuracy the diaphragm meter was selected for a range of only 50 ft. lbs., and dead weights

were obtained to counter balance any torque above this value. In this manner an accuracy of about 0.4 ft. lb. is obtained. It should be noted here that the force pickup is quite sensitive to shocks caused by imperfections on the rollers of the cradle suspension. To obtain a non-fluctuating indication on the mercury column it was necessary to polish the roller surfaces and to machine them to a concentricity of .0002 inch.

(c). Flow Rate Measurements

The flow rate through the compressor is determined from measurements of the velocity profiles in the entrance duct. A plane normal to the compressor axis and about midway between the compressor entrance vanes and the duct inlet was selected for the profile surveys. At this section velocity surveys were made with a Prandtl type pitot tube having a tip diameter of 3/16". Since the air velocities in the duct are of the order of 50 ft/sec a very sensitive manometer was required to obtain the desired accuracy. The pitot tube was therefore used in connection with a water-micromanometer manufactured by the Meriam Instrument Co. (Fig. 20). This instrument is of the "movable-well" type and can be read to an accuracy of .001 inch of water. In addition to the velocity pressures, the static pressure at the wall of the duct was also recorded.

One survey was made for each valve setting, and from the surveys the discharge rate of air was computed. This discharge rate was then correlated with the wall pressure, and a calibration chart of wall pressure vs. discharge rate was prepared. In all further runs the discharge was determined by a reading of the wall pressure. The calibration curve is shown in Fig. 22. With the necessary density determinations (see Ref. 4) the discharge was obtained to an accuracy of about .25%.

For density determination, the wet and dry bulb temperature was measured in the bell mouth entrance to an accuracy of $1/10^{\circ}F$. The barometric pressure was measured by a standard mercury barometer.

(d). Instrument Carriage

The foregoing measurements constitute the principal ones for the determination of overall quantities. For the detailed surveys, measurements were made directly downstream of each blade row. The probes used for these surveys all had stems of .158" diameter and small measuring heads (see Fig. 23). They were used in a specially constructed traversing carriage which is shown in Fig. 24. It consists of a base and a movable carriage head. The base fits into the compressor ports described in sec. 2:1.2, in such a way that its bottom surface fits flush with the

inside of the compressor case. The probe is located and held in the carriage head by a collar, soldered accurately to the probe. It is then positioned by means of the three wheels on the side of the carriage head. The top wheel moves the probe radially, the center one turns it about its own axis, and the bottom wheel moves the entire carriage head in a circumferential direction. The corresponding dials give the position of the probe. To cover the slit in the carriage base which is necessary to allow the circumferential movement, a flexible sliding tape is made to move with the carriage head. The sliding tape covers the slot completely so that the inner surface of the compressor case is essentially unbroken except for the protruding probe. The ends of the tape recede into the inside of the carriage base. A photograph of the carriage showing the tape and protruding probe is given in Fig. 25. A circumferential angle of 15° can be covered by the traversing probe. This angle is about 30% greater than the $11\frac{1}{4}^{\circ}$ stator blade spacing. Further traversing in the tangential direction is not required as the flow picture should be identical for each segment. This assumption is confirmed by the measurements in the overlapping portion of the area covered by the carriage as well as by additional checks through radial holes at two other circumferential locations (see Fig. 26).

The manufacture of the carriage, as well as the detail design, was performed by Boller and Chivens Engineering Company of South Pasadena, California.

The accuracy with which the probe can be positioned by the carriage is approximately as follows: Radial position, .01 inch; tangential position, 0.05 degree; probe orientation, 0.1 degree.

(e). Yaw Probe (Velocity Direction Measurement)

For the measurement of flow direction a cylindrical yaw tube was used (Fig. 23). The tube is .158 inches in diameter and its pressure orifices measure .015 inches. The orifices are spaced 55° apart. The two side holes are used for determining the flow direction, and the center hole is provided for total head measurements. When the pressure at the two side holes is equal (i.e. the differential pressure between the holes is equal to zero) the center hole is pointing in the direction of flow. This tube, as well as the two to be described, were originally developed at the Pratt and Whitney Corporation, and complete reports on their characteristics are available (Ref. 2). The probes were procured from the Whitney Instrument Co., East Long Meadow, Mass.

To check the direction indicated by the tube, a calibration was made on a test jet (Fig. 27). The carriage

with yaw probe in place was installed near the calibration jet and adjusted to lie in a horizontal plane. The probe was then positioned in the jet and turned about its own axis until the pressure differential between the side holes vanished. This direction was recorded, and the experiment repeated with the carriage rotated about 180° and remaining in the horizontal plane. The mean of the two readings minus the angle of the normal to the plane of the carriage gives the correction which has to be applied to the carriage angle.

(f). Pitot Static Probe (Velocity and Total Head Measurements)

A small Pitot Static Probe (Fig. 23) was procured for the measurement of total head and velocity head. The tube has a diameter of .158" and the measuring tip is .058 inches in diameter, the total head orifice and the static pressure orifices are .026 inches and .009 inches in diameter respectively. The probe indicates total head and velocity head within about 1% if it is pointing within 3° of the flow direction. To insure proper alignment a survey with the pitot static tube is usually preceded by a yaw tube survey. In the operating range of the test compressor, radial velocity components are believed to be sufficiently small so that no appreciable errors in total head and

velocity measurements result. This assumption is verified by good agreement obtained between flow rates measured in the entrance duct and those obtained from detailed internal measurements, (see Table 3).

(g). Kiel Probe (Total Head Measurements)

The Kiel probe (Fig. 23) is a total head tube with a shielding duct. The diameter of the tube is .158 inches and the duct has a length of about .32 inches with a diameter of .125 inches. The pressure orifice is .032 inches. This probe is particularly useful for the total pressure survey of a flow whose direction is not well known, as the probe is quite insensitive to direction. The total head reading is correct within $\frac{1}{2}\%$ if the probe direction is within 30° of the flow direction.

(h). Pressure Pickup Gage

The orifices of the aforementioned probes are all extremely small as set forth in the description. Under some conditions, therefore, they are not suitable for use with a water manometer because such a manometer requires considerable flow through the small orifice for a change in pressure. The time required for equilibrium reading is extremely long. To avoid this difficulty, the small orifice probes are used with an electrical pressure pickup

which consists of a small plunger which actuates strain gages. The gage is manufactured by the Statham Company, Los Angeles, California. This gage requires practically no flow for a change in pressure and the response of the system is quite rapid.

The resistance change of the gage with pressure is detected by means of a special bridge, similar to a Wheatstone bridge. The circuit is shown in Fig. 28. To calibrate the system, the gage is connected in parallel with the micromanometer, and a relation between the strain gage resistance and the applied pressure is obtained. Typical calibration curves are shown in Fig. 29. The curves are for different pressure ranges. Those different ranges may be obtained by adjusting the proper resistances in the special bridge. With the range of 2" of water, the pressure may be read to .002" of water.

III. Comparative Study of Blade Types

3:1 Brief Development of Compressor Theory

3:1.1 Introduction to The Problem

The flow through an axial flow compressor constitutes a very complex problem in fluid dynamics. The difficulties become apparent if one compares this problem to that of determining the flow about an airplane wing. In the case of the compressor one has to deal not with a single wing but with a large number of wings, the blades of the compressor. Each row is formed by a large number of identical blades, and various rows operate axially adjacent to each other. The rotor rows move relative to the stator rows, and the energy of the fluid is changed when it passes through a rotor. In terms of fluid dynamics, the problem therefore consists of calculating the flow of fluid through closely spaced airfoil cascades, the flow being neither irrotational nor of constant energy. The former property applies even though the fluid were assumed perfect, because the rotationality is introduced by the trailing vortices of the blade rows. The change of energy is due to the action of the rotor.

It becomes then the task of the engineer to reduce this problem to one capable of solution, by making justifiable simplifying assumptions. Most present analyses

have in common the assumption that the fluid is perfect and that there are an infinite number of blades in each row. In addition, various other simplifications are introduced by several authors. One of the finest and most detailed analyses of this kind was carried out by F. Marble (Ref. 3). This analysis is suitable for determining the blade shape for certain desired flow characteristics, and it gives detailed information on the complete flow picture for this case. Because of the comprehensiveness of this analysis the actual numerical calculations are, of course, quite laborious for engineering use.

Marble's analysis does, as was pointed out, involve among others the assumption of a perfect fluid, and a discrepancy of a few percent between computed and measured results must be expected. It may then be argued that simplifying assumptions within the perfect fluid theory which are estimated to introduce only errors of the same order, are also permissible, if engineering applications are of primary consideration. A theory of this kind was developed by W. D. Rannie (Ref. 4). The theory gives detailed information about the flow through a compressor, nevertheless it can be quite conveniently used for the solution of the "direct" (calculation of flow from given blades) as well as the "indirect" (calculation of blade shape for desired profile) compressor problem. It is

therefore quite suitable for engineering studies (see sec. 3:3) and engineering design. As mentioned in section I, the purpose of the experiments to be described in section IV of this thesis was to check the adequacy of this theory. In the following section a brief development of the theory will be given. For a detailed presentation, reference is made to the original paper (Ref. 4).

It is interesting to point out that nothing in the theory will restrict the working fluid to air. The results are, therefore, generally valid and apply, e.g., to axial flow water pumps as well as to air compressors.

3:1.2 Development of Basic Equations

As was mentioned, the first assumption made in developing the theory is that of a perfect fluid. As the pressure ratio per stage is usually moderate, a second assumption is permissible, i.e., that the fluid is incompressible. With these two assumptions, the basic equations governing the flow through a blade row, the three Eulerian equations and the continuity equation are written.

The assumption of an infinite number of blades in each row is then introduced; this implies full axial symmetry, i.e., there are no changes in any quantity with the circumferential angle . Let two sections - - - one far upstream of the blade row and one far downstream - - -

be considered. Quantities at these sections will be given the subscripts "a" and "b" respectively. At these sections the radial velocities must have vanished. Under these conditions, the first of the Eulerian equations (the equation for the radial direction reduces to

$$\rho \frac{u_0^2 \lambda_a^2}{\xi_a} = \frac{dp_a}{d\xi_a} \tag{1}$$

at the upstream section, and to

$$\rho \frac{u_0^2 \lambda_b^2}{\xi_b} = \frac{dp_b}{d\xi_b} \tag{2}$$

at the downstream section, where

r_0 = tip radius

u_0 = tip speed of rotor blades

$u_0 \lambda$ = circumferential velocity component*

$u_0 \varphi$ = axial velocity component

$\omega = \frac{\omega_0 r_0}{u_0}$ = Dimensionless angular velocity (this quantity is unity for a rotor and zero for a stator)

$r_0 \xi$ = radial distance

p = static pressure

ρ = fluid density

---

* In cases where confusion cannot arise, the dimensionless coefficient λ is called "tangential velocity component", φ "axial velocity component", etc., the word "dimensionless" being omitted.

Next the Eulerian equation in its vector form is integrated along a streamline again from a point way in front to a point far behind the blade row. This results in the Bernoulli equation, which in the present notation becomes

$$p_a + \tfrac{1}{2}\rho u_o^2(\lambda_a^2 + \varphi_a^2) = p_b + \tfrac{1}{2}\rho u_o^2(\lambda_b^2 + \varphi_b^2) \qquad (3)$$

in the case of a stator row.

For a rotating row, the integration is carried out along a streamline relative to the rotor and the result becomes

$$p_a + \tfrac{1}{2}\rho u_o^2(\lambda_a^2 + \varphi_a^2 - 2\omega\xi_a\lambda_a) = p_b + \tfrac{1}{2}\rho u_o^2(\lambda_b^2 + \varphi_b^2 - 2\omega\xi_b\lambda_b) \qquad (4)$$

The continuity equation will be used in its differential form, which gives

$$\varphi_a \xi_a \, d\xi_a = \varphi_b \xi_b \, d\xi_b \qquad (5)$$

It is now assumed that any changes in the flow profiles due to the action of the blades take place while the fluid is moving through the blades. Any changes in velocities which occur outside the blade row are considered to be negligible. According to this assumption, the velocities which appear in the foregoing Bernoulli relations are practically equal to the velocities at the leading and

trailing edge of the cascade respectively, so that these velocities can be used in determining cascade blade angles.

This assumption is plausible because of the following reasoning: The total radial shift of the streamlines from a point far in front to a point far behind the blade row can be calculated and is in general small, compared to the radius. This in turn means that the radial velocities will be small compared to the axial velocities. This should be particularly true outside the blade row, as a large part of the shift should be expected to take place within the blade row, the place where the forces are acting. The same type of reasoning applies to the axial velocity component, as the change in axial velocity is related to the streamline shift by the continuity of mass flow. Lastly, the change in tangential velocity after leaving (or before entering) the blade row must also be small, because there are no tangential forces acting on the air outside of the blade rows. There is therefore no change in moment of momentum and the tangential velocity of a fluid particle must be proportional to its radial position. This radial position changes, however, only slightly because of the small radial shift, which was just mentioned.

It is mainly this assumption of negligible radial velocities and its consequences which simplify the compressor theory so much. It makes the compressor theory

sufficiently flexible to allow a comparatively simple treatment of the direct as well as of the indirect problem. Equations 1 to 5 then are the basic ones to be used in this development, as will be shown in the following sections.

The preceding argument is, of course, supposed to show merely that the assumption is plausible. Checks on its validity are discussed with the aid of the experimental data in section IV, in accordance with the purpose of these experiments. The assumption is, however, also supported by the calculations of the flow pattern for a typical case as carried out in section 3:5, using Marble's results (Ref. 3).

3:1.3 The Direct Problem

The "direct problem" in compressor design - - - in analogy with the wing theory - - - consists of determining the flow through a given blade row. The approaching flow will be considered known, and the flow leaving the row is to be determined. In accordance with the previous development the blade row is taken to consist of an infinite number of blades. This in turn means that the exit angle of the flow is known and independent of the entrance condition.

Let a rotor row now be considered. Differentiating

the Bernoulli equation (eq. 4) and substituting the first Eulerian equations (eqs. 1 and 2) for the pressure differentials, one obtains

$$\frac{d\xi_a}{d\xi_b}\left[\frac{\lambda_a^2}{\xi_a} + \frac{1}{2}\frac{d}{d\xi_a}\left(\lambda_a^2 + \varphi_a^2 - 2\omega\xi_a\lambda_a\right)\right] = \frac{\lambda_b^2}{\xi_b} + \frac{1}{2}\frac{d}{d\xi_b}\left(\lambda_b^2 + \varphi_b^2 - 2\omega\xi_b\lambda_b\right) \qquad (6)$$

On the left-hand side, the combination of terms

$$\frac{\lambda_a^2}{\xi_a} + \frac{1}{2}\frac{d}{d\xi_a}\left(\lambda_a^2 + \varphi_a^2\right)$$

is proportional to the energy gradient of the approaching flow, and this function will be designated by the symbol F. From the geometry of the velocity diagram, the tangential velocity component λ_b is seen to be equal to

$$\lambda_b = \omega\xi_b - \varphi_b \cot\beta_\varepsilon \qquad (7)$$

where β_ε is the known exit angle from the blade row. Substituting these expressions into eq. 6, the following relation is obtained

$$\frac{\left(\omega\xi_b - \varphi_b\cot\beta_\varepsilon\right)^2}{\xi_b} + \frac{1}{2}\frac{d}{d\xi_b}\left[-\omega^2\xi_b^2 + \varphi_b^2\cot^2\beta_\varepsilon + \varphi_b^2\right] = \left[F - \omega\frac{d}{d\xi_a}\left(\xi_a\lambda_a\right)\right]\frac{d\xi_a}{d\xi_b}$$

From the continuity relation the ratio $d\xi_a/d\xi_b$ is shown to be equal to

$$\frac{d\xi_a}{d\xi_b} = \frac{\varphi_b\xi_b}{\varphi_a\xi_a}$$

Substituting this equation and simplifying, one obtains the following differential equation for φ_b .

$$\frac{d\varphi_b}{d\xi_b} + \left[\frac{\cos^2\beta_\varepsilon}{\xi_b} - \frac{d}{d\xi_b}\left(\ln \sin\beta_\varepsilon\right)\right]\varphi_b = \omega\left[2\sin\beta_\varepsilon\cos\beta_\varepsilon - \frac{\xi_b}{\varphi_a \xi_a}\sin^2\beta_\varepsilon \frac{d}{d\xi_a}\left(\xi_a \lambda_a\right)\right] + \frac{\xi_b}{\xi_a \varphi_a} F \sin^2\beta_\varepsilon .$$

The ratio of the two streamline radii before and after the blade row, ξ_a/ξ_b , is equal to unity at the inside and at the outside radius of the channel and differs from this value only very slightly at other radii, for almost all practical cases. This ratio will therefore be taken equal to unity as a first approximation. The foregoing differential equation can then be solved, the answer being

$$\varphi_b = \sin\beta_\varepsilon \, e^{-\int_{\xi_i}^{\xi_b} \frac{\cos^2\beta_\varepsilon}{\xi_b} d\xi_b} \left\{ \int_{\xi_i}^{\xi_b} \left[\omega\left(2\cos\beta_\varepsilon - \frac{\sin\beta_\varepsilon}{\varphi_a}\frac{d}{d\xi_a}\left(\xi_a\lambda_a\right) + \frac{F}{\varphi_a}\sin\beta_\varepsilon\right] e^{\int_{\xi_i}^{\xi_b} \frac{\cos^2\beta_\varepsilon}{\xi_b} d\xi_b} d\xi_b + K \right\} \quad (8)$$

The constant K is evaluated by means of the integrated continuity equation, so that

$$\int_{\xi_i}^{1} \varphi_a \xi_a \, d\xi_a = \int_{\xi_i}^{1} \varphi_b \xi_b \, d\xi_b \quad (9)$$

If it is desired to find the streamline radius ξ_b of a stream surface behind the blade row, which had a radius of

ξ_a in front of the blade row, this may be done as follows: According to the definition of the stream surface, the flow between two stream surfaces is constant at any cross-section. Taking the inner cylinder of radius ξ_i as one stream surface and the stream surface in question as the other, one can write

$$\int_{\xi_i}^{\xi_a} \psi_a \xi \, d\xi = \int_{\xi_i}^{\xi_b} \psi_b \xi \, d\xi \qquad (10)$$

This is an equation for the limit of the right-hand integral. It is usually most convenient to evaluate eq. (10) by plotting both integrals vs. ξ. Vertical lines (constant flow rate) on this graph will intersect the two curves at corresponding radii ξ_a and ξ_b. A relation between ξ_a and ξ_b can be obtained in this way (see Fig. 46). This function may then be substituted in equation (8) for a second approximation. In the cases considered in this report (see sec. 3:5) this was not necessary, for the accuracy desired as the ratio of the radii did not differ sufficiently from unity at any radius.

Equation (8) together with the geometrical relationship of equation (7) gives then the complete solution for the flow through a rotating blade. The same equation is, of course, applicable to a stator row. It is just necessary to set the dimensionless angular velocity, ω, equal

to zero. It is this equation which has been used to calculate the velocity profiles in section 4:2. Some simplifications of the equation are possible in special cases. If, e.g., the approaching flow is of constant energy; the factor F is equal to zero. Also, in some cases the differential $\frac{d}{d\zeta_a}(\zeta_a \lambda_a)$ may be evaluated analytically.

3:1.4 The Indirect Problem and The Selection of Blade Types

The "indirect problem" is concerned with the design of compressor blading for certain given conditions. For a large number of applications multistage compressors are required, and in this case a repeating flow pattern will in general be chosen. The following discussion will apply to this type of compressor.

Consider a single stage, i.e., a rotor followed by a stator, of a multistage compressor. Three locations will be of interest, a cross-section in front of the rotor, one behind the rotor and one behind the stator. Quantities at these cross-sections will be denoted by subscripts 1, 2, and 3 respectively.

With these provisions the Bernoulli equation for the flow through the rotor becomes

$$p_1 + \tfrac{1}{2}\rho u_0^2 (\lambda_1^2 + \varphi_1^2 - 2\zeta_1\lambda_1) = p_2 + \tfrac{1}{2}\rho u_0^2 (\lambda_2^2 + \varphi_2^2 - 2\zeta_2\lambda_2) \qquad (11)$$

and that for the stator becomes

$$p_2 + \tfrac{1}{2}\rho u_0^2\left(\lambda_2^2 + \varphi_2^2\right) = p_3 + \tfrac{1}{2}\rho u_0^2\left(\lambda_3^2 + \varphi_3^2\right) \qquad (12a)$$

The requirement of a repeating flow pattern, however, means that the velocity is the same in magnitude and direction after each full stage. Therefore λ_3 must be equal to λ_1 ; φ_3 equal to φ_1 , and $\xi_3 = \xi_1$. Equation (12a) therefore becomes

$$p_2 + \tfrac{1}{2}\rho u_0^2\left(\lambda_2^2 + \varphi_2^2\right) = p_3 + \tfrac{1}{2}\rho u_0^2\left(\lambda_1^2 + \varphi_1^2\right) \qquad (12)$$

The second Eulerian equation applied to the three cross-sections, yields the following

$$\frac{dp_1}{d\xi_1} = \frac{dp_3}{d\xi_1} = \rho u_0^2 \frac{\lambda_1}{\xi_1} \qquad (13)$$

and

$$\frac{dp_2}{d\xi_2} = \rho u_0^2 \frac{\lambda_2}{\xi_2} \qquad (14)$$

Finally, the continuity equation in its integrated form gives

$$\boxed{\int_{\xi_c}^{\xi_0} \varphi_1 \xi_1 \, d\xi_1 = \int_{\xi_c}^{\xi_0} \varphi_2 \xi_2 \, d\xi_2 = \tfrac{1}{2}\bar{\varphi}\left(\xi_0^2 - \xi_c^2\right)} \qquad (15)$$

where $\bar{\varphi}$ is the average axial velocity component.

These equations are the basic ones developed in section 3:1.2 applied to the present problem. For use in the following they will be rearranged somewhat. From equations (11) and (12) one obtains

$$\frac{p_3 - p_1}{\frac{1}{2}\rho u_0^2} - \psi = 2(\xi_2 \lambda_2 - \xi_1 \lambda_1)$$

Within the accuracy of the linearization (Sec. 3:1.3) this becomes

$$\boxed{\psi = 2\xi(\lambda_2 - \lambda_1)} \tag{16}$$

Differentiating equation (12) and substituting equation (13) it follows that

$$\frac{\lambda_2^2}{\xi_2} + \frac{1}{2}\frac{d}{d\xi_2}(\lambda_2^2 + \varphi_2^2) = \left[\frac{\lambda_1^2}{\xi_1} + \frac{1}{2}\frac{d}{d\xi_1}(\lambda_1^2 + \varphi_1^2)\right]\frac{d\xi_1}{d\xi_2} \tag{17}$$

This may be arranged into the form

$$\boxed{\frac{d}{d\xi_2}(\varphi_2^2) + \frac{1}{\xi_2^2}\frac{d(\xi_2^2\lambda_2^2)}{d\xi_2} = \left[\frac{d}{d\xi_1}(\varphi_1^2) + \frac{1}{\xi_1^2}\frac{d(\xi_1^2\lambda_1^2)}{d\xi_1}\right]\frac{d\xi_1}{d\xi_2}}$$

The boxed equations will be used in this discussion. $\bar{\varphi}$ in equation (15) is the given design flow and in equation (16) ψ is the work coefficient. From the postulate of the repeating flow pattern and equations (13) it follows that ψ is constant at the design condition. The local value of ψ

therefore is equal to the average design value $\overline{\psi_d}$. Furthermore, the integrated continuity equation serves only as a boundary condition and is used to evaluate the constants of integration. Consequently, the problem consists of two equations (eq. 16 and 17) and four unknowns ($\varphi, \varphi_2, \lambda_1, \lambda_2$). Two additional conditions may therefore be imposed.

For most applications of axial flow compressors the entering air is of nearly constant energy. This means that there is no change of total head with radius, or symbolically

$$\frac{d p_2}{d \xi} = 0 \tag{18}$$

Since ψ was shown to be constant, this condition will hold throughout the compressor. The two sides of equation (17), now, just represent the change of total head with radius, so that, by virtue of equation (18), we may set each side equal to zero. Dropping the subscript for ξ, one obtains

$$\frac{d}{d\xi}(\varphi_2)^2 + \frac{1}{\xi^2}\frac{d}{d\xi}(\xi^2 \lambda_2^2) = 0 \tag{19}$$

$$\frac{d}{d\xi}(\varphi_1)^2 + \frac{1}{\xi^2}\frac{d}{d\xi}(\xi^2 \lambda_1^2) = 0 \tag{20}$$

The system to be solved consists now of three equations

and four unknowns. This means that with the design performance ($\bar{\varphi}_2$ and $\bar{\psi}_2$) and entrance condition ($\frac{d\varphi}{d\zeta} = 0$) specified, still one quantity may be selected at will, in other words: An infinite number of blade types can be designed to give a specified performance at specified entrance conditions. Each blade type will have special properties, and the most suitable one can be selected for each particular application. As an example of the properties that may be controlled in this manner the velocity of the air relative to the blades is mentioned. For high speed compressors this velocity should be low in order to avoid adverse compressibility effects. The maximum relative velocity can be kept low by using the proper blading.

For this study the tangential velocity in front of the rotor (λ_1) was selected as the additional condition that can be imposed on the problem. For the series studied, λ_1, was taken to be of the form $\lambda_1 = \alpha \zeta^n$, where α is a constant and n was taken equal to -2, -1, 0, 1, and 2 for the various cases. This series was selected because the corresponding blades cover quite a variety of shapes and because the most frequently used blading ($\lambda_1 = \alpha/\zeta$) is a member of this series. Names have been attached to two of the blade types corresponding to the above selection of the circumferential velocity, λ_1. If n = -1, the resulting blade type is called a "free vortex" blading, because the

distribution of the circumferential velocity component is the same as that in a "free vortex". Similarly, the blading corresponding to n = 1 is called a "solid body" blading. There is no other significance to these names.

As an example the solution of the equations will be carried out for one case, the case n = -2. Substituting $\lambda_1 = \alpha/\xi^2$ into equation (20) one obtains

$$\frac{d}{d\xi}(\varphi_1^2) = -\frac{1}{\xi^2}\frac{d}{d\xi}(\alpha^2\xi^{-2}) = 2\alpha^2\xi^{-5}$$

and upon integrating

$$\varphi_1^2 = \kappa_1 - \frac{\alpha^2}{2\xi^4}$$

or

$$\varphi_1 = \sqrt{\kappa_1 - \frac{\alpha^2}{2\xi^4}} \ .$$

From equation (16) λ_2 is found to be equal to

$$\lambda_2 = \lambda_1 + \frac{\psi}{2\xi} = \frac{\alpha}{\xi^2} + \frac{\psi}{2\xi}$$

Substituting this expression into equation (19) one obtains

$$\frac{d}{d\xi}(\varphi_2^2) = \frac{-1}{\xi^2}\frac{d}{d\xi}\left(\frac{\psi^2}{4} + \frac{\alpha\psi}{\xi} + \frac{\alpha^2}{\xi^2}\right) = \frac{\psi\alpha}{\xi^4} + \frac{2\alpha^2}{\xi^5} \ .$$

Upon integrating this becomes

$$\varphi_2^2 = \kappa_2 - \frac{1}{3}\frac{\alpha\psi}{\xi^3} - \frac{1}{2}\frac{\alpha^2}{\xi^4}$$

or

$$\varphi_2 = \sqrt{\kappa_2 - \frac{1}{3}\frac{\alpha\psi}{\zeta^3} - \frac{1}{2}\frac{\alpha^2}{\zeta^4}}$$

The constants κ_1 and κ_2 are evaluated by means of equation (15), as follows

$$\int_{\zeta_i}^{\zeta_o} \sqrt{\kappa_1 - \frac{\alpha}{2\zeta^4}}\, \zeta\, d\zeta = \frac{1}{2}\bar{\varphi}\left(\zeta_o^2 - \zeta_i^2\right)$$

and

$$\int_{\zeta_i}^{\zeta_o} \sqrt{\kappa_2 - \frac{1}{3}\frac{\alpha\psi}{\zeta^3} - \frac{1}{2}\frac{\alpha^2}{\zeta^4}}\, \zeta\, d\zeta = \frac{1}{2}\bar{\varphi}\left(\zeta_o^2 - \zeta_i^2\right)$$

These integrals have to be evaluated graphically; only for some special values of n can an analytical solution be found.

The same procedure is followed for other values of n. It should be noted how particularly simple the solution becomes if $\lambda_1 = \alpha/\zeta$. In this case $\varphi_1 = \varphi_2 = \bar{\varphi}$ i.e. the axial velocity is constant throughout the compressor. It follows that there is no streamline shift and no radial velocity. Consequently the compressor problem is actually reduced to a two-dimensional one. It is largely because of this analytical simplification that this design (the so-called "free vortex" design) has been used so frequently.

There is, however, one property unique to the "free vortex" blading: the axial velocities φ_1 and φ_2 are not a function of the hub ratio. In multistage machines, therefore, in which the density change of the air is considerable the same blade shapes may be used by simply increasing the hub ratio and decreasing the blade length. At each radius then the blade sections for the rotors and stators respectively will be identical throughout the compressor. This may mean a considerable simplification in manufacturing.

3:2 Criteria of Comparison

The numerical calculations for the above set ($\lambda_1 = \alpha f^n$) were carried out, taking the work coefficient $\bar{\psi}_d$ equal to .40, and the discharge coefficient $\bar{\varphi}_d$ equal to .45. A hub ratio of .60 was used throughout and, in order to obtain a more uniform basis of comparison, the tangential velocity at midradius was kept constant for all designs. (The effect of this assumption is discussed later.) For these conditions certain characteristics of the blades were computed which were believed to be of importance for selection purposes. The characteristics that were computed are the following:

(a) Maximum Relative Velocity.

The relative velocity was computed for various sections of the rotor and stator and the maximum for each blade type was noted. The maximum relative velocity is of importance for air compressors because it determines the place at which adverse compressibility effects will first occur. A low relative velocity is therefore desirable for high speed compressors. In determining the velocities for this study, values were taken from the velocity diagrams and no attempt was made to determine local velocities at the blade surfaces. The values will, however, be characteristic and the relative merits of the different blade types in this respect will be correctly indicated.

(b) Maximum Turning Angle.

The angle through which the air is turned was computed for various sections of the stator and rotor. The largest angle was recorded for each blade type. The angle of turning is related to the lift coefficient. Large angles are liable to cause cascade losses and early "stall".

(c) Maximum Chord Twist.

The angle between the chords of the tip and root was computed for the rotor and stator. The larger one

(it usually occurs on the rotor) was compared to the values of the other blade types. The characteristic of blade twist is of interest mainly for structural and manufacturing reasons. A large twist is undesirable in this respect.

(d) Reaction Ratio.

The reaction ratio was defined as the pressure increase through the rotor divided by the pressure increase through a complete stage. In the previous notation this ratio is given by

$$\rho = \frac{p_2 - p_1}{p_3 - p_1} \tag{21}$$

For the case of a multistage compressor with repeating flow pattern, this is equal to

$$\rho = \frac{(\lambda_1^2 - \lambda_2^2) + (\varphi_1^2 - \varphi_2^2) + 2\xi(\lambda_2 - \lambda_1)}{2\xi(\lambda_2 - \lambda_1)} \tag{21a}$$

by virtue of eq. (11) and (12). This ratio was computed for various sections of each blade type. The minima and maxima were used for comparison.

It is desirable to keep the pressure increase through rotor and stator fairly well balanced so as to avoid too rapid diffusion in either rotor or stator.

Rapid diffusion is undesirable because it causes losses through excessive boundary layer growth, which eventually leads to separation.

(e) Cavitation Coefficient.

The phenomenon of cavitation occurs, of course, only if the working fluid of the compressor (or rather pump) is a liquid. In this case cavitation limitations correspond largely to the compressibility limitations which occur when the working fluid is air, although the physical processes are entirely different. Both effects will first become apparent at the point of the blade surface where the pressure is lowest and the velocity highest. For this reason the cavitation tendency would be well indicated by the previously discussed criterion of "maximum relative velocity". It is, however, desired to establish an order of magnitude of the pressures involved and also to indicate how calculations of this pressure could be carried out, provided the necessary experimental data were available. A coefficient indicating the tendency to cavitation was therefore defined as

$$\sigma' = \frac{p_o - p}{\frac{1}{2}\rho u^2} \qquad (22)$$

where p_o is the pressure of the purely axial flow at entrance, and p is the minimum pressure occurring near the

leading edge of the rotor blades. This minumum pressure can be computed only when the blade sections are known precisely. A nominal value that should be fairly satisfactory for purposes of comparison was calculated in the following way.

A mean relative velocity ω_m was defined for the rotor as

$$\left(\frac{\omega_m}{u_0}\right)^2 = \left(\frac{\varphi_1+\varphi_2}{2}\right)^2 + \left(\frac{2\xi-\lambda_1-\lambda_2}{2}\right)^2$$

and the corresponding mean pressure is equal to

$$p_m = p_1 + \tfrac{1}{2}\rho\left(\omega_1^2 - \omega_m^2\right)$$

where ω_1, is the relative velocity in front of the rotor, which in the previous notation is defined by

$$\left(\frac{\omega_1}{u_0}\right)^2 = \left(\xi-\lambda_1\right)^2 + \varphi_1^2$$

The pressure coefficient for the minimum pressure point was defined as

$$C_p = \frac{p-p_m}{\tfrac{1}{2}\rho\omega_m^2}$$

and it was now assumed that this coefficient is proportional to the lift coefficient, i.e.

$$C_p = -a\,C_L$$

The lift coefficient in turn is given by the equation

$$\rho \omega_m \Gamma = \tfrac{1}{2} \rho \omega_m^2 c C_L$$

where the circulation Γ is equal to

$$\Gamma = u_0 s (\lambda_2 - \lambda_1)$$

With these equations, the cavitation coefficient becomes

$$\sigma' = 2a\left(\frac{s}{c}\right)(\lambda_2 - \lambda_1)\left(\frac{2\xi - \lambda_2 - \lambda_1}{2}\right)^2 + \left(\frac{\varphi_1 + \varphi_2}{2}\right)^2$$
$$-(\xi - \lambda_1)^2 + \left(\frac{2\xi - \lambda_2 - \lambda_1}{2}\right)^2 + (\lambda_1^2 + \varphi_1^2) - \left(\frac{\varphi_1 + \varphi_2}{2}\right)^2 . \qquad (23)$$

This derivation is somewhat indirect. It was, however, desired to include the coefficients C_p and C_L based on ω_m, because available test information is usually given in this form. From the data a value of 4 for "a" was found representative (Ref. 5), and (s/c) was taken from the "free vortex" blading of the present compressor.

With these assumptions the coefficient σ' was calculated for various radii of each blade type and the maximum value was used for comparison. A large value of σ' indicates a tendency of the blades to cavitate. It is again emphasized that the coefficient here calculated is

approximate and should be regarded only as giving the relative cavitation tendency of the blade types as well as the correct order of magnitude.

3:3 Comparison of Blade Types

The criteria of the previous section were computed for the selected blade sets and the numerical results are presented in table 4. The velocity diagrams are shown in Fig. 30a. As expected, although designed for the same overall performance conditions, the blades do exhibit a difference in their characteristics. For a more convenient comparison, the blade types have been listed in table 5 in order of their suitability for each of the criteria. Using the table as a whole for a basis, the types $\lambda_1 = \alpha\xi^2$, and $\lambda_1 = \alpha\xi$ show up most favorably. They are then followed by the types $\lambda_1 = \alpha$, $\lambda_1 = \alpha/\xi$ and $\lambda_1 = \alpha/\xi^2$. Let the comparison now be made for a single criterion, e.g. the important one of lowest relative velocity. There again $\lambda_1 = \alpha\xi^2$ and $\lambda_1 = \alpha\xi$ are most favorable with $\lambda_1 = \alpha$, $\lambda_1 = \alpha/\xi$ and $\lambda_1 = \alpha/\xi^2$ following in this order. The reduction in relative velocity from the "free vortex" blading to the "solid body" blading is about 10%. This reduction, although not large, is significant for high speed compressors. Also one would expect the differences to be more pronounced for smaller hub ratios. Similar comparisons can be

made for the other criteria. In general, then, some of the other blade types show definite advantages over the "free vortex" type and they should be considered carefully in compressor design.

The study is, of course, not complete. One of the limitations imposed was that λ, at the midradius was taken equal for all types. (The value chosen for λ, corresponds closely to a 50% reaction at the blade center.) To observe the effect of the removal of this restriction, the "free vortex" and "solid body" types were calculated for a large range of values of λ, at the midradius (see tables 6 and 7, and Figs. 30b and 30c). This changes of course the reaction ratio at the center and also the twist of the blades. It does, however, have only a very slight effect on the other criteria. This can be seen by inspecting again table 5, in which the optima of each property for the whole set of "solid body" and "free vortex" blading were entered with brackets.

A second limitation was the assumption that ψ be constant. This assumption does apply for a typical stage of a multistage compressor. For some special single stage designs as for instance for the first stage of a multi-stage compressor and for some wind tunnel fans, a different distribution of ψ may be advantageous. In this study, however, the assumption seems appropriate.

The third limitation lies in the type of function used for λ, . By using different functions more blade shapes can be obtained, and some of these will no doubt exhibit improvements in special characteristics. The possible improvement is, however, believed to be limited. As an example, a flow pattern was constructed to give a minimum value for the maximum relative velocity. In this construction only the conditions for energy addition and continuity were satisfied and the Eulerian equations were disregarded. Nevertheless, the resulting optimum flow pattern had a maximum relative velocity (in terms of tip speed) of as much as (.70). The best maximum velocity of the blade types which were analyzed was as low as (.81). This then may be taken as an indication that not much improvement over the blade types investigated can be obtained. It may be said then that the study does cover quite a range of different blade shapes and should be representative as a general survey.

3:4 Particular Designs

3:4.1 Design Flow Patterns

The blade study of the previous section will now be used as a basis for selecting two blade sets for the experimental work. For this purpose two sets are of

particular interest: the "free vortex" blading ($\lambda_1 = \alpha/\xi$), and the "solid body rotation" blading ($\lambda_1 = \alpha\xi$). The "free vortex" blading was selected because it was desired to measure in detail the flow pattern of this more conventional set at its design point and to determine its efficiency in order to establish a basis of comparison with other blade types. Off the design point, this blading does not possess any properties simplifying the flow pattern, and the experiments at these flow rates lend themselves very well for checks on the theory. The "solid body" set is of general interest because of its advantageous properties, which were discussed in the previous section. It is of special interest here because it represents a blade shape very different from the "free vortex" blades and leads to three-dimensional flow at the design point as well as off the design point. This will give further check on the proposed compressor theory, and it will show whether or not such a blading has a comparable efficiency at its design point.

For these reasons it was decided to construct a set of each of these two blade types. (See Fig. 31)

The calculations of the design flow pattern were carried out as shown in section 3:1.4. They will be briefly outlined in the following.

(a) "Free vortex" blading.

The "free vortex" blading implies the assumption

$$\lambda_1 = \alpha/\xi$$

λ_2 is then determined from equation (16), which gives

$$\lambda_2 = \frac{\pi}{2\xi} + \frac{\alpha}{\xi}$$

Substituting these expressions for λ_1 and λ_2 into equations (19) and (20) respectively and integrating one obtains

$$\varphi_1 = K_1$$

and

$$\varphi_2 = K_2$$

By use of the continuity equation both constants are seen to be equal to the average axial velocity component $\bar{\varphi}_a$ so that

$$\varphi_1 = \varphi_2 = \bar{\varphi}_a$$

The particular simplifications which occur for the "free vortex" design were pointed out previously. The constant

was selected here so that the 50% reaction point is located at $\xi = 0.7$. This radius was selected for the 50% reaction point in preference to the midradius ($\xi = 0.8$) in order to avoid excessive turning angles near the root.

(b) "Solid Body" blading.

Proceeding analogously as in the case of the "free vortex" blading, the tangential velocity in front of the rotor is now taken to be equal to

$$\lambda_1 = \alpha \xi$$

From equation (16), λ_2 is determined as

$$\lambda_2 = \frac{\nu}{2\xi} + \alpha \xi$$

Substituting the expressions for λ_1 and λ_2 into equations (19) and (20) and integrating one obtains

$$\varphi_1 = \sqrt{\kappa_1 - 2\alpha^2 \xi^2}$$

and

$$\varphi_2 = \sqrt{\kappa_2 - 2\alpha^2 \xi^2 - 2\nu\alpha \ln \xi}$$

The constants κ_1 and κ_2 are evaluated by means of the continuity equation. For the blade set which was manufactured, was selected so as to give a 50% reaction at the mid-radius ($\xi = 0.8$). The values of λ_1, λ_2, φ_1, and φ_2 determine the velocity diagrams at all radii. A tabulation of the velocity components and the corresponding angles is given in tables 8 and 9, and 10 and 11, for the "free vortex" and "solid body" blading respectively. A diagrammatic representation of the blading for the two types

is shown in Fig. 31.

3:4.2 The Cascade Leaving Angle

In the previous calculations a cascade with infinitely close blade spacing has been assumed. In that case the direction of the air leaving the cascade is equal to the tangent of the trailing edge of the blades. In any actual case, the blade spacing is finite and the leaving angle has to be determined.

Two principal methods can be used for this determination. First an empirical rule relating the blade camber and spacing to the air deflection is available. According to this relation

$$\theta^* = \theta_c \left(1 - 0.26\sqrt{s/c}\right) \qquad (24)$$

where θ^* is the air deflection, θ_c is the blade camber angle, and (s/c) is the ratio of spacing to chord. This relation was formed on the basis of experimental cascade data. The rule was formulated by H. Constant (Ref. 6). For the present work the rule was interpreted to mean that the exit angle computed by eq. 24 is independent of the entrance conditions, i.e., a cascade with an infinite number of blades having the calculated exit angles is substituted for the real cascade.

In the second method the exit angle is taken to be equal to that calculated for a two-dimensional cascade of thin blades having the same camber line and spacing as the cross-section of the real blades in question. The angle is calculated by a conformal transformation from the flow about a cylinder. Details of the transformation may be found in Ref. 4.

As a third method, recourse may be taken to two-dimensional experimental cascade data. This possibility is discussed in section 4:9. It is at present often limited by the lack of sufficient cascade data.

The first two methods were both used in the computation of flow patterns (see sec. 4:2). For the design of the blades Constant's rule was used exclusively, however, the transformation method leads to very much the same results for the cases in question.

3:5 Comparison of The Present Compressor Theory With a More Exact Perfect Fluid Theory.

3:5.1 Introduction

In section 3:1, a method of determining the velocity profiles far in front of and far behind a blade row was discussed. It was pointed out that the difference between these profiles and the profiles existing at the leading and trailing edges of the blades respectively, is expected

to be very small. For this reason the profiles at the far sections were selected for determining the blade angles.

Using the results of some of Marble's work (Ref. 3) it is possible to approximate closely the flow near a blade row of small axial extension. The difference between those values and the flow data of the far sections can then be realized, and the merits of the assumptions of the present theory can be checked.

The comparison has been carried out for a special case, the "solid body" blading (see sec. 3:4.1) operating at the design point.

3:5.2 Computations.

Marble shows in his paper (Ref. 3) that for the aforementioned use the axial velocity component at any section may be approximated by means of the equations

$$\frac{c_a}{u_0} = \varphi = \varphi_1 + \frac{1}{2}(\varphi_2 - \varphi_1)\, e^{\nu \frac{\zeta}{\zeta_0 - \zeta_c}} \qquad \text{for } \zeta \leq 0$$

$$\frac{c_a}{u_0} = \varphi = \varphi_1 + (\varphi_2 - \varphi_1)\left[1 - \frac{1}{2} e^{-\nu \frac{\zeta}{\zeta_0 - \zeta_c}}\right] \qquad \text{for } \zeta > 0 \qquad (25)$$

where ζ is the axial distance from the blade center divided by the tip radius. The constant ν may be computed in various ways. For this computation it was taken equal to 3.20 (slightly larger than π). This corresponds to taking the first term of a series which gives the more exact distri-

bution. The complete series is given in reference 4 and the fact that the approximation leads to a high degree of accuracy is also discussed there. Knowing the axial velocity component, the radial one may be computed from the continuity equation, so that

$$\frac{c_r}{u_0} = \mu = \frac{\nu}{\zeta_0 - \zeta_i} \; e^{-\frac{\nu}{\zeta_0 - \zeta_i}|\zeta|} \; \frac{1}{2\zeta} \int_{\zeta_i}^{\zeta} (\varphi_1 - \varphi_2)\, \zeta \, d\zeta \tag{26}$$

where μ is the dimensionless radial velocity. Also, knowing φ, points of the streamline at any section may be determined by using the definition of the streamline which says that the flow between two streamlines is constant. Using the hub as one of the streamlines, one finds

$$\int_{\zeta_i}^{\zeta_1} \varphi_1 \, \zeta \, d\zeta = \int_{\zeta_i}^{\zeta_2} \varphi \, \zeta \, d\zeta \tag{27}$$

This is an equation for the limit ζ_2, the radius at a given ζ of a streamline which had a radius of ζ_1, far in front of the blade grid. Using equation (27) for various axial positions and various stream tubes, the complete stream tube picture may be obtained. (A typical auxiliary graph which was used for such a computation is shown in Fig. 46.) With the aid of the stream tube picture the change in tangential velocity may be determined. All the change in moment of momentum takes place at the blade row (assumed to be a disk of zero axial extension). The

moment of momentum of each particle of fluid remains constant from a position far upstream to the blade row and then again from the blade row to a section far downstream, because there are no tangential forces acting between these stations. The tangential velocity at any section upstream of the blade row is therefore equal to

$$\lambda = \lambda_1 \frac{\xi_1}{\xi_\zeta} \tag{28}$$

where λ_1 is the tangential velocity at radius ξ_1 far upstream and ξ_ζ is the radius of the same stream tube at ζ. Similarly the tangential velocity at any section upstream is found to be equal to

$$\lambda = \lambda_2 \frac{\xi_2}{\xi_\zeta} \tag{28a}$$

3:5.3 Comparison of Results

The calculations were carried out for the flow through the entrance vanes, and the rotor. The calculations for the stator are identical with those for the flow through the rotor, except for the signs. The results are presented in the form of graphs of the axial velocity, φ, the radial velocity μ and the tangential velocity λ, vs. the axial distance ζ for various radii ξ. (See Figs. 32 to 37.) In each one of these graphs the location of the edge of the actual blades is also indicated, and it is

seen that there exists only a very small difference between the conditions at the far sections and those at the blade edges. For the design of blades, the difference in the flow angle between these sections is of most interest. The flow angle, (the angle formed by φ and λ), was plotted as a function of ζ for each streamline in Figs. 38, 39 and 40, for the entrance vanes, the rotor, and the stator respectively. From these graphs the flow angles at the blade edges were taken. These angles together with the corresponding angles at infinity were plotted as functions of the radius in Figs. 41, 42, and 43. These graphs show that the difference in angle is less than $1/2^{\circ}$ over the main portion of the blades and is still only of the order of 1° at the root and tip. This deviation is believed to be less than those due to real fluid effects. For this reason, for the design of compressor blading on the basis of perfect fluid theory, it seems quite satisfactory to calculate blade angles from the equilibrium flow pattern which exists at a large distance from the actual blades. This is what has been done in the design theory presented in section 3:1.

A further assumption, which was made in the development of theory for calculating the performance of an arbitrary blade set, can also be checked by this example. In section 3:1 the ratio of the radii of a given streamline

far and behind the blade row, was taken to be equal to unity. The actual ratios may be determined from the plot of streamlines in Figs. 44 and 45. The largest ratio exists near the center of the annulus and is equal to about 1.03 in both cases. This is sufficiently close to unity to justify the foregoing assumption.

The case under consideration involves a fairly extreme type of flow profile. Nevertheless, the assumptions of the simplified theory were shown to be adequate when examined in the light of the results of the more elaborate theory. This specific example, therefore, may be taken as one indication that the compressor theory presented in section 3:1 will yield satisfactory results.

IV. Experimental Investigation of The Validity of The Compressor Theory.

4:1 Purpose of The Experimental Work

In section 3:1 a theory for the flow through an axial compressor was presented. It was shown that the theory allows the solution of the "indirect" as well as of the more difficult "direct" problem. The "indirect" problem consists of finding the blade shape to obtain a given flow pattern, whereas the "direct" problem consists of finding the flow pattern resulting from a given blade shape. The first is used mostly for design studies whereas the second is used for predicting the performance of a particular blading. It is the purpose of this chapter to examine the theory in the light of experimental results.

The theory is based on a number of assumptions. These assumptions are of different types and their role in the development of the theory is discussed in the following paragraphs.

The first assumption postulates the fluid to be perfect: i.e., there are no losses of any kind. This assumption is a frequent one in fluid dynamics and it is believed that, at normal flow conditions, pressure and flow characteristics as well as the corresponding blade shapes can be calculated on this basis. It is on this same basis

that the lift and induced drag are calculated for airplane wing shapes. For the computation of efficiency and stall characteristics the viscosity of the fluid has, of course, to be taken into account. At normal flow conditions, however, the viscous effects are not expected to change the general flow pattern and pressure distribution to any large extent. The perfect fluid assumption is made so frequently that it will not be regarded as particular to the present theory.

The second assumption concerns the leaving angle from the blade rows. For a blade row with infinitely close spacing this angle is determined by the tangent to the trailing edge. For a finite spacing, the leaving angle is more difficult to predict. Several methods were discussed in section 3:4.2, and with the collection of further experience more satisfactory methods will probably be evolved. In the present compressor theory, however, the leaving angle is assumed to be given, and the methods of determining the properties of a cascade with finite blade spacing should again be regarded as auxiliary assumptions. As a secondary result it was hoped to obtain some information on the relative merit of methods for cascade angle determination, as well as on the effect of this angle assumption on the computed results. For this reason, computations were carried out with two different assumptions

for the leaving angle. The two assumptions in question are the following:

(a) The outlet angles were assumed to be independent of the inlet angle and were taken to correspond to an air deflection angle of

$$\theta^* = \theta_c \left(1 - 0.26\sqrt{s/c}\right)$$

where θ_c is the blade camber.

(b) The outlet angles were assumed to be equal to those obtained in the flow of a perfect fluid through a two-dimensional cascade of thin airfoils having the same camber lines as the actual airfoil sections. The flow about these thin airfoils was obtained from an approximate conformal transformation of the flow about a cylinder (Ref. 4).

The third assumption, or group of assumptions, consists of those which are particular to the compressor theory. These assumptions include the following:

(a) The ratio of the radius of a particular stream tube in front of a blade row to the radius of the same stream tube behind the blade row is assumed to be unity.

(b) The equilibrium flow pattern which theoretically is reached only at an infinite distance behind the blade row, is assumed to be fully developed at

the trailing edge of the blade row.

(c) The flow is assumed axially symmetrical.

It is on these assumptions that the simplifications of the theory are based and it is these assumptions in particular which are to be checked against the experimental results. For the comparison, therefore, operating conditions will be selected under which the first two assumptions will be satisfied. Agreement between experiment and theory under these conditions will then be interpreted to mean that the special assumptions of the theory are valid. Information on the validity of the first two assumptions will be derived wherever possible.

For the investigation, single stage tests with the "free vortex" and the "solid body" blade types were carried out. Detailed flow patterns as well as overall performance data were secured in each case.

4:2 Analytically Computed Flow Data

Using the compressor theory of section 3:1, the axial velocities behind the entrance vanes (φ_1), behind the first rotor (φ_2), and behind the first stator (φ_3) were computed. The equations for these axial velocities are:

$$\varphi' = \kappa \sin \gamma_i \; e^{-\int_{\gamma_i}^{\gamma} \frac{\cos^2 \gamma_i}{\gamma} d\gamma} \qquad (8a)$$

$$\varphi_2 = \sin\beta_2 \, e^{-\int_{\xi_i}^{\xi} \frac{\cos^2\beta_2}{\xi} d\xi} \left\{ \int_{\xi_i}^{\xi} \left[2\cos\beta_2 - \frac{\sin\beta_2}{\varphi_1} \frac{d}{d\xi}(\xi\lambda_1) \right] e^{\int_{\xi_i}^{\xi} \frac{\cos^2\beta_2}{\xi} d\xi} d\xi + K \right\} \qquad (8b)$$

$$\varphi_3 = \sin\gamma_3 \, e^{-\int_{\xi_i}^{\xi} \frac{\cos^2\gamma_3}{\xi} d\xi} \left\{ \int_{\xi_i}^{\xi} \frac{F}{\varphi_2} \sin\gamma_3 \, e^{\int_{\xi_i}^{\xi} \frac{\cos^2\gamma_3}{\xi} d\xi} d\xi + K \right\} \qquad (8c)$$

The equations were derived in section 3:1.3. Knowing the axial velocity components, the tangential components are computed by means of the relations

$$\lambda_2 = \xi - \varphi_2 \cot\beta_2 \qquad \text{(behind the rotor)}$$

and

$$\lambda_1 = \varphi_1 \cot\gamma_1 \qquad \text{(behind the entrance vanes)}$$

where γ_1 is the absolute and β_2 the relative exit angle. The work coefficient was then computed at each radius from the equation

$$\psi = 2\xi(\lambda_2 - \lambda_1)$$

The equations for the axial velocity components cannot in general be solved analytically, and the result must be obtained by graphical or numerical computation. By means of the foregoing relations, the velocities and total pressures were computed for the flow behind the first rotor

and behind the first stator. The computations were carried out for both blade types - - - the "free vortex" blading and the "solid body" blading - - - and for flow rates at and off the design point. Two complete sets of calculations were carried out. For the first set of calculations the blade exit angles were determined on the basis of Constant's rule and the second set was prepared using the exit angles obtained on the basis of cascade transformation. The angle assumptions for both blade types are presented graphically in Figs. 47 to 49.

A sample of each type of calculation is shown in Tables 12 and 13. In both examples the flow behind the first stator of the "free vortex" blading is computed for an average axial velocity of $\bar{\varphi} = .35$. In the first case the stator exit angle is assumed to be known and independent of the entrance angle and can therefore be entered immediately for all flow rates. In the second case, the cascade entrance angle is first computed, and the corresponding exit angle, β_3 is obtained from a cascade transformation (see Fig. 48).

The results of the computations for the "free vortex" blading are presented in Figs. 50 to 55. In Fig. 50 the axial velocity at each radius behind the rotor, φ_2 , (using Constant's rule) is plotted as a function of the average axial velocity, $\bar{\varphi}$. A similar graph for the

velocity behind the stator is given in Fig. 51. The total pressure increase, ψ , (which is equal to the work done in the ideal frictionless case) is shown in Fig. 52 again as a function of the average velocity, $\bar{\varphi}$. The results for the second set of computations (using the angles obtained from conformal transformations) are given in Figs. 53 to 55. The corresponding results for the "solid body" blading are given in Figs. 56 to 59.

4:3 Experimental Flow Data

For the comparison with the computed data, experimental measurements of velocity direction, velocity and total head were made at various flow rates. Flow rates including about $\pm$ 20% off the design value were covered. Measurements were made behind the first rotor of the "free vortex" blading, behind the first rotor of the "solid body" blading and, in case of the "free vortex" blading, measurements behind the first stator were also made. For the tests behind the rotors a row of entrance vanes and the first rotor itself were installed. For the stator tests, the above blade rows and the first stator, but no additional blade rows were installed. The angle measurements were taken with the cylindrical yaw probe, and both the velocity and total head were measured by means of the pitot static tube. The Statham Gage (sec. 2:2) was used as pressure

pickup in both cases. The angles, in each case, were determined first and were then used in setting the pitot tube. For both traverses the tube was held in the instrument carriage (see sec. 2:2). The measurements are therefore taken in a plane about 1/2 chord length behind the trailing edge.

It is also to be pointed out that the measurements behind the rotor were made with the stator removed. The resulting flow pattern will, however, be very nearly the same as that with the stator in place, since the influence of the stator does not reach far upstream, as can be seen by inspecting the results of section 3:5.

No provision was made for extensive measurements behind the entrance vanes, as this was not believed necessary. Only a few radial surveys of flow direction and total pressure were made and, where needed, the velocity was calculated neglecting losses through the vanes.

As mentioned before, the purpose of the experiments was to compare experimental data with calculated values, and in particular it was desired to check the assumptions within the perfect fluid theory. For this reason, wherever possible, the measurements were taken in a part of the fluid which was little influenced by frictional effects and could be expected to behave like a perfect fluid. This means in general in the main body of the flow, i.e. the entire

region outside of the boundary layer and blade wakes. For the measurements behind the rotor this comprises practically the entire annulus excepting about 3/4 inch near the walls. An inspection of a survey behind the rotor (Fig. 60a) shows that the variations due to the entrance vane wakes are very slight and that the measured values do not change much with circumferential position. The regions showing slight shadows were, however, avoided, and a radial survey at a position free from entrance vane wake effects was taken as representative. The effect of the rotor blade wakes themselves could, of course, not be separated with the present test installation. The average velocities and pressures obtained in this way are, however, not influenced much by these wakes. This is again verified by the close agreement of the compressor flow rates computed from entrance duct measurements and detail surveys (see table 3). In the case of the measurements behind the stator, the data were taken in the region between wakes and outside the strip near the walls. The location of the wakes was previously determined by a complete total head survey, an example of which is shown in Fig. 60b.

4:4 Basis of Comparison of Experiment With Theory.

Comparison was based on the following procedure: A certain flow rate, as indicated by the wall pressure of the

inlet duct was selected. At this overall flow rate, radial surveys of flow direction, velocity, and total head were made behind the first rotor and the first stator at the aforementioned tangential positions. An average axial velocity, $\bar{\varphi}'$, corresponding to the main body of the fluid was then obtained by averaging from a radius of $\xi = .65$ to $\xi = .95$. The average $\bar{\varphi}'$ defined in this manner was then used as a basis of comparison and the corresponding calculated values were obtained from the graphs presented in the previous section. Axial velocities measured behind the stator were in general higher than those measured behind the rotor because the stator blades (or the corresponding wakes) essentially reduce the available through-flow area. To correct for this reduction in area, each axial velocity measured behind the stator was adjusted by a constant factor of such magnitude that the average $\bar{\varphi}'$ was the same as that obtained from the measurements behind the rotor.

4:5 Presentation of Data

The data are presented in a number of graphs. For each flow rate two graphs were prepared as follows. The first shows the experimental and theoretical axial velocity components behind the rotor as a function of radius, and the second graph shows the same comparison for the total head. Such information has been prepared for the measure-

ments behind the "free vortex" and "solid body" rotor and for those behind the "free vortex" stator. As to the total head behind the stator, it should be pointed out that the calculations, of course, indicate the same profile behind the stator as behind the rotor, because no energy change occurs in passing through the stator, and the streamline shift is negligible (see sec. 3:5). In further graphs the blade exit angle from each blade row is shown for each radius as a function of the previously defined average velocity φ'. This same information is also replotted in a graph showing the exit angle vs. the inlet angle in each case, which is a common way of presenting cascade data. On each of the foregoing graphs the angles corresponding to the two assumptions (see 3:4) are also indicated.

The methods of taking measurements and the basis of comparison having been defined, the experimental work will be analyzed in the following section.

4:6 Discussion of Results Obtained With the "Free Vortex" Blading.

4:6.1 Cascade Angle Characteristics.

As was pointed out before, the validity of the principal assumptions of the theory can be checked best when the flow conditions are such that the angle assumption and the perfect fluid assumption are well satisfied. This

point will therefore be considered first, and with this in mind the cascade characteristics are examined. In Figs. 61 and 62 such information is presented in the form of a graph of the leaving angle vs. the entrance angle for various sections of the rotor and stator respectively. In addition to this experimental data the exit angle predicted by Constant's rule and that predicted by the cascade transformation are also indicated.

("Free Vortex" Rotor)

Let the data for the rotor be analyzed first. The points which are marked on each curve (Fig. 61) correspond to flow rates, the points toward the right representing the highest flow rates. (To show the relation of the leaving angle to the flow rate Fig. 63 was prepared.)

It is then seen that for the larger flow rates the experimental data agree well with the assumed values at least for the upper 2/3 of the blade. The discrepancy from the angles computed by Constant's rule is of the order of one degree only and the discrepancy from the cascade transformation is slightly larger. Also, the angle remains fairly constant over a certain range of flow which is in agreement with the assumptions. At lower flow rates, however, the leaving angle decreases considerably below that predicted. Near the hub the condition of decreasing

leaving angle exists even at the larger flow rates, and good agreement with the assumed angles exists only at the highest flow rate. At the very low flow rates, on the other hand, the section closest to the hub (ξ = .633) shows a reverse trend.

The characteristics exhibited by the upper sections of the compressor blade are also noticed in tests with two-dimensional cascades, as has been found in the literature. Some of these data are reproduced in Figs. 67 and 68. The camber, the range of entrance angles, and the solidity, (s/c) are of the same order of magnitude in the two-dimensional as in the compressor cascades. Two rotor sections have actually a sufficiently close geometric correspondence to allow them to be plotted on the same graphs. (Figs. 67 and 68) A comparison of these two sets of data shows such a close agreement that it seems permissible to conclude that for the case under discussion, the blade sections in the compressor have characteristics similar to those of the corresponding two-dimensional cascades.

Again there is a range where the outlet angle is insensitive to changes of the inlet and a range in which the leaving angle decreases considerably with inlet angle. This decrease is not predicted by perfect fluid theory and is, therefore, believed to be caused by real fluid effects. Further information on this question is obtained by in-

specting the pressure loss data given for the two-dimensional cascades. These data show that the drop off in leaving angle is associated with a considerable increase of the losses. This then is the same phenomenon as the "stall" in case of a single airfoil. The stalling of the cascade will usually be more gradual owing to the influence of neighboring airfoils, and some drop off in leaving angle may occur before the loss becomes severe. The angles below which for each cascade the losses become large are indicated*. Some loss measurements were also made in the compressor directly, and these loss characteristics were shown to be similar to those of the two-dimensional tests (Ref. 4).

The angle data from the rotor (Fig. 61) may now be interpreted in the light of this discussion. The sections of the rotor in the upper half (ζ = .8, ζ = .9, ζ = .967) operate in the "flat range" for most of the flow rates tested, and the losses are therefore expected to be small. In this range, as was pointed out, the magnitude of leaving angle is well predicted by the assumptions. In the present example Constant's rule seems to give the angles

* The losses become high again if the inlet angle increases above a certain value. Angles of such magnitudes are, however, outside of the range of the reported tests.

somewhat closer. At the low flow rates, however, these sections enter the "cascade stall". The leaving angle decreases with further decrease of the inlet angle (corresponding to a decrease in the flow rate) and the losses are expected to increase. The sections nearer the hub (ζ = .633, ζ = .7) are operating close to the "cascade stall" even at the high flow rates, and the leaving angle decreases with decreasing inlet angle even then. The magnitude of the leaving angle is not well predicted by the angle assumptions, and higher losses should be expected. The upswing of the curve at the very low flow rate is not a real cascade effect but is caused by the rotating hub. At the hub itself the velocity of the air must be equal to that of the hub because of the viscosity of the air. The direction of this velocity would be $\beta_2 = 180^\circ$. At small distances from the hub (e.g. at ζ = .633) this influence is still noticeable and brings about the upswing of the curve. The influence diminishes of course with the distance from the hub. At ζ = 0.7 it produces only a flattening of the angle curve and no effect is noticeable any more at ζ = 0.8. The effect is apparent only when the axial velocity components are low, i.e., at the low flow rates. At the high flow rates the velocity induced by the hub is not sufficient to produce any detectable change in the flow angle.

On the basis of the foregoing discussion one may select the flow conditions for which the velocity profiles behind the rotor can best be compared to the computed profiles. Fig. 61 shows that at the highest flow rate ($\bar{\varphi}' = .504$) the leaving angles at all sections are in quite good agreement with the assumed values. (Constant's rule, in this case, gives the slightly better values.) Furthermore, all the upper sections ($\zeta = 0.8;\ 0.9;\ 0.967$) are within the "flat range" and even the sections near the hub ($\zeta = 0.7;\ 0.633$) seem not far from this range, so that the losses are expected to be small everywhere. This high flow rate should, therefore, be selected for the comparison of flow patterns behind the rotor for the purpose of checking the assumptions of the compressor theory.

("Free Vortex" Stator)

The angle measurements for the flow through the stator are shown in Fig. 62, in which the leaving angles from the stator, γ_3, are plotted as a function of the corresponding inlet angles, γ_2. (The leaving angles are also plotted as a function of flow rate in Fig. 64). The general characteristics of these curves are the same as those described for the rotor. The characteristics for two of the stator sections are entered on the graph of the

two-dimensional cascades (Fig. 66) and very close agreement is seen to exist. All of the stator sections considered are used in the flat range for most of the flow rates tested, and only at the lowest flow rates do the effects of "cascade stall" become apparent. The effect of the rotor hub is also discernible for the section $\zeta = .633$. This time it causes a rapid decrease of the leaving angle at low inlet angles, because the velocity of the hub corresponds to a leaving angle $\gamma_3 = 0$.

At the high flow rates the magnitudes of the measured angles are quite close to those predicted by the assumptions. The two assumptions give very similar results, however, Constant's rule again compares better with the measured direction. By the same reasoning as before, the losses are also believed to be fairly small at these flow rates. This was verified by direct measurements at one point of the compressor, i.e., at the section $\zeta = .8$, of the stator (Ref. 4).

As was seen before, the first two assumptions (low losses and correct leaving angles) were satisfied at a high flow rate ($\bar{\varphi}' = .504$) for the rotor and it is now seen that these conditions are also satisfied for the stator at this flow rate. This flow rate, therefore, is also satisfactory for analyzing the flow pattern behind the stator.

("Free Vortex" Entrance Vanes)

As was mentioned in section 4:3, the compressor was not designed for extensive measurements behind the entrance vanes. Consequently, only a few measurements were made at this station to check approximately if the expected flow conditions existed. These data show that the flow direction behind the entrance vanes was within about 2° of the expected directions. This agreement is believed to be sufficient to allow satisfactory comparisons to be made for the flow profiles behind the rotor and stator. The angle data for the entrance vanes are given in Fig. 69.

4:6.2 Velocity Profiles - ("Free Vortex" Blading)

The axial velocity as measured behind the first rotor at a flow rate of $\bar{\varphi}' = .504$ is shown in Fig. 70a as a function of radius, ζ. The calculated profiles are also indicated. (The profiles calculated by the two angle assumptions are practically identical as both assumptions lead to about the same value). A comparison of the measured profile with the calculated one then, shows perfect agreement. This agreement is the first test which indicates that the particular assumptions of the compressor theory are valid. It is also to be pointed out that the flow rate in question ($\bar{\varphi}' = .504$) is above the design

point, so that some three-dimensional flow exists, although the blading is of the "free vortex" type. The flow profile behind the stator at the same flow rate ($\bar{\varphi}' = .504$) (Fig. 70b) is again in very good agreement with the calculated data. This is taken as a further verification of the assumptions of the theory.

Additional flow profiles behind the rotor and the stator are given in Figs. 71 to 74. These profiles are for the flow rates $\bar{\varphi}' = .463, .419, .394$, and $.354$. The figures show that the agreement between measured and calculated values becomes gradually worse as the flow rate is decreased. The differences are caused in part by the deviation of the angles and in part by the losses. Although the agreement of the profiles at the lower flow rates is not good, nevertheless the calculated profiles still indicate the same tendencies as the measured profiles, and some information on the behavior of the flow at low flow rates is still obtained.

Graphs summarizing the calculated and measured velocity profiles for various flow rates are given in Figs. 75a, b and 76a, b for the rotor and stator respectively.

4:6,3 Total Pressure Profiles - ("Free Vortex" Blading)

Before inspecting the total pressure profiles the

losses which occur upstream of the measuring station should be recalled. The total pressure is measured behind the rotor (γ_2) and behind the stator between blade wakes (γ_3). The atmospheric pressure is used as a basis for the total pressure measurements. At a station behind the rotor, therefore, the air has lost total pressure as a result of friction in the entrance duct, in the entrance vanes, and in the rotor itself. The further losses incurred in passing through the stator row are largely excluded by taking measurements in between wakes.

In comparing calculated with measured profiles, the aforementioned losses have to be kept in mind. From some surveys in front of the entrance vanes, the approximate losses in the entrance duct have been determined (Fig. 89). The losses are seen to amount to about 2% at the lowest flow rate ($\bar{\varphi}' = .354$) and to as much as 8% at the higher flow rates. The losses through the entrance vanes themselves seem to be very small. Any difference in measured and calculated total head beyond the amount accounted for by the duct losses indicates either that cascade losses occurred or that less work was done on the air than was calculated.

The measured total head profile behind the rotor at a flow rate of $\bar{\varphi}' = .504$ is shown in Fig. 70c. On the same graph the calculated profiles are given. The shapes

of the two profiles are practically identical. There are some differences in the magnitudes, but if the duct loss is taken into account the remaining difference is very small and can easily be accounted for by small friction losses through the blade row itself. The two profiles are, therefore, said to be in excellent agreement, and their agreement constitutes additional proof of the validity of the compressor theory.

Since there is no addition of energy in the stator, the total head profile is practically unchanged, and the same comments apply to the profiles behind the stator.

The pressure profiles for the lower flow rates ($\bar{\varphi}' = .463, .419, .394$ and $.354$) are given in Figs. 71c to 74c, and Figs. 71d to 74d for the rotor and stator respectively. As in the case of the velocity profiles, the agreement between calculated and measured profiles becomes less perfect when the flow rate is reduced. This is again caused by the deviation of the flow direction from the assumed one and by the increasing cascade losses. The general tendencies of the total pressure profiles at low flow rates is still fairly well represented, and in spite of the deviation the calculations for the low flow rates are still sufficiently close to the measured values to be used for the prediction of the overall performance. This will be discussed in connection with the overall

performance data in section 4:8. Graphs summarizing calculated and measured total pressure profiles are shown in Figs. 75c, d and 76c, d for the rotor and stator respectively.

4:7 Discussion of Results with the Solid Body Blading

4:7.1 Cascade Angle Characteristics

("Solid Body" Rotor)

The leaving angle from the rotor of the "solid body" blading is presented as a function of the inlet angle for various blade sections (See Fig. 77). The angles are also given as a function of the flow rate in Figs. 78 and 79. The angles predicted from Constant's rule and from the simplified cascade transformation are also indicated. It is seen that predicted and measured values of the angles agree extremely well, in particular at the high flow rates. The angles obtained from the cascade transformation are possibly somewhat closer in this case. Furthermore, all sections operate in the "flat range" of the angle curve for all except the lowest flow rates. There is no noticeable hub effect because, with the "solid body" type flow pattern the velocities near the hub are still relatively high, even at the lowest flow rate in question.

Before drawing any conclusions on the losses,

however, a further aspect has to be considered. The flow through the rotor of the "solid body" blading requires a considerable change in the axial velocity component. This change is more prominent than that at the off design conditions of the "free vortex" blading, although some change of axial velocity component occurred even there. This change in the axial velocity component means either more or less diffusion through the compressor cascade (depending on whether the axial velocity component increases or decreases) than would occur through a similar cascade having essentially two-dimensional flow. For the "solid body" blading at the flow rates tested, the axial velocity increases through the lower part of the rotor blades and decreases through the upper part. At the tip section, in fact, the blades hardly turn the air, and almost pure diffusion takes place. Whenever three-dimensional flow causes such additional diffusion, changes from the loss characteristics of a two-dimensional cascade should be expected.

The angle properties of three of the rotor sections were plotted together with the previously used characteristics of the two-dimensional cascades in Figs. 80a, b, c. The geometry of the two-dimensional cascades differs more from that of the "solid body" blade sections than it did in the case of the sections from the "free vortex" blading.

The comparison is therefore not quite as satisfactory, nevertheless some interesting observations can be made. In Fig. 80a, e.g., the angle characteristics of the rotor section ζ = .735 have been entered. The magnitude of the leaving angle is seen to be in line with that of the two-dimensional cascade, however, the "flat range" seems to extend further to the left, i.e., the "cascade stall" occurs at a lower inlet angle. This shift is explained by the increase in axial velocity which takes place at this section (ζ = .735). The adverse pressure gradient through the compressor section is less than that in the two-dimensional tests, and therefore the stall should be expected to occur at a lower inlet angle. Similarly, the losses will probably become severe only then. Near the center of the blade the change in axial velocity is small, and the data for such a section (ζ = .84) fit in well with the two-dimensional characteristics (See Fig. 80b). In the case of a section near the tip of the blade the conditions are the reverse of those at the root sections. The data for the section ζ = .95 are plotted on Fig. 80c. There are not sufficient two-dimensional data available to make an exact comparison in this case, and it is therefore difficult to appreciate the shift of the angle curve. The losses, however, may become considerable before a drop in leaving angle is noticed, because the sections near the

tip act principally as diffusers. Very little turning is required, but the losses which correspond to those of a straight diffuser certainly exist. At the highest flow rate tested ($\bar{\varphi}' = .499$) the amount of diffusion required is, however, small and the losses are therefore expected to be negligible.

The high flow rate ($\bar{\varphi}' = .499$) should, therefore, give satisfactory conditions for checking the particular assumptions of the compressor theory.

("Solid Body" Entrance Vanes)

As in the case of the "free vortex" blading, only approximate data could be obtained behind the entrance vanes. In fact the chords of the "solid body" vane sections were longer than those of the "free vortex" blading (especially near the tip) and at some radii the instrument heads were actually located a small distance (about $\frac{1}{4}$") inside the vane cascade. A slight correction was made to compensate for this error. The data are shown in Fig. 81. The velocity directions of the air leaving the vanes are seen to be close to the assumed values, although (as in the case of the "free vortex" vanes) the vanes produce somewhat less turning than expected. The entering conditions to the rotor are, however, sufficiently close to allow satisfactory comparisons for

the profiles behind the rotor.

4:7.2 Velocity Profiles ("Solid Body" Blading)

In the discussion of the cascade characteristics of the blade sections of the "solid body" rotor it was concluded that at a flow rate of $\bar{\varphi}' = .499$ the perfect fluid assumption was well satisfied and that the leaving angles were very close to those assumed. In Fig. 82a, the measured and the calculated velocity profiles at this flow condition are shown. The two profiles are seen to be in almost perfect agreement, which is taken as further proof of the validity of the compressor theory. This check is a particularly important one as the axial velocity component varies considerably from hub to tip. The older two-dimensional compressor theory would have assumed a constant axial velocity component, which would not have been a good approximation in this case. The present compressor theory, however, gives the very satisfactory approximation just mentioned.

The profiles for the lower flow rates ($\bar{\varphi}' = .466$, .427, and .392) are shown in Figs. 83a to 85a. These profiles are still in good agreement with the computed profiles, because the leaving angles still correspond very well to the assumed ones. The losses, which gradually increase at the lower flow rates, are believed to have only

a secondary effect on the flow profiles.

Graphs summarizing calculated and measured velocity profiles are shown in Figs. 86a and 86b.

4:7.3 Total Pressure Profiles ("Solid Body" Blading)

The total pressure profile at $\bar{\varphi}' = .499$ is shown in Fig. 82b. If (as in the case of the "free vortex" blading) the entrance duct loss is added to the measured profile, it is seen to be in very good agreement with the computed total pressures. The profile which was calculated on the basis of the cascade transformation angles gives a somewhat better comparison because these angles corresponded better to the measured angles, as seen from Fig. 77. Again the compressor theory is well verified by the comparison. It is interesting to note here that quite an erroneous total pressure distribution would have been obtained on the basis of the assumption that the axial velocity component is constant (see Fig. 82c).

The pressure profiles at the lower flow rates are given in Figs. 83b to 85b. The deviations from the calculated profile become gradually larger as the flow rate is reduced. This is due to the steadily increasing losses. However, as in the case of the "free vortex" blading, the general tendencies of the profiles are still correctly indicated by the calculations, and adequate prediction of

the overall performance will still be obtainable.

Two summary graphs giving calculated and measured total pressure profiles at the various flow rates are again shown in Figs. 86c and 86d.

4:8 Overall Performance of Both Blade Types.

The quantities which will be discussed under the heading "overall performance", are the average total head, the torque coefficient, and the efficiency as a function of the average flow rate. The above terms are defined as follows: The average total head

$$\bar{\psi}' = \frac{\iint \psi' \varphi \zeta \, d\zeta \, d\theta}{\iint \varphi \zeta \, d\zeta \, d\theta} \tag{29}$$

the work coefficient

$$\bar{\psi} = \frac{2\,(\text{Torque})}{A \rho \omega_0^2 r_0^2 \bar{\varphi}} \tag{30}$$

and the efficiency

$$\eta = \frac{\bar{\psi}'}{\bar{\psi}} \tag{31}$$

These quantities have been plotted as a function of flow rate in Figs. 87 and 88 for the "free vortex" blading and "solid body" blading respectively. The calculated work input (which is equal to the calculated total head

increase, because no losses are considered in the theory) is also shown in the figures.

Because the work coefficient, which is derived from the compressor torque, includes the losses, it is particularly suitable for comparison with the calculated work input. For both types of blading the calculated and measured curves for the work input are almost perfectly parallel. The analytical curves are slightly displaced towards higher flow rates, as the reduction of flow rate due to the boundary layers was not taken into account in the analytical work. The difference in both cases is of the order of 3% - 5% and can be predicted fairly well from experience. With this adjustment the calculated and analytical work coefficient curves become almost identical. This also means that the design point ($\bar{\varphi} = .45$, $\bar{\psi} = .40$) has been obtained very accurately for both blade types. The total head curves are located slightly below the work curve, the ratio of the two being the efficiency. Both blade types reach their peak efficiency very nearly at the design point. The two maximum efficiencies are about equal, being 89% for the "free vortex" blading* and 87% for the

* This efficiency was obtained at 750 rpm, which corresponds to a Reynolds' number of 80,000. According to experiments by Eckert (Ref. 7) (Fig. 90) an improvement of about 5% is to be expected at a Reynolds' number of 160,000, i.e., at 1500 rpm. Tests with three stages of the present compressor have verified these data (Ref. 4)

"solid body" blading.

It is interesting to point out that the two blade types, which have different properties and are quite different in appearance, actually do yield the same overall performance and that they both reach approximately the same high efficiency at the design point. This fact gives further credence to the compressor design theory and establishes the fact that a blading with a three-dimensional flow pattern can have a high efficiency.

4:9 Summary and Conclusions of Section IV.

In the preceding section (sec. IV) experiments with two blade types were discussed. The first type (the so-called "free vortex" blading) was designed for a two-dimensional flow pattern, the second type (the "solid body" blading) was designed for a three-dimensional one. The experiments were performed principally in order to evaluate the merits of a special theory describing the flow through an axial flow compressor (see sec. 3:1). As a secondary objective, it was desired to obtain some information on the characteristics of compressor cascades.

In the experiments, the fluid velocity, the flow directions, and the total pressures were measured behind the various blade rows for a number of different flow rates. In addition some data on the overall performance of the two

blade types were collected.

The measured flow profiles were then compared to those calculated by the aforementioned theory. In analyzing the calculated profiles with the aid of the experimental ones, it was found advantageous to classify the assumptions of the theory into three groups: the assumption that the fluid is perfect, the assumption concerning the direction of the flow leaving the blade rows, and the assumptions introduced to linearize and simplify the equations of three-dimensional flow. This latter group of assumptions was considered particular to the theory, and in accordance with the purpose of the experiments, the investigation of their validity was a major purpose of the tests. For the analysis of these assumptions, therefore, flow conditions were selected at which the first two types of assumptions were satisfied.

The overall performance was measured in order to obtain further comparative data and to determine whether or not a blade type having a "three-dimensional" flow pattern (the "solid body" blading in this case) can be as efficient as the "free vortex" blading, which, at the design point has a two-dimensional flow pattern.

On the basis of the experimental data of the previous section, the following conclusions were drawn:

(a) The applicability of the aforementioned com-

pressor theory has been demonstrated. The theory yields accurate results in predicting the flow characteristics of given blades at and off design conditions. This conclusion is based on comparisons of velocities and total pressures at flow conditions where the perfect fluid assumption and the assumption of the leaving angle were satisfied.

(b) The overall performance of the compressor in the neighborhood of the design point is predicted well by the theory. The analytical and experimental "work input" curves are almost identical, provided a small adjustment is made for the wall boundary layers.

(c) The design point (as determined by flow rate and work coefficient) is obtained closely by the blades designed from the compressor theory. The maximum efficiency coincides well with the design point.

(d) The "free vortex" blading as well as the "solid body" blading yields a high efficiency at the design point. This shows that a blading with three-dimensional flow can have an efficiency comparable to that of a "free vortex" blading.

(e) The leaving angles from the blade rows are quite insensitive to changes in the inlet angle for

a fairly wide range. Below that range (i.e., for the higher incidence angles and higher lift coefficients) the cascade begins to "stall". This causes a decrease of the leaving angle with decreasing inlet angle as well as a considerable increase in losses. The "stall" is usually less abrupt than in the case of a single airfoil, because of the mutual influence of the blades.

If the axial velocity through a section of a blade row remains fairly constant, the measured angle characteristics of the compressor blade sections are almost identical with the experimental data for a corresponding two-dimensional cascade. If, however, there is a considerable change in the axial velocity component, the "stall" point will be shifted and the losses will probably be different from those of the two-dimensional cascade.

(f) For the region in which the cascade leaving angle is fairly independent of the inlet angle, both assumptions used for predicting this angle (Constant's rule as well as the transformation method (see sec. 3:4.2)) give the magnitude of the angle to a good approximation. Each of the assumptions leads to very nearly the same values and, for the cases tested, one is not consistently better than the other.

(g) The assumption that the fluid is perfect is good as long as no part of the blade is stalled and there are no large diffusion losses through the blade sections. If large losses occur at any part of the blade, the compressor theory under investigation cannot be expected to yield very exact results even if the leaving angles were predicted accurately.

On the basis of the results obtained, it is seen that the compressor theory as presented in section 3:1 is based on justifiable assumptions, provided the losses are low and the characteristics of the cascade sections are known. Under these conditions the theory yields results well within the usually required engineering accuracy for both problems: the design of blades and the prediction of performance for given blades. If greater accuracy is required than can be obtained from the theory, or if performance predictions are to be made in a region of high losses (e.g., the "stall" region) viscous effects must be taken into account.

REFERENCES

1. Bowen, J.T., Some Viscosity Effects in Axial Flow Compressors. California Institute of Technology, Thesis, 1949.

2. Markowski, S. J. and Moffatt, F. M., Instrumentation for the Development of Aircraft Power Plant Components Involving Fluid Flow, Reprint, Society of Automotive Engineers, 1947.

3. Marble, Frank E., The Flow of a Perfect Fluid Through an Axial Turbomachine with Prescribed Blade Loading, Journal of the Aeronautical Sciences, Vol. 15, No. 8, August, 1948.

4. Bowen, J. T., Sabersky, R. H., and Rannie, W. D., Theoretical and Experimental Investigation of Axial Flow Compressors, Report to the Office of Naval Research, January, 1949.

5. Bogdanoff, Seymore M. and Harriet E., Blade Design Data for Axial-Flow Fans and Compressors, N.A.C.A., Wartime Report L-635, July, 1945.

6. Howell, A. R., The Present Basis of Axial Flow Compressor Design, Part I, Aero. Research Council, R. & M. 2095, June, 1942.

7. Eckert, B., The Influence of Physical Dimensions and Fow Conditions on Compressor Characteristics, Part A, Buships 338, The Navy Department, 1946.

APPENDIX I: NOTATION

The symbols defined below are generally used throughout the thesis. Special symbols, subscripts, etc., are defined in the body of the thesis where needed.

Symbol	Definition
A	Area of compressor annulus
c	Absolute velocity (in a fixed coordinate system)
c_a	Absolute axial velocity component
c_u	Absolute tangential velocity component
c_r	Absolute radial velocity component
C_L	Lift coefficient per unit length of airfoil
C_p	Static pressure coefficient
h_o, H_o	Blade length
p	Static pressure
p_t	Total (stagnation) pressure
P	Reaction ratio
r	Radius from center of rotation
r_o	Tip radius
s	Cascade pitch
u_o	Tip velocity
w	Velocity relative to a moving coordinate system

w_m	Relative mean velocity
z	Axial distance from blade row center
z, r, θ	Cylindrical coordinate system
β	Direction of relative velocity from plane of rotation
β_o	Stagger angle
γ	Direction of absolute velocity from plane of rotation
Γ	Circulation per unit length of airfoil
ζ	Dimensionless axial distance = z/r_o
η	Efficiency
θ_c	Cascade camber angle
θ^*	Air turning angle
λ	Dimensionless tangential velocity = c_u/u_o
μ	Dimensionless radial velocity = c_r/u_o
ξ	Dimensionless radius = r/r_o
ξ_i	Dimensionless hub radius (or hub ratio) = r_i/r_o
ξ_o	Dimensionless tip radius = r_o/r_o = 1
ρ	Fluid density
σ'	Cavitation coefficient
φ	Dimensionless axial velocity component
$\bar{\varphi}$	Dimensionless average axial velocity component
ψ	Local work coefficient
ψ'	Local total (stagnation) pressure rise coefficient
$\bar{\psi}$	Total work coefficient (Torque coefficient)

$\bar{\psi}'$ Average total pressure rise coefficient

ω Dimensionless angular velocity = $\omega_0 r_0 / a_0$

ω_0 Angular velocity

For " Diagrammatic Representation of Special Symbols" see next page.

DIAGRAMMATIC REPRESENTATION OF SPECIAL SYMBOLS

CASCADE NOTATION (ANGLES)

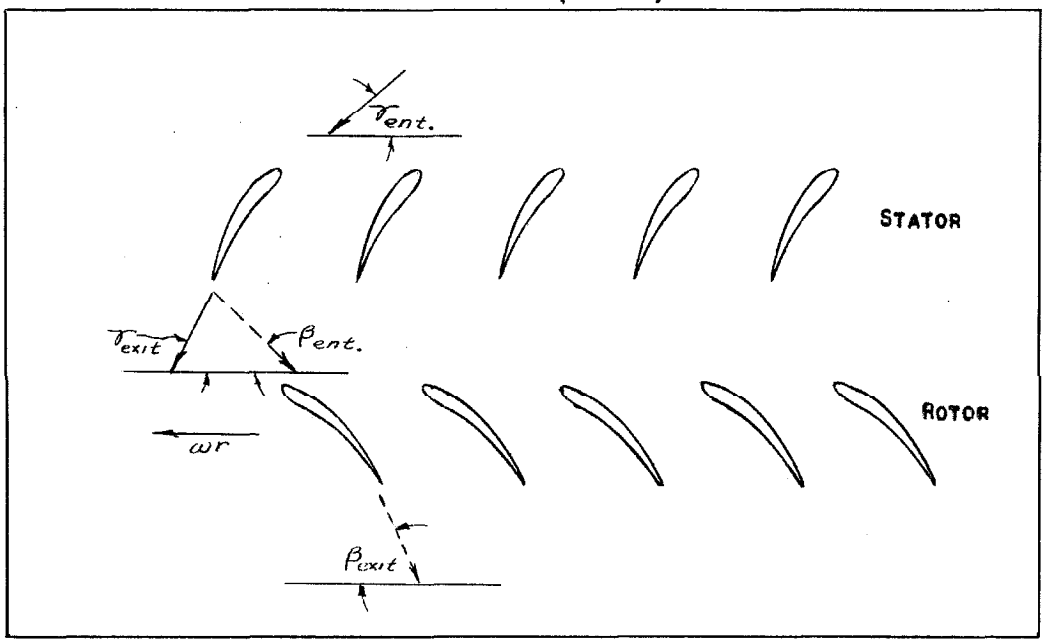

NOTATION CONCERNING FLOW THROUGH BLADE ROW

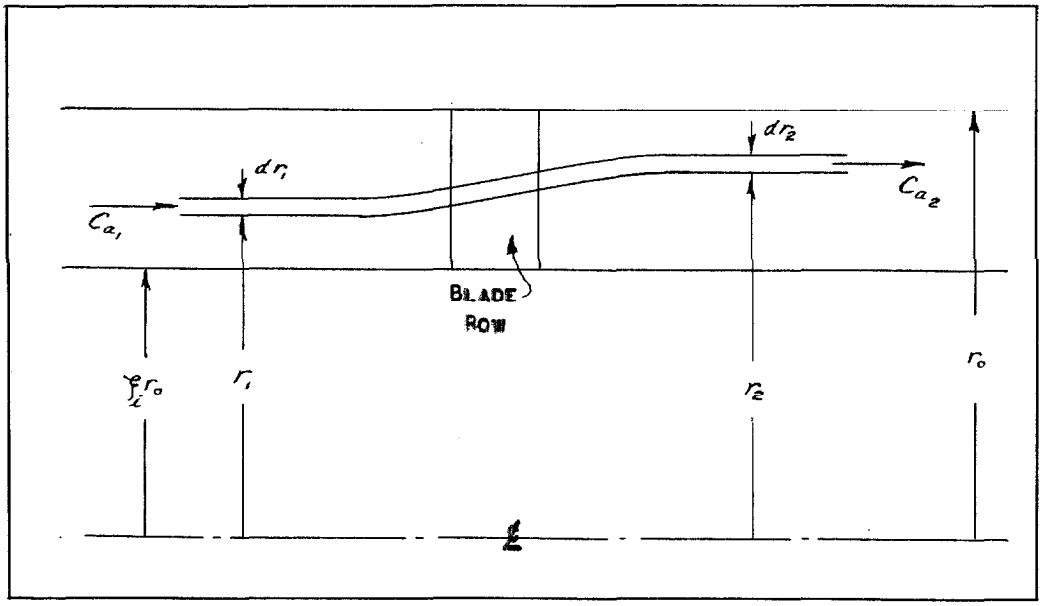

F I G U R E S

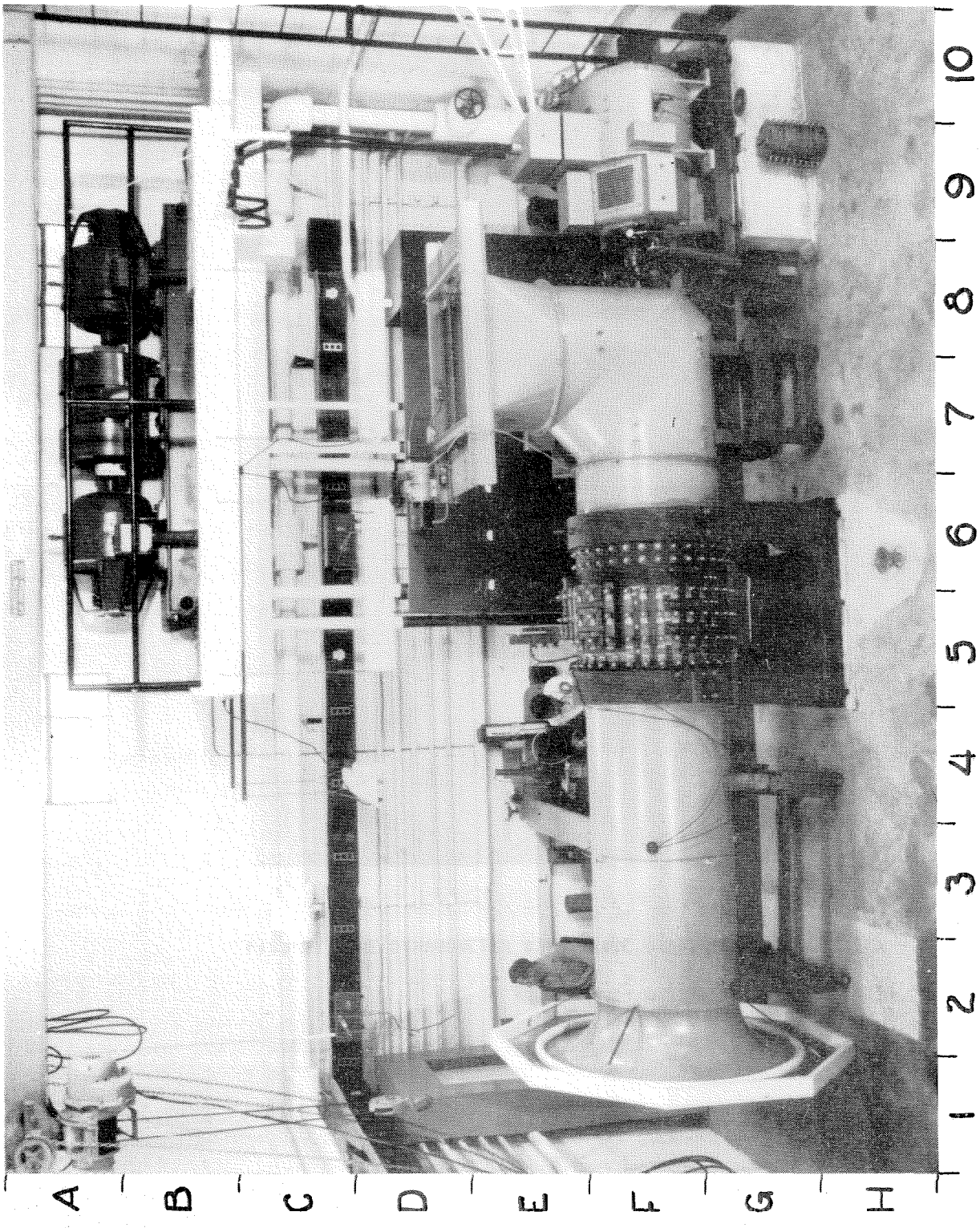

FIG. 1 GENERAL VIEW OF TEST INSTALLATION (SEE SEC. 2:1.1)

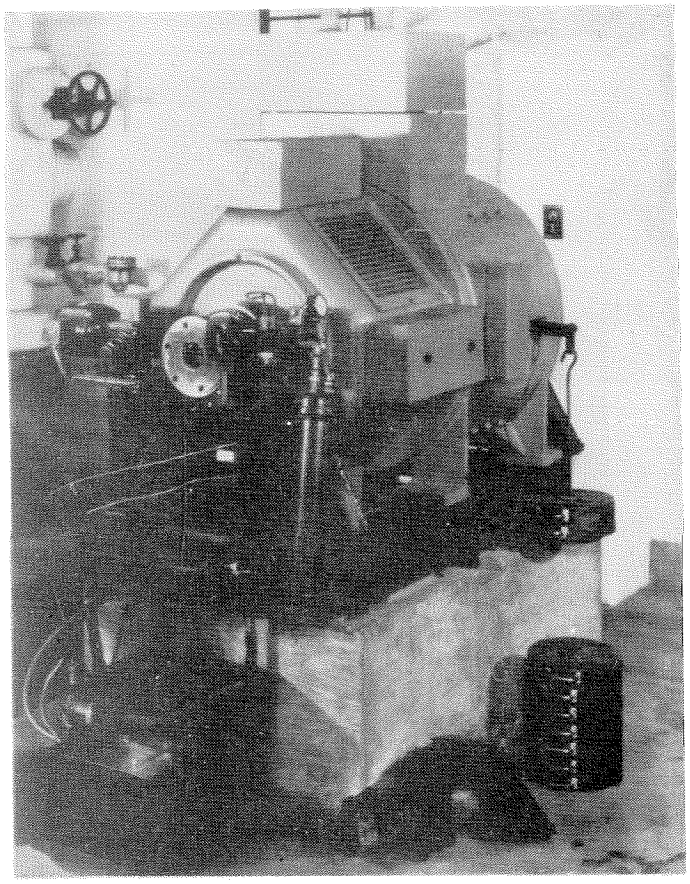

FIG. 2 THE DYNAMOMETER WITH DRIVE SHAFT REMOVED

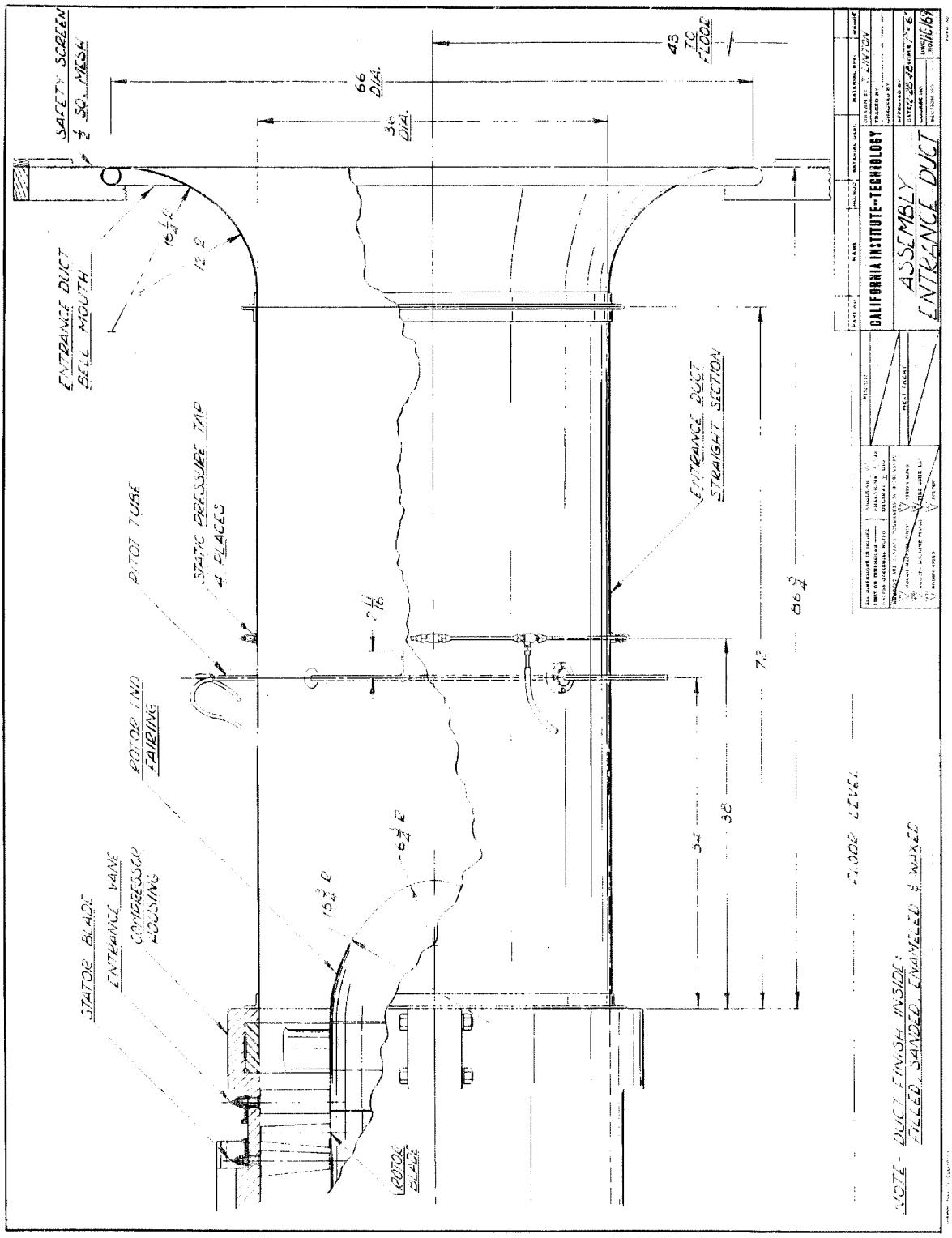
SAFETY SCREEN
½ SQ. MESH
ENTRANCE DUCT
BELL MOUTH
PITOT TUBE
STATIC PRESSURE TAP
4 PLACES
ROTOR END
FAIRING
STATOR BLADE
ENTRANCE VANE
COMPRESSOR
HOUSING
ENTRANCE DUCT
STRAIGHT SECTION
66
DIA.
36
DIA.
43
TO
FLOOR
CALIFORNIA INSTITUTE OF TECHNOLOGY
ASSEMBLY
ENTRANCE DUCT

FIG. 3

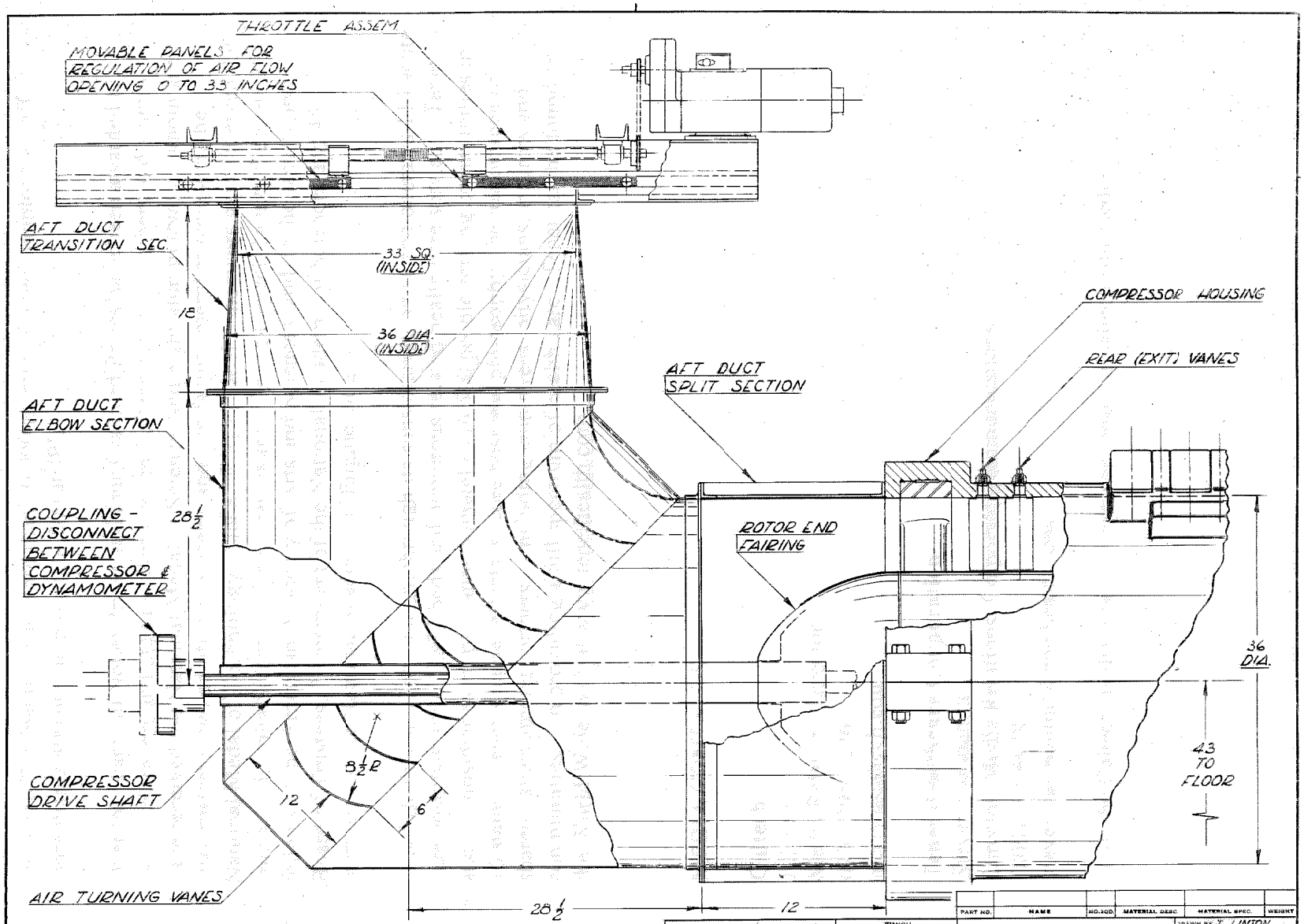

FIG. 4

PART NO.	NAME	NO. REQD.	MATERIAL DESC.	MATERIAL SPEC.	WEIGHT

ALL DIMENSIONS IN INCHES
LIMIT ON DIMENSIONS UNLESS OTHERWISE NOTED — ANGULAR ± ½° FRACTIONAL ± 1/64 DECIMAL ± .010

NUMBERS ARE SURFACE ROUGHNESS IN MICROINCHES
125 ROUGH MACHINE FINISH
63 SMOOTH MACHINE FINISH
32 ROUGH GRIND
16 FINISH GRIND
8 FINE GRND. LAP
4 POLISH

FINISH

HEAT TREAT

CALIFORNIA INSTITUTE OF TECHNOLOGY

ASSEMBLY AFT DUCTS

DRAWN BY T. LINTON
TRACED BY
CHECKED BY
APPROVED BY
DATE 1-18-49 SCALE 1" = 6"
COURSE NO.
SECTION NO.
DWG NO. 11-C-1170

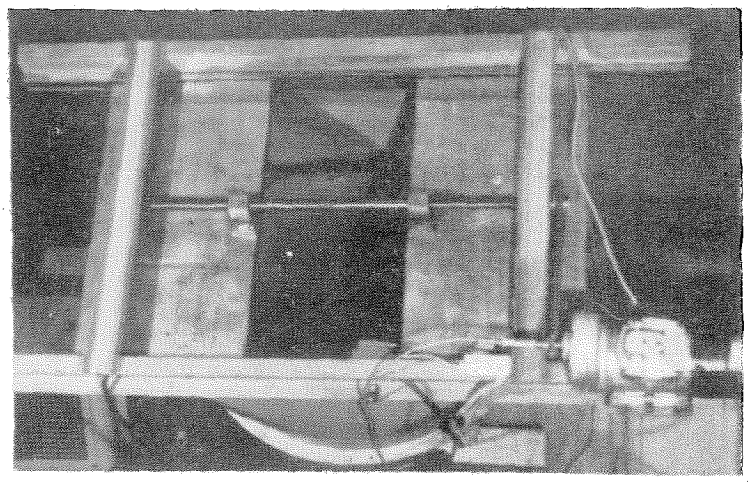

FIG. 5 THE THROTTLE VALVE

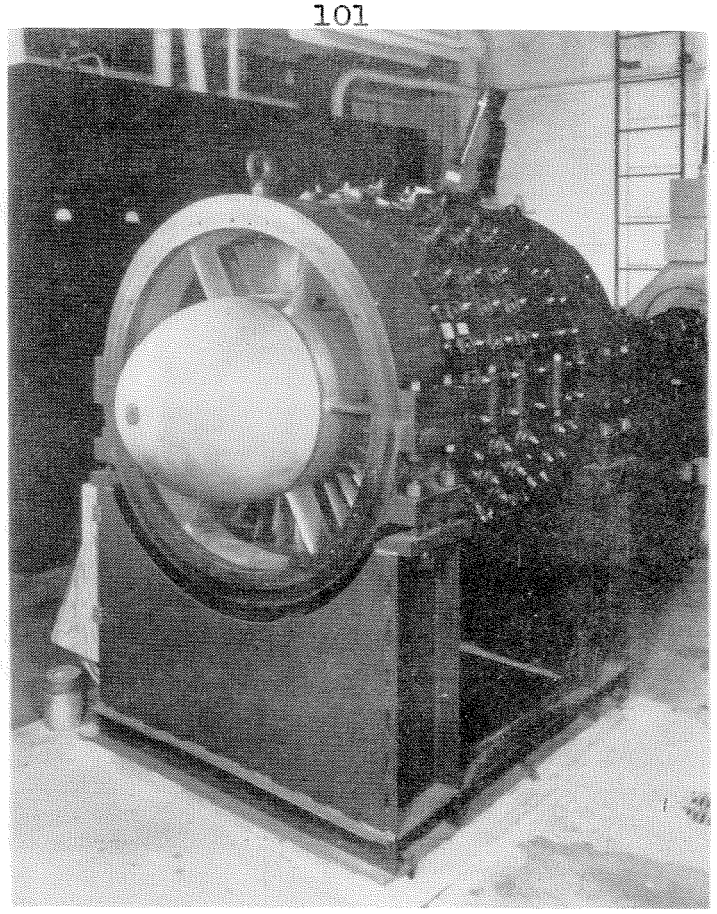

FIG. 6 ASSEMBLED TEST COMPRESSOR

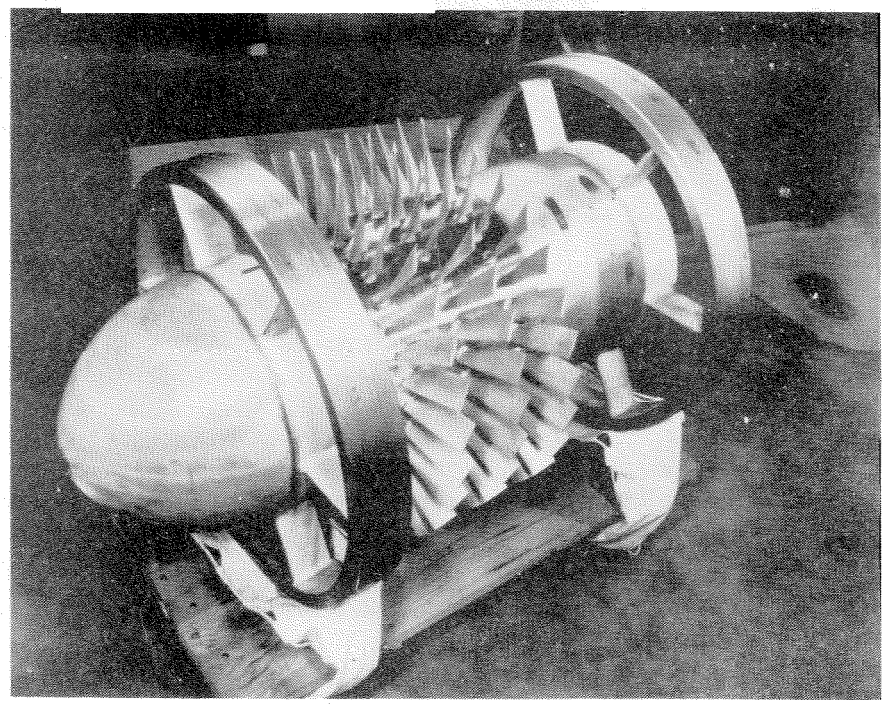

FIG. 7 ROTOR ASSEMBLY

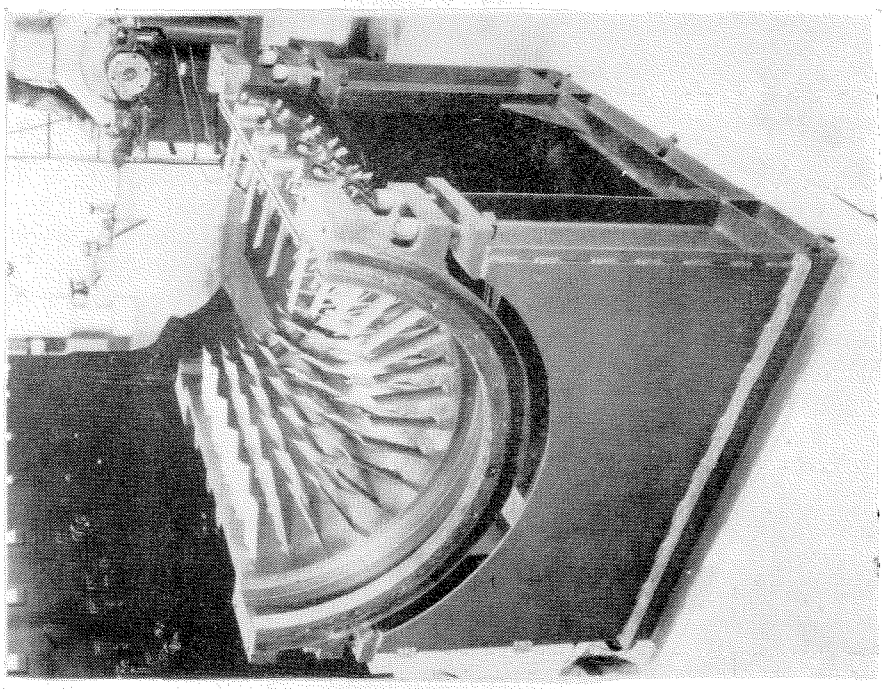

FIG.9 LOWER HALF OF COMPRESSOR CASE.

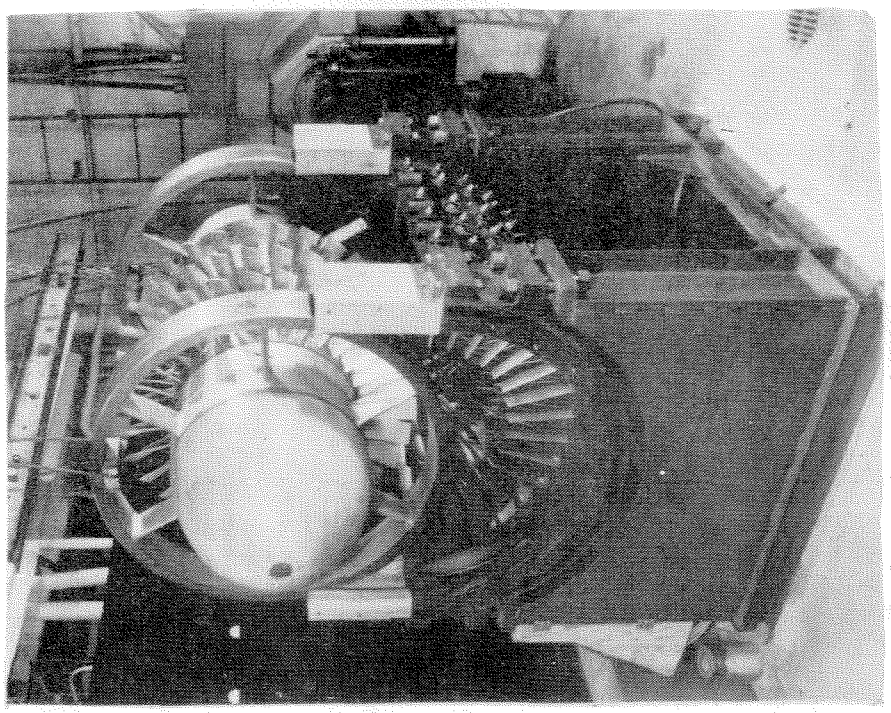

FIG.8 ROTOR ASSEMBLY BEING PLACED IN LOWER CASE.

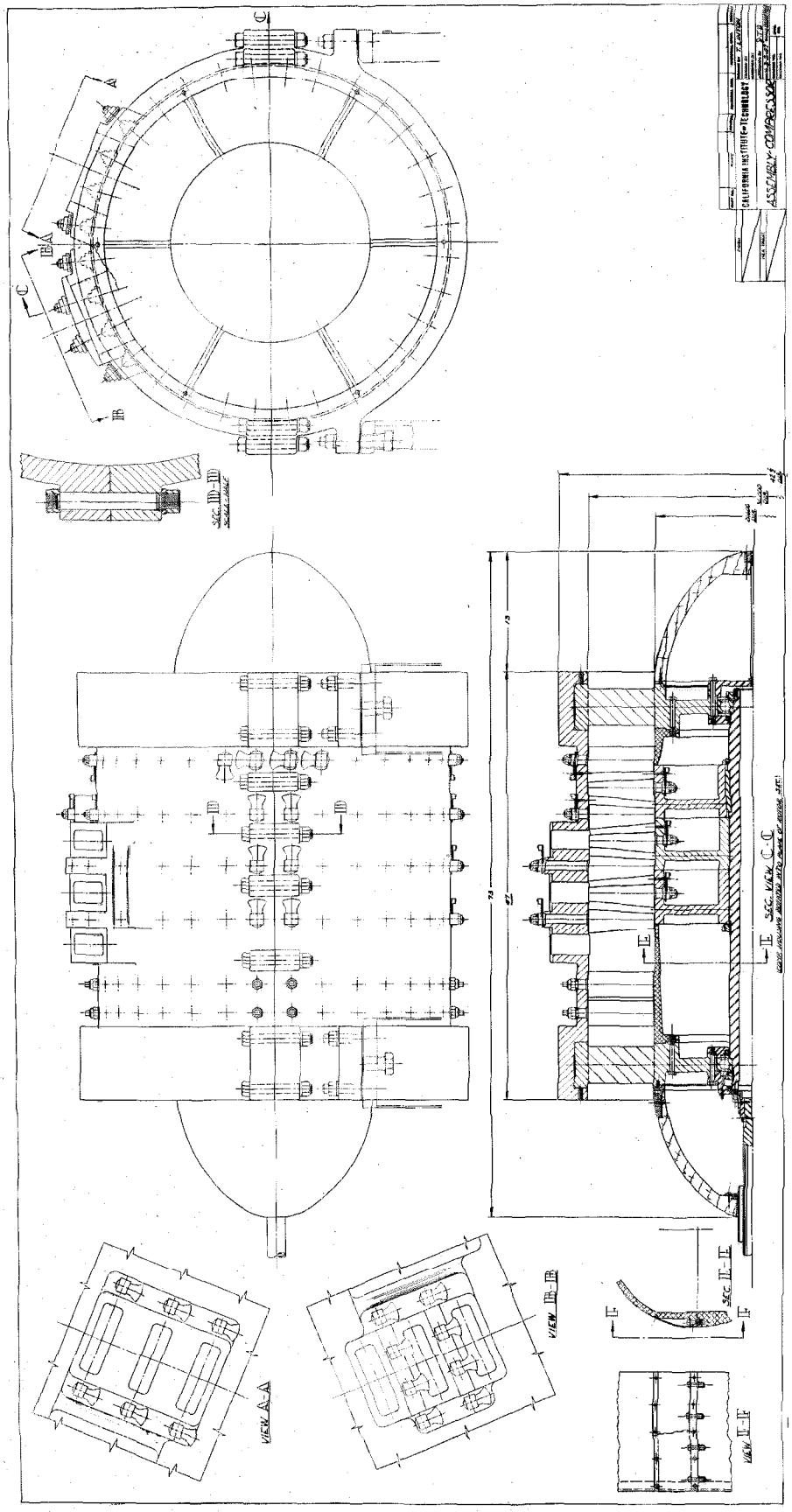
ASSEMBLY COMPRESSOR
SEC. III-III
SEC. II-II
VIEW A-A
VIEW III-III
VIEW II-F

Fig. 10

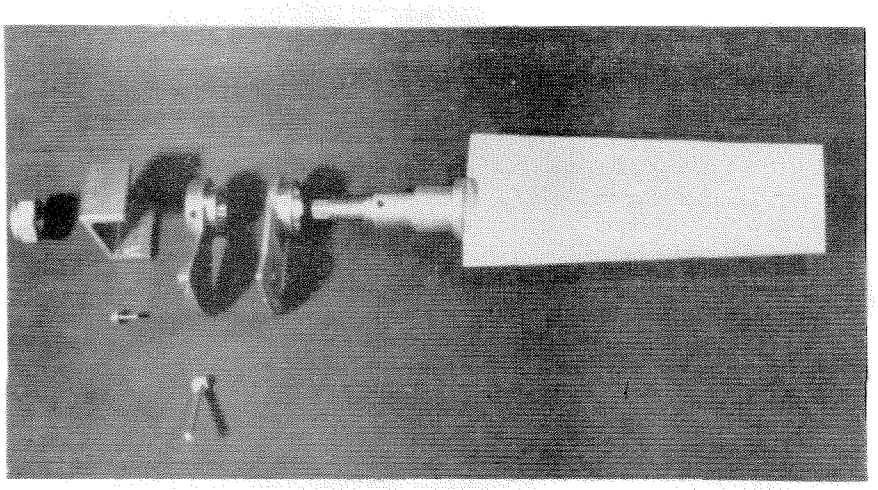

FIG. 11 DETAIL OF BLADE FASTENING MECHANISM

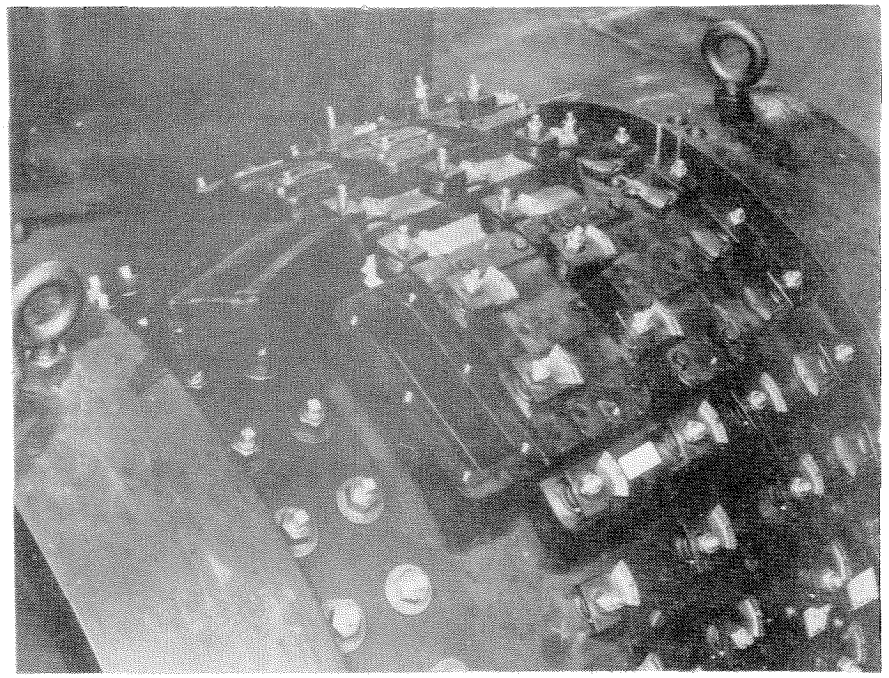

FIG. 12 DETAIL OF INSTRUMENT PORTS AND STATOR BLADE FASTENINGS

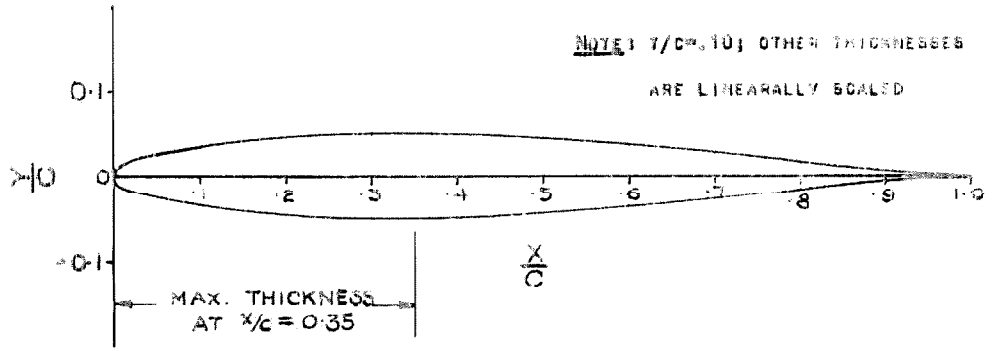

FIG. 13

BASIC AIRFOIL THICKNESS FOR COMPRESSOR BLADE DESIGN

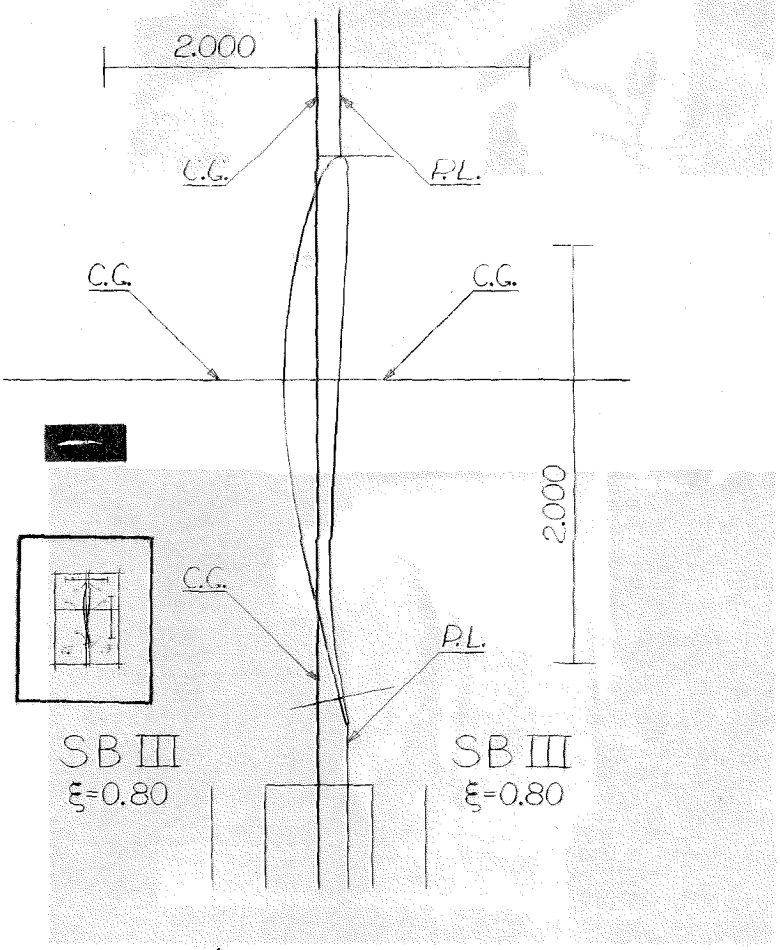

FIG. 14 MASTER BLADE DRAWING

THE PHOTOGRAPH SHOWS A 10X DRAWING OF A BLADE SECTION. A FULL SIZE PRINT OF THIS SECTION ON TEMPLET STOCK IS SHOWN IN THE UPPER LEFT CORNER AND AN ACTUALLY CROSSECTIONED BLADE IS SHOWN NEXT TO IT.

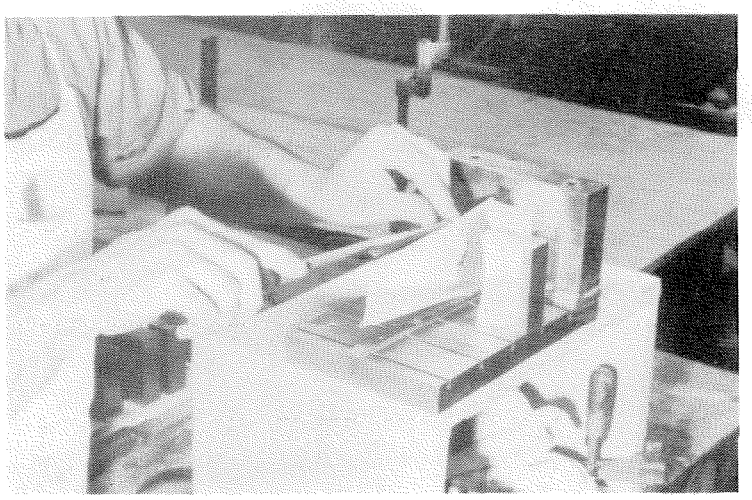

FIG. 15 BLADE BEING FINISHED.

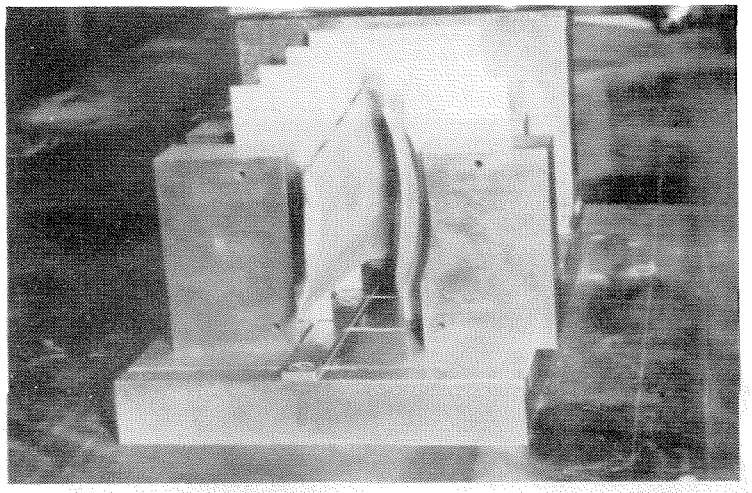

FIG. 16 BLADE BEING FINISHED WITH SECTION TEMPLATES.

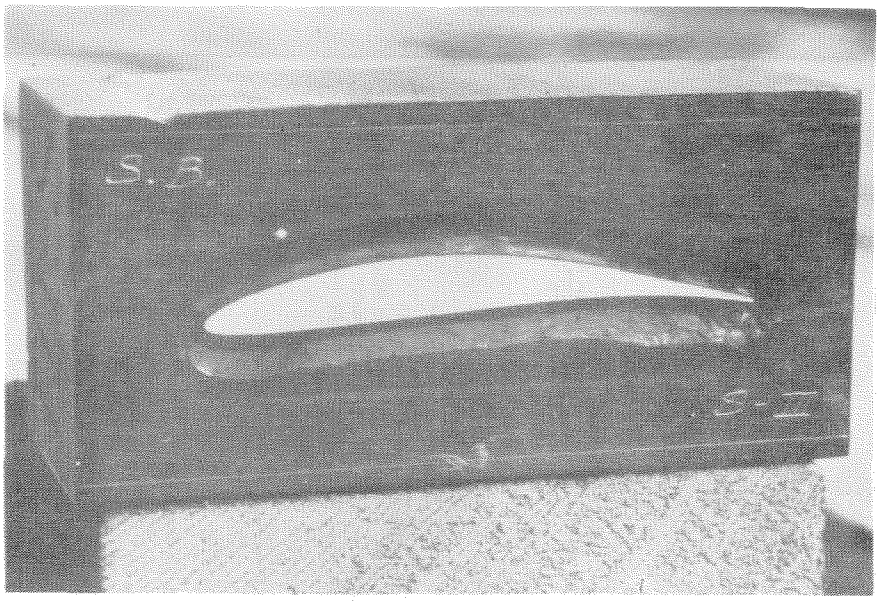

FIG. 17 A BLADE CROSS-SECTION

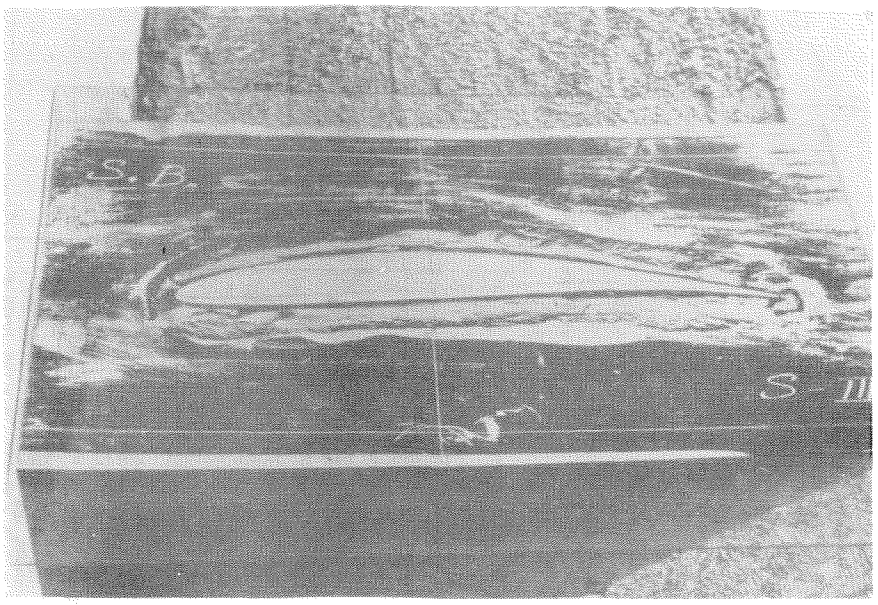

FIG. 18 SECTION COMPARISON TEST

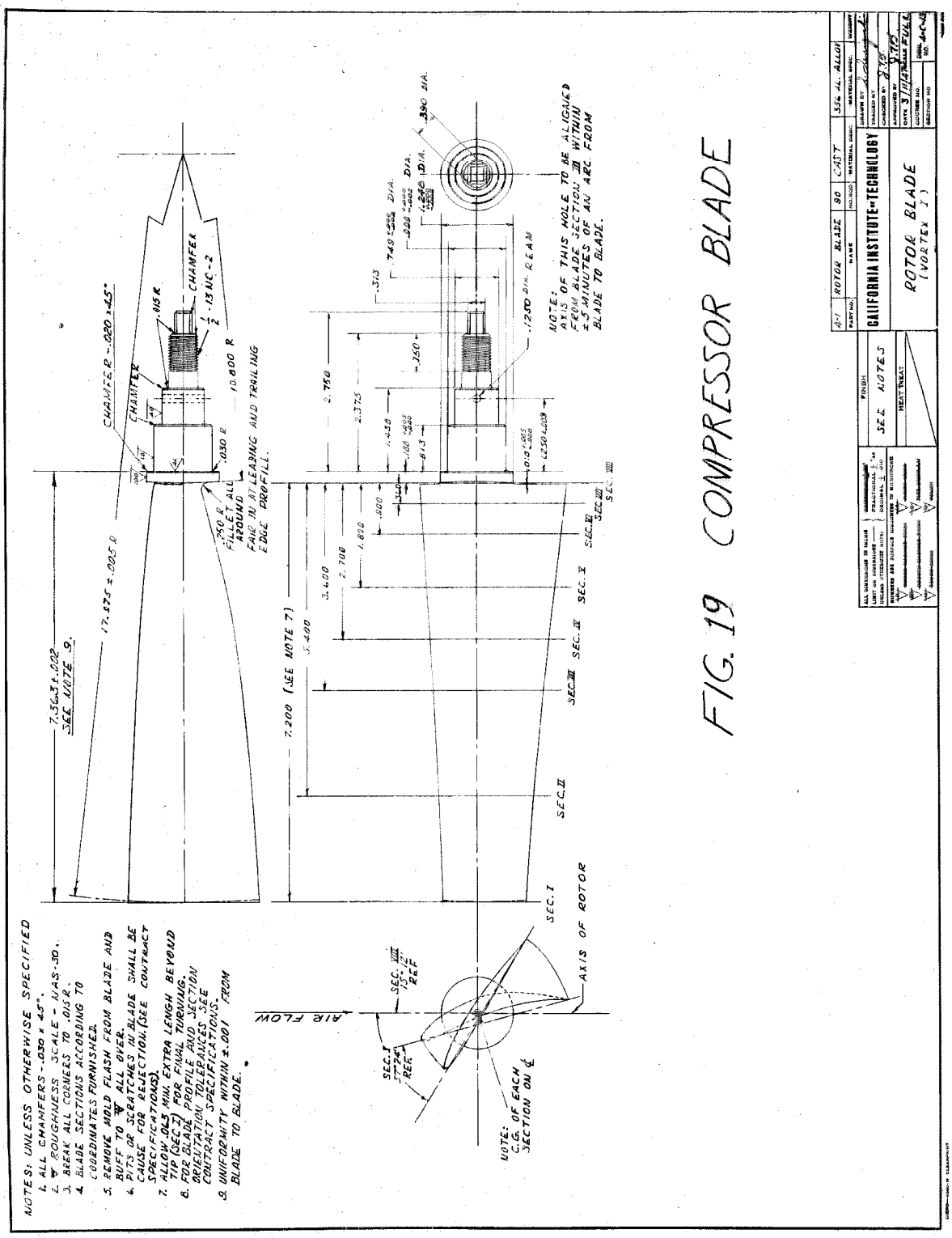

FIG. 19 COMPRESSOR BLADE

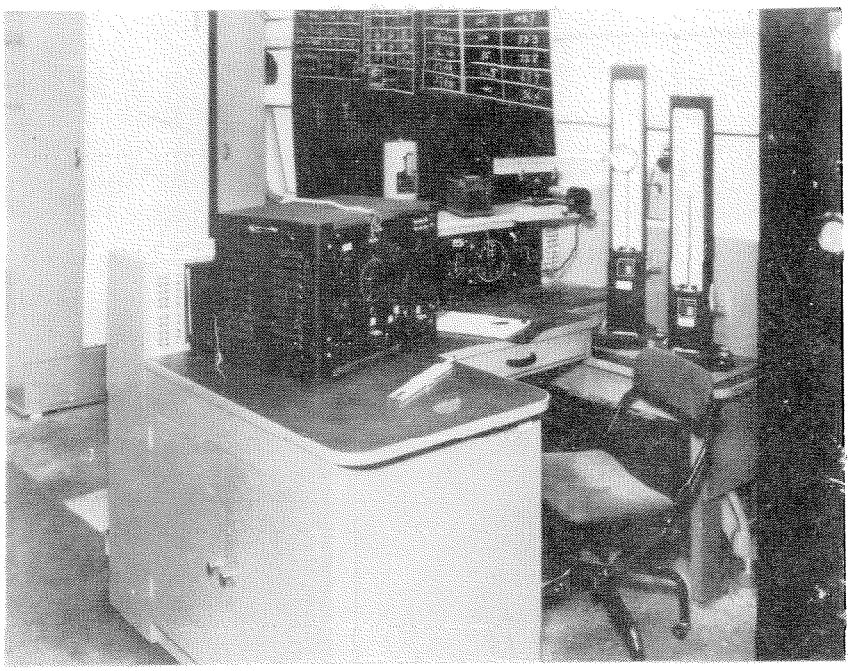

FIG. 20 THE OPERATING DESK

IN THE CENTER OF THE DESK THE TACHOMETER DIALS ARE SHOWN. THE CENTER DIAL IS FOR INSTANTANEOUS INDICATION. THE RIGHT HAND DIAL IS A CLOCK AND THE LEFT HAND DIAL A REVOLUTION COUNTER. THE TWO ARE COUPLED. ON THE DESK, TO THE RIGHT, TWO MERIAM MICRO MANOMETERS ARE SHOWN AND THE INSTRUMENT CASE TO THE LEFT CONTAINS THE BRIDGE FOR THE STATHAM PRESSURE GAGE. THE LEADS FROM THE GAGE ARE SEEN ON THE TOP OF THE BOX. IN THE BACKGROUND THE 20-TUBE MANOMETER IS SHOWN.

Fig. 21

DYNAMOMETER TORQUE CALIBRATION CURVE

FOR AXIAL-FLOW COMPRESSOR

C. I. T.

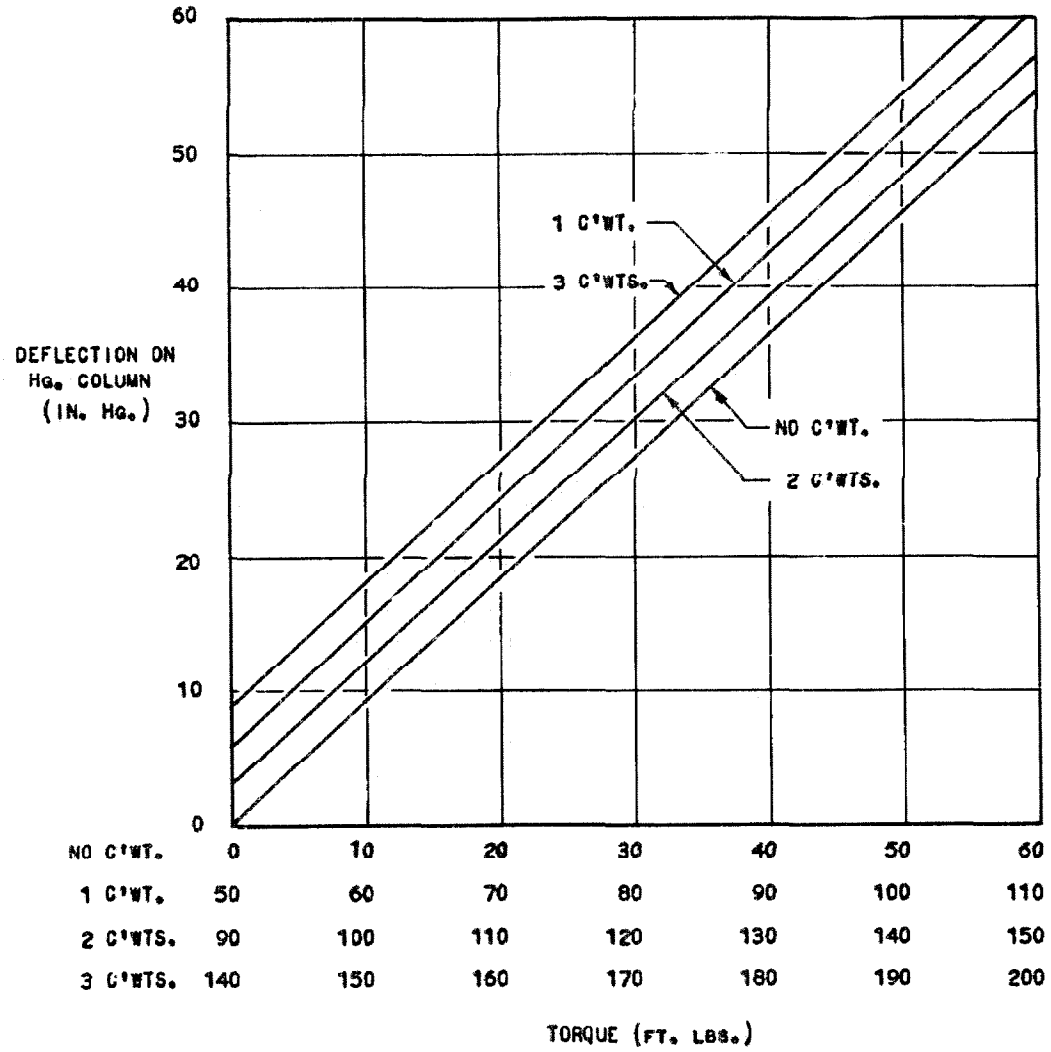

NO C'WT.	0	10	20	30	40	50	60
1 C'WT.	50	60	70	80	90	100	110
2 C'WTS.	90	100	110	120	130	140	150
3 C'WTS.	140	150	160	170	180	190	200

TORQUE (FT. LBS.)

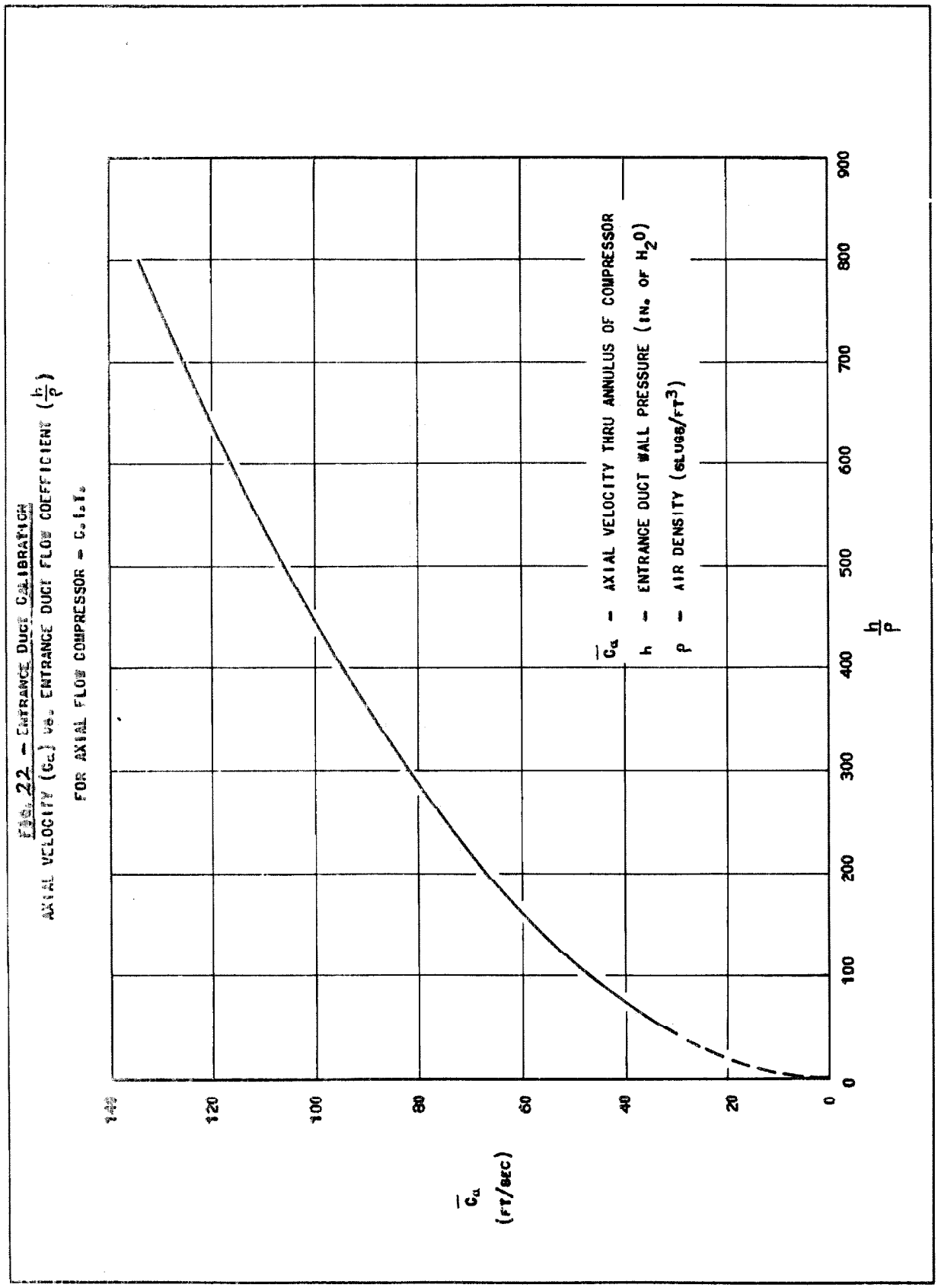

FIG. 22 - ENTRANCE DUCT CALIBRATION
AXIAL VELOCITY ($\bar{C}_a$) vs. ENTRANCE DUCT FLOW COEFFICIENT ($\frac{h}{\rho}$)
FOR AXIAL FLOW COMPRESSOR - C.I.T.

MEASURING PROBES

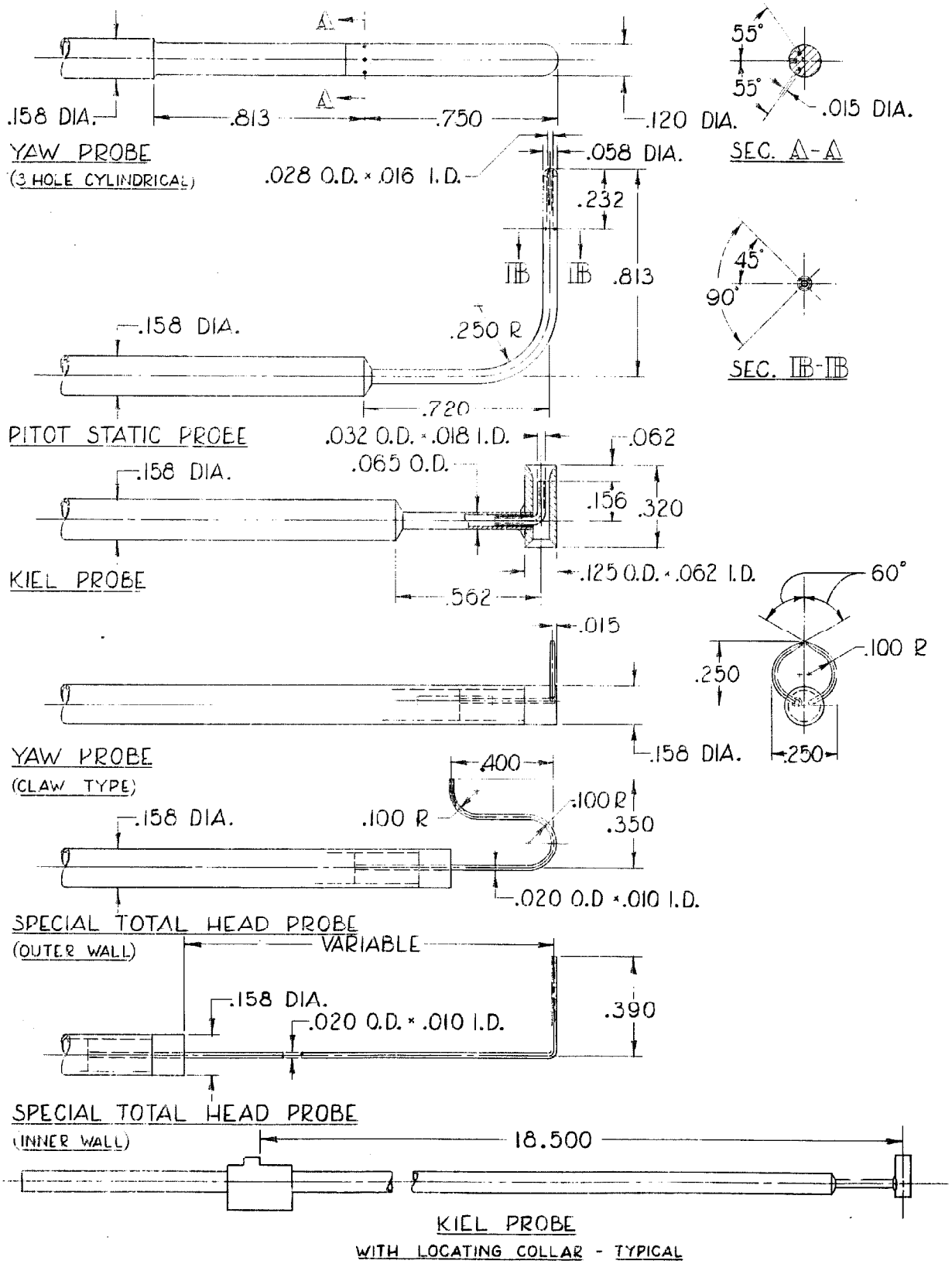

FIG. 23

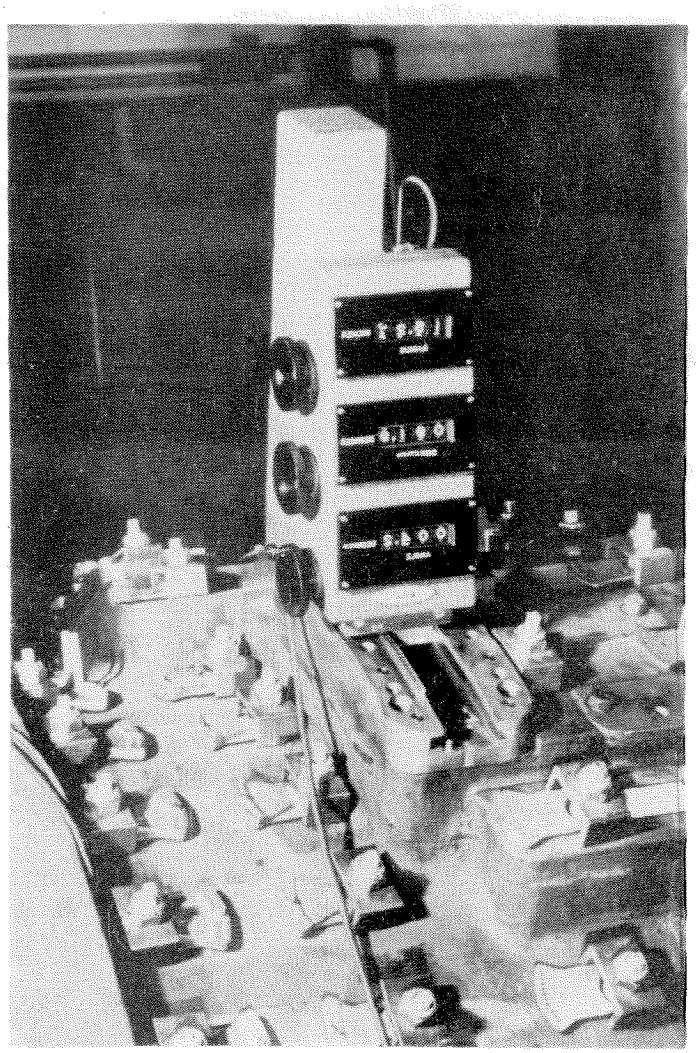

FIG. 24 INSTRUMENT CARRIAGE INSTALLED IN FORWARD PORT

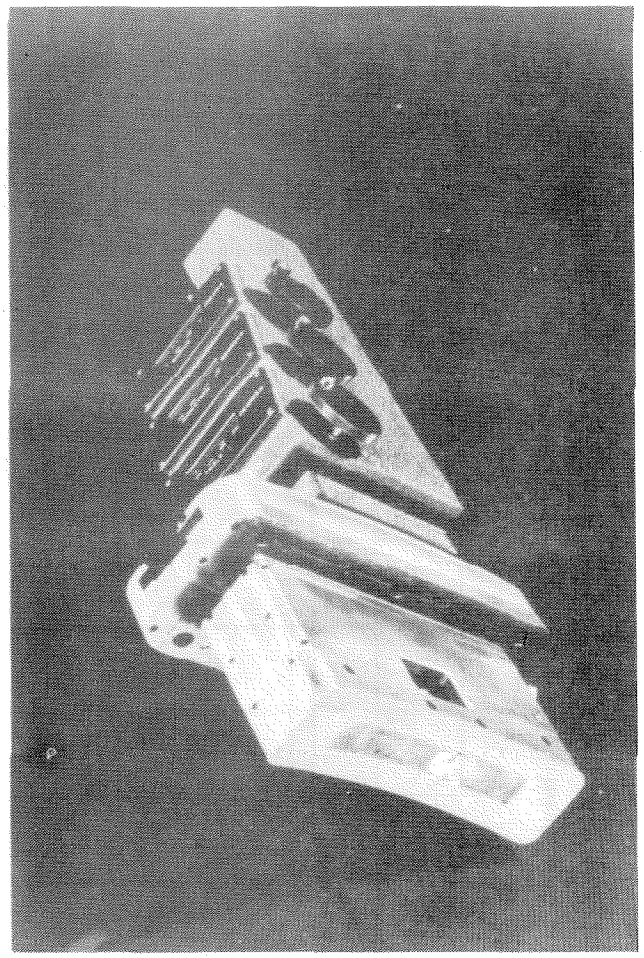

FIG. 25 INSTRUMENT CARRIAGE – BOTTOM VIEW

THE PHOTOGRAPH SHOWS HOW THE SLIDING TAPE FITS SMOOTHLY TO THE CURVED CONTOUR OF THE BASE. A TOTAL HEAD TUBE IS PROTUDING THROUGH THE TAPE.

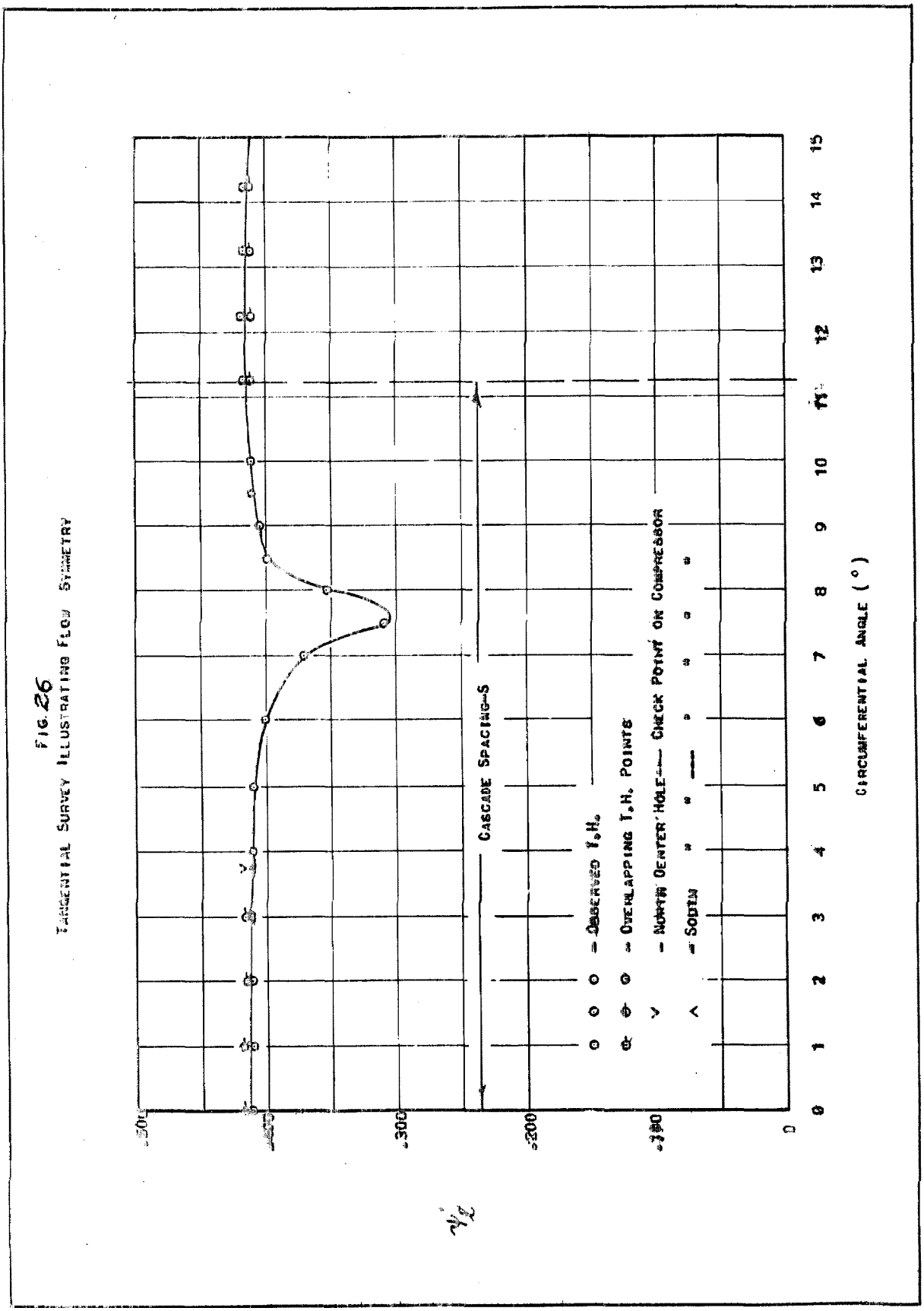

FIG. 26
TANGENTIAL SURVEY ILLUSTRATING FLOW SYMMETRY

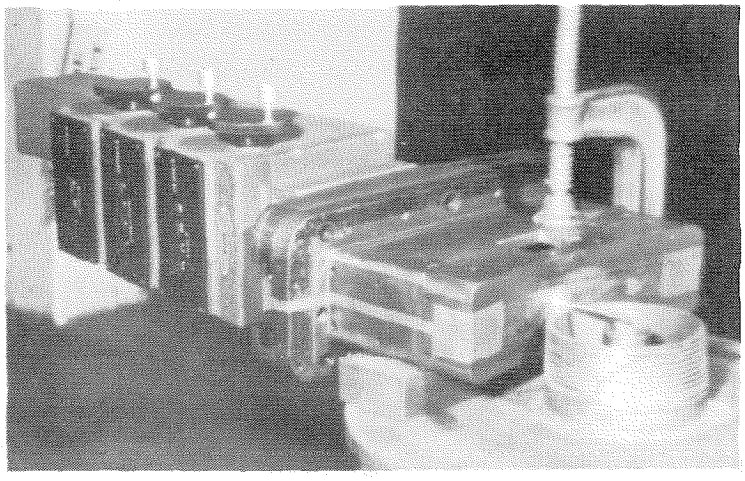

FIG. 27 INSTRUMENT CARRIAGE ON CALIBRATION STAND

THE SHOWN INSTRUMENT CARRIAGE IS SHOWN AS INSTALLED FOR CALIBRATING THE DIRECTION FINDING CLAW PROBE. THE CARRIAGE IS MOUNTED IN A PERFECTLY HORIZONTAL POSITION AND THE DIRECTION OF THE JET IS THEN DETERMINED. THE CARRIAGE IS THEN MOUNTED IN A SIMILAR POSITION BUT DISPLACED BY 180° AND THE DIRECTION READING IS REPEATED. THE MEAN OF THE TWO READINGS GIVEN THE ZERO DIRECTION OF THE PROBE.

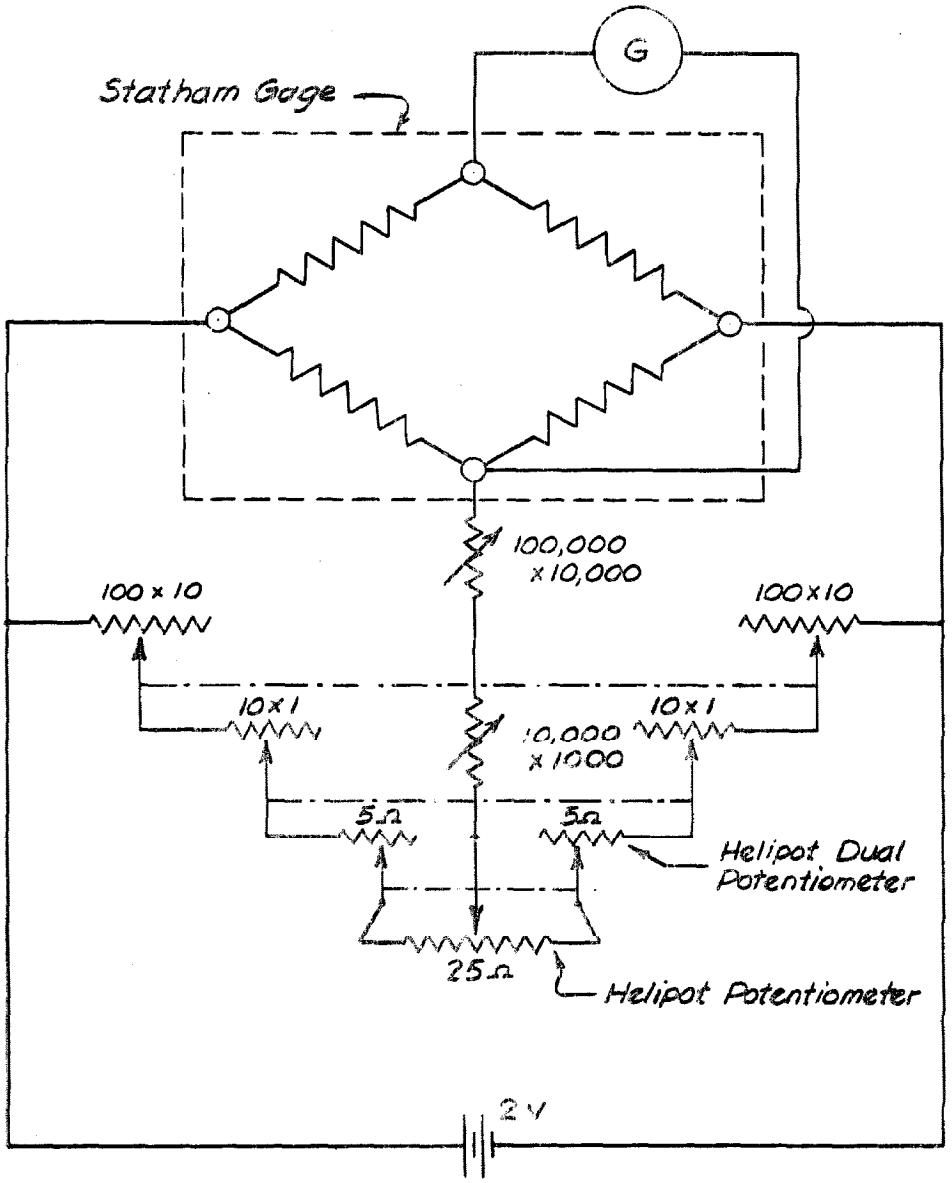

BRIDGE FOR USE WITH STATHAM PRESSURE GAGE

— CIRCUIT DIAGRAM —

(DESIGN BY C. THIELE)

NOTES

— · — · — · — MECHANICAL CONNECTION

100 x 10 = 100 OHM RHEOSTAT ADJUSTABLE IN 10 OHM STEPS. ALL DECADE RESISTORS WERE PROCURED FROM GENERAL RADIO CO.

FIG. 28

STATHAM GAGE CALIBRATION CURVE

FOR STATHAM GAGE PRESSURE TRANSMITTER

SERIAL No. 95 MODEL P5-0.20 - 250

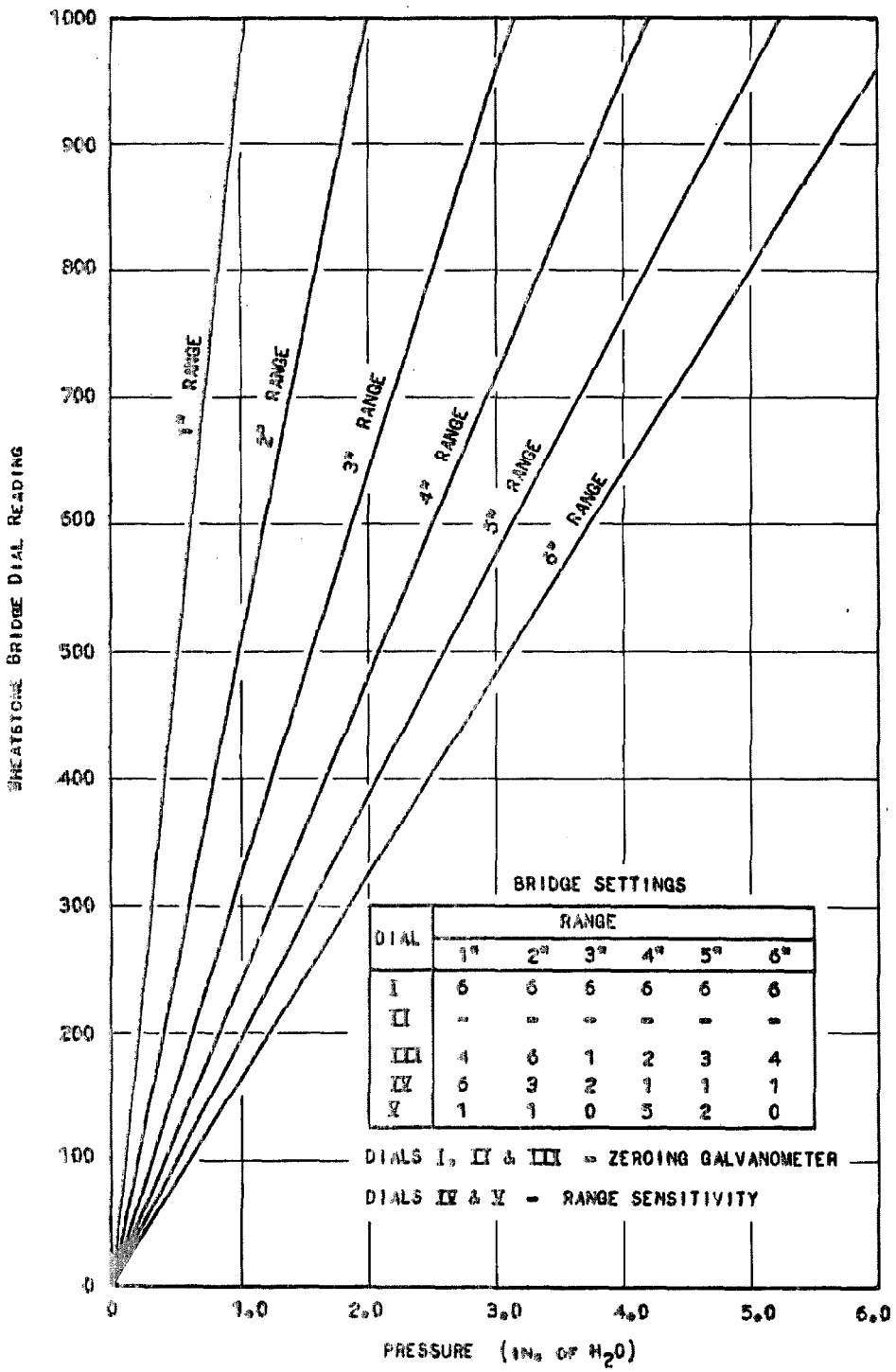

BRIDGE SETTINGS

DIAL	RANGE					
	1"	2"	3"	4"	5"	6"
I	6	6	6	6	6	6
II	"	"	"	"	"	"
III	4	6	1	2	3	4
IV	6	3	2	1	1	1
V	1	1	0	5	2	0

DIALS I, II & III = ZEROING GALVANOMETER

DIALS IV & V = RANGE SENSITIVITY

FIG. 29

Radius	Blade Type $\lambda_1 = \frac{\alpha}{\xi^2}$	Blade Type $\lambda_1 = \frac{\alpha}{\xi}$	Blade Type $\lambda_1 = \alpha$	Blade Type $\lambda_1 = \alpha\xi$	Blade Type $\lambda_1 = \alpha\xi^2$
$\xi = 1.0$	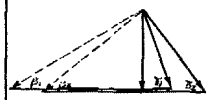	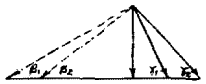	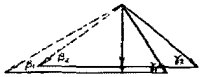	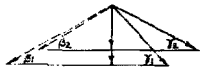	
$\xi = 0.8$	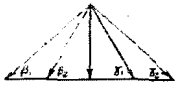		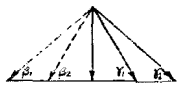		
$\xi = 0.6$			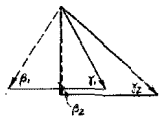	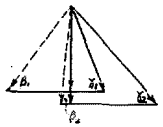	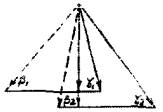

NOTE: λ_1 AT $\xi = 0.8$ TAKEN EQUAL FOR ALL BLADE TYPES EXCEPT $\alpha\xi^2$

ϕ_1 = AXIAL VELOCITY ENTERING ROTOR
ϕ_2 = AXIAL VELOCITY LEAVING ROTOR
λ_1 = TANGENTIAL VELOCITY ENTERING ROTOR
λ_2 = TANGENTIAL VELOCITY LEAVING ROTOR

β_1 = ROTOR BLADE ENTRANCE ANGLE
β_2 = ROTOR BLADE EXIT ANGLE
γ_1 = STATOR BLADE EXIT ANGLE
γ_2 = STATOR BLADE ENTRANCE ANGLE

$\Phi = 0.45$
$\psi = 0.40$

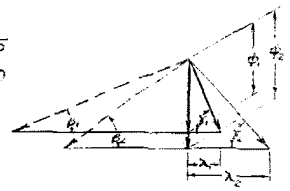

VELOCITY DIAGRAMS FOR VARIOUS BLADE TYPES OF THE FORM $\lambda_1 = \alpha\xi^n$

FIG 30 a

RADIUS	POSITION OF 50 PERCENT REACTION POINT				
	$\xi_2 = 0.45$	$\xi_3 = 0.50$	$\xi_4 = 0.70$	$\xi_5 = 0.80$	$\xi_6 = 0.90$
$\xi = 1.0$	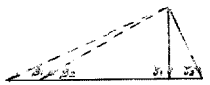		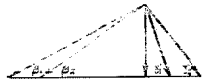	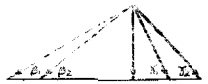	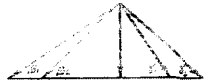
$\xi = 0.8$	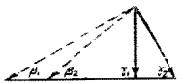	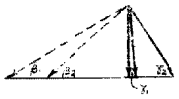	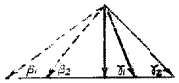		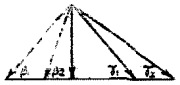
$\xi = 0.6$	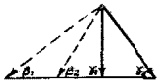	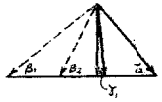	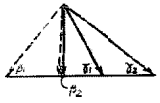		

ϕ_1 = AXIAL VELOCITY ENTERING ROTOR
ϕ_2 = AXIAL VELOCITY LEAVING ROTOR
λ_1 = TANGENTIAL VELOCITY ENTERING ROTOR
λ_2 = TANGENTIAL VELOCITY LEAVING ROTOR

β_1 = ROTOR BLADE ENTRANCE ANGLE
β_2 = ROTOR BLADE EXIT ANGLE
γ_1 = STATOR BLADE EXIT ANGLE
γ_2 = STATOR BLADE ENTRANCE ANGLE

$\bar{\Phi} = 0.45$
$\psi = 0.40$

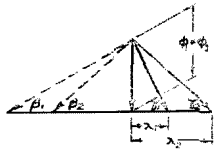

VELOCITY DIAGRAMS OF FREE VORTEX BLADES WITH VARYING POSITION OF THE 50 PERCENT REACTION POINT

FIG. 30 b

RADIUS	POSITION OF 50 PERCENT REACTION POINT				
	$\xi_{50} = 0.45$ ($\alpha = 0$)	$\xi_{50} = 0.55$ ($\alpha = 0.10$)	$\xi_{50} = 0.67$ ($\alpha = 0.20$)	$\xi_{50} = 0.82$ ($\alpha = 0.344$)	$\xi_{50} = 0.90$ ($\alpha = 0.40$)
$\xi = 1.0$			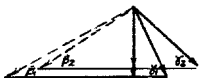	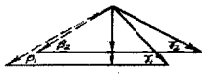	
$\xi = 0.8$		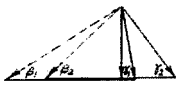	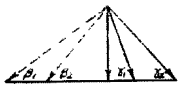		
$\xi = 0.6$	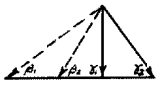	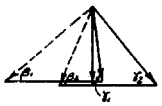	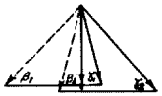	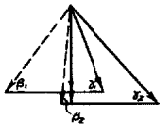	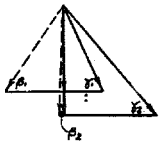

ϕ_1 = AXIAL VELOCITY ENTERING ROTOR
ϕ_2 = AXIAL VELOCITY LEAVING ROTOR
λ_1 = TANGENTIAL VELOCITY ENTERING ROTOR
λ_2 = TANGENTIAL VELOCITY LEAVING ROTOR

β_1 = ROTOR BLADE ENTRANCE ANGLE
β_2 = ROTOR BLADE EXIT ANGLE
γ_1 = STATOR BLADE EXIT ANGLE
γ_2 = STATOR BLADE ENTRANCE ANGLE

$\Phi = 0.45$
$\Psi = 0.40$

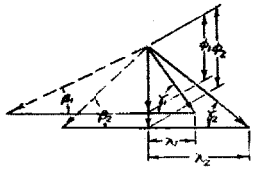

VELOCITY DIAGRAMS OF SOLID BODY BLADES WITH VARYING POSITION OF THE 50 PERCENT REACTION POINT

FIG. 30c

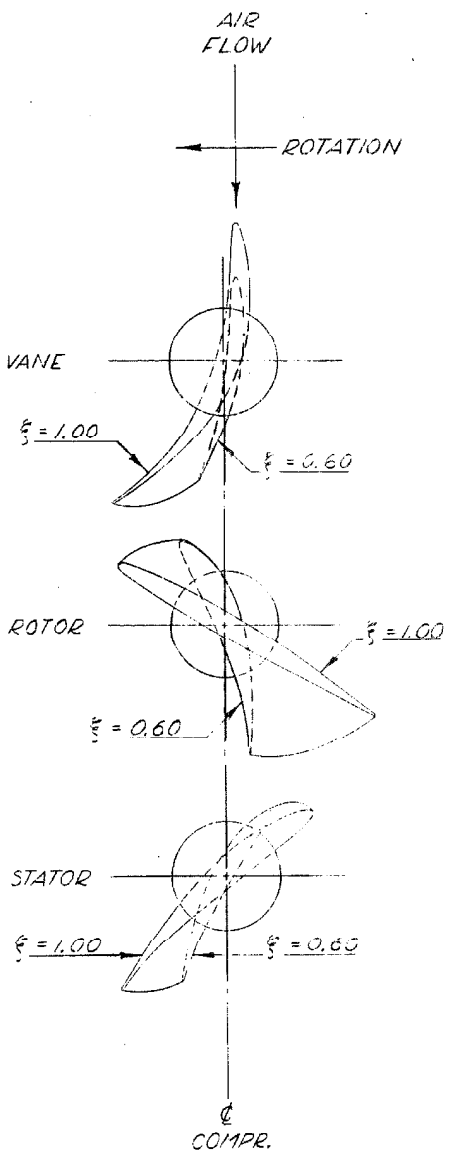

SOLID BODY BLADING

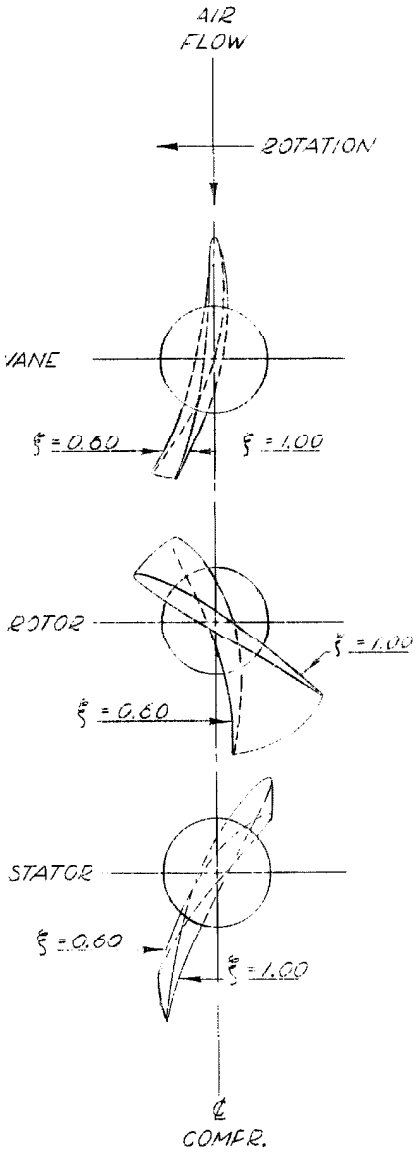

FREE VORTEX BLADING

COMPRESSOR BLADING

NOTE:
THE BLADE TYPES SHOWN HAVE BEEN CONSTRUCTED

FIG. 31

SOLID BODY BLADING
FLOW THROUGH ENTRANCE VANES
CHANGE OF AXIAL VELOCITY ALONG A RADIUS

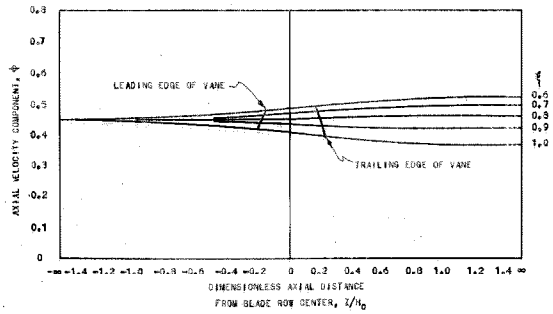

H_0 = CHANNEL HEIGHT

FIG. 32

SOLID BODY BLADING
FLOW THROUGH ENTRANCE VANES
RADIAL VELOCITY COMPONENTS ALONG A RADIUS

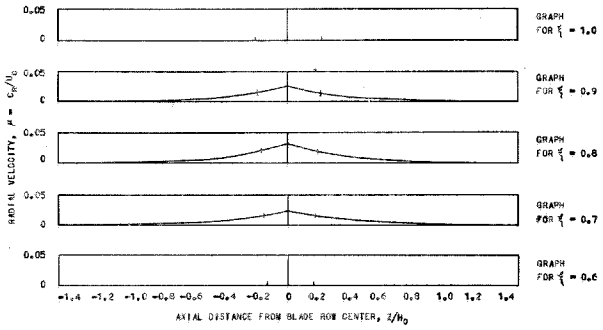

NOTE: H_0 = CHANNEL HEIGHT

NOTE: SMALL VERTICAL BARS INDICATE LOCATION OF VANE EDGE

FIG. 33

SOLID BODY BLADING
FLOW THROUGH ENTRANCE VANES
CHANGE OF CIRCUMFERENTIAL VELOCITY COMPONENT ALONG A RADIUS

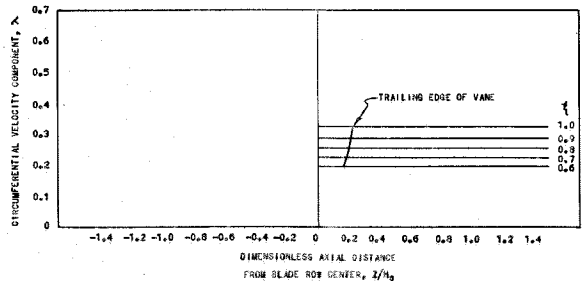

H_0 = CHANNEL HEIGHT

FIG. 34

SOLID BODY BLADING
FLOW THROUGH FIRST ROTOR
CHANGE OF AXIAL VELOCITY ALONG A RADIUS

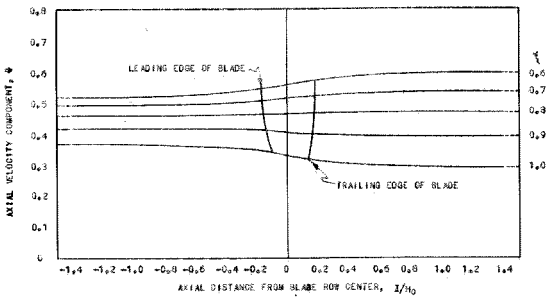

NOTE: H_0 = CHANNEL HEIGHT

FIG. 35

SOLID BODY BLADING
FLOW THROUGH FIRST ROTOR
RADIAL VELOCITY COMPONENTS ALONG A RADIUS

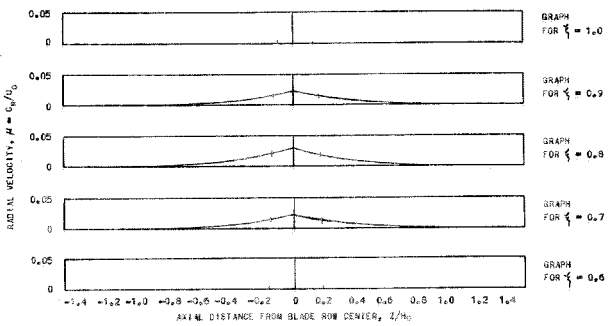

NOTE: H_0 = CHANNEL HEIGHT

NOTE: SMALL VERTICAL BARS INDICATE LOCATION OF VANE EDGE

FIG. 36

SOLID BODY BLADING
FLOW THROUGH THE FIRST ROTOR
CHANGE OF CIRCUMFERENTIAL VELOCITY COMPONENT ALONG A RADIUS

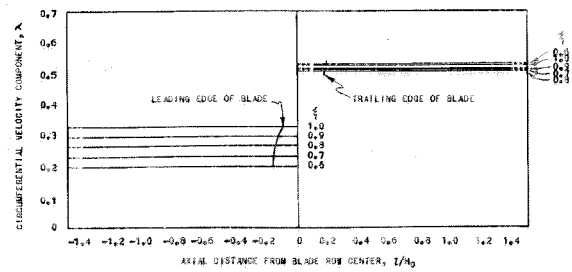

NOTE: H_0 = CHANNEL HEIGHT

FIG. 37

SOLID BODY BLADING
FLOW THROUGH ENTRANCE VANES
FLOW DIRECTION ALONG A RADIUS

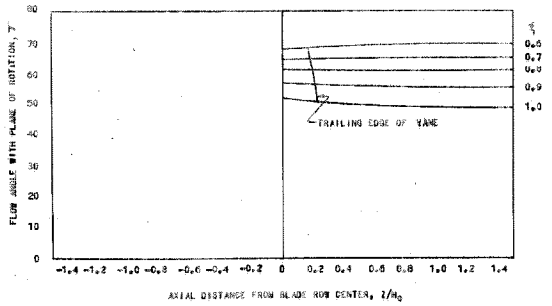

NOTE: H_0 = CHANNEL HEIGHT

FIG. 38

SOLID BODY BLADING - ROTOR
RELATIVE FLOW ANGLE (β)
FOR VARIOUS RADII ($\bar{r}$)

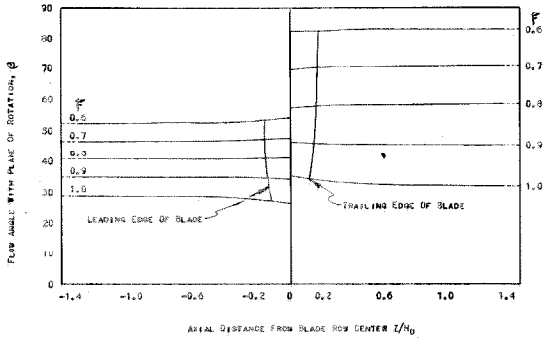

NOTE: H_0 = CHANNEL HEIGHT

FIG. 39

SOLID BODY BLADING
FLOW THROUGH THE FIRST STATOR
FLOW ANGLE (β) FOR VARIOUS RADII ($\bar{r}$)

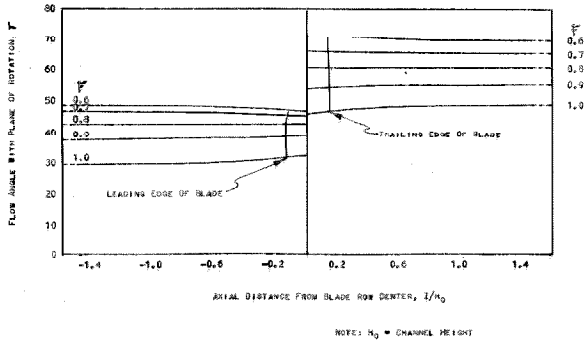

NOTE: H_0 = CHANNEL HEIGHT

FIG. 40

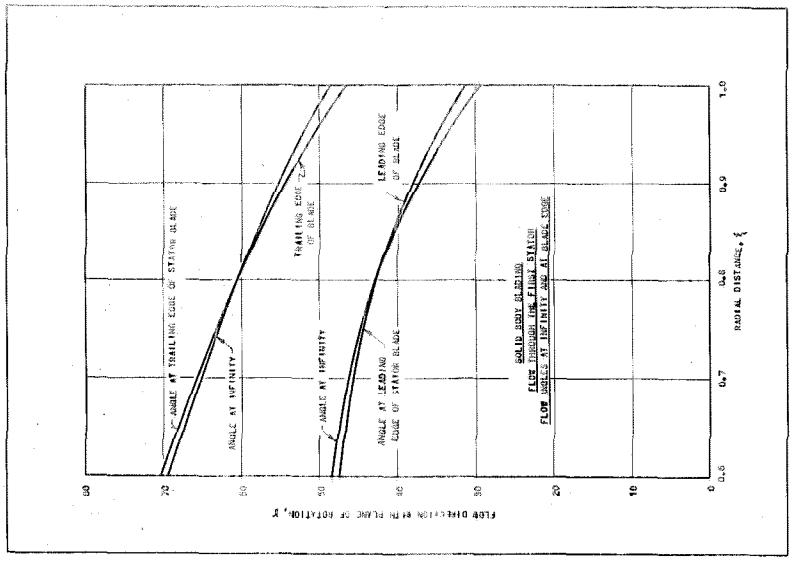

FIG. 43

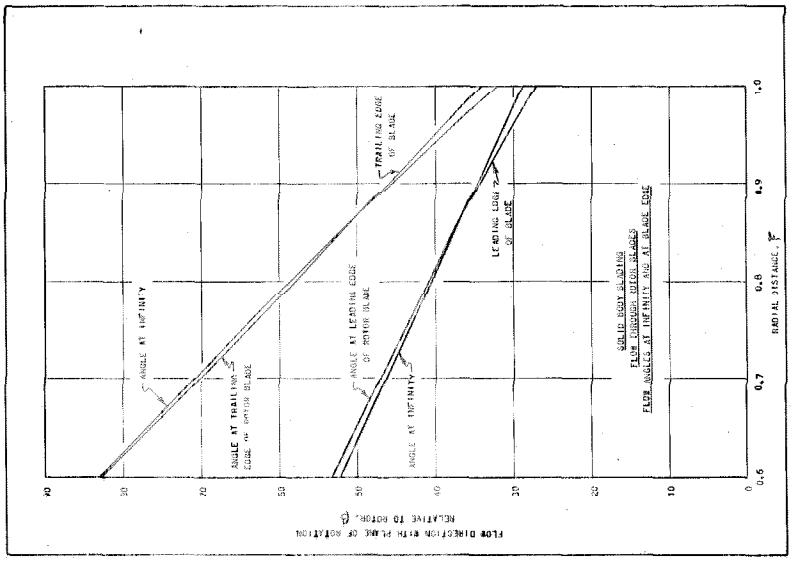

FIG. 42

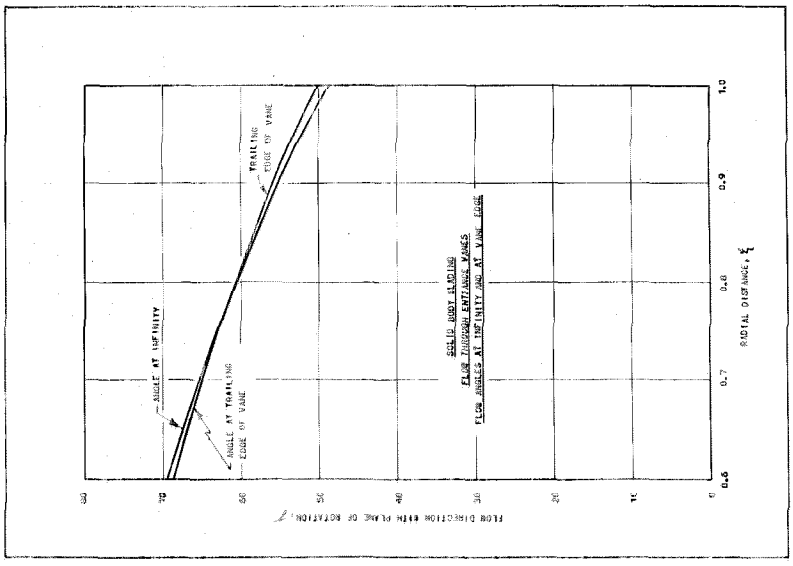

FIG. 41

SOLID BODY BLADING
FLOW THROUGH ENTRANCE VANES
STREAMLINE PICTURE OF THE FLOW

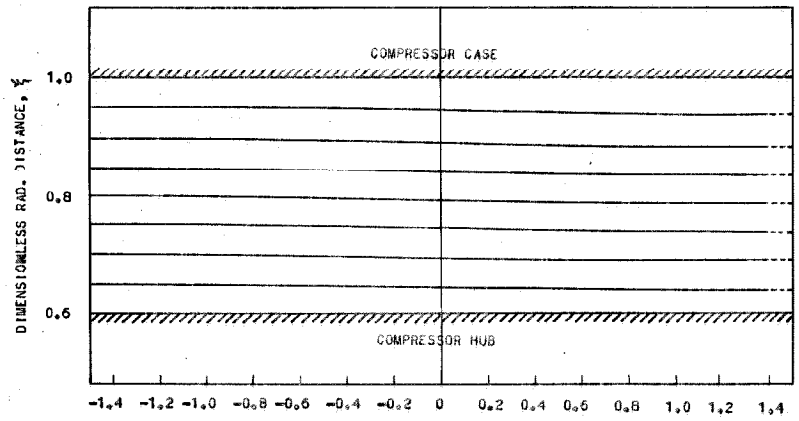

H_0 = CHANNEL HEIGHT

FIG. 44

SOLID BODY BLADING
FLOW THROUGH FIRST ROTOR
STREAMLINE PICTURE OF THE FLOW

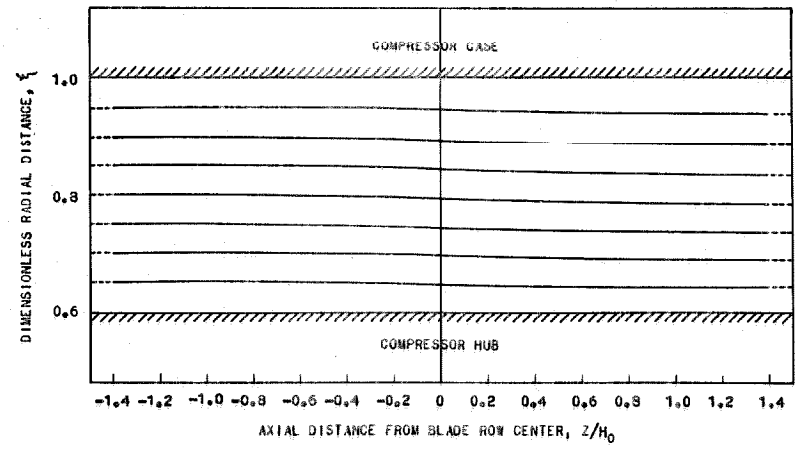

NOTE: H_0 = CHANNEL HEIGHT

FIG. 45

SOLID BODY BLADING
FLOW THROUGH ENTRANCE VANES
DETERMINATION OF STREAM TUBE RADIUS

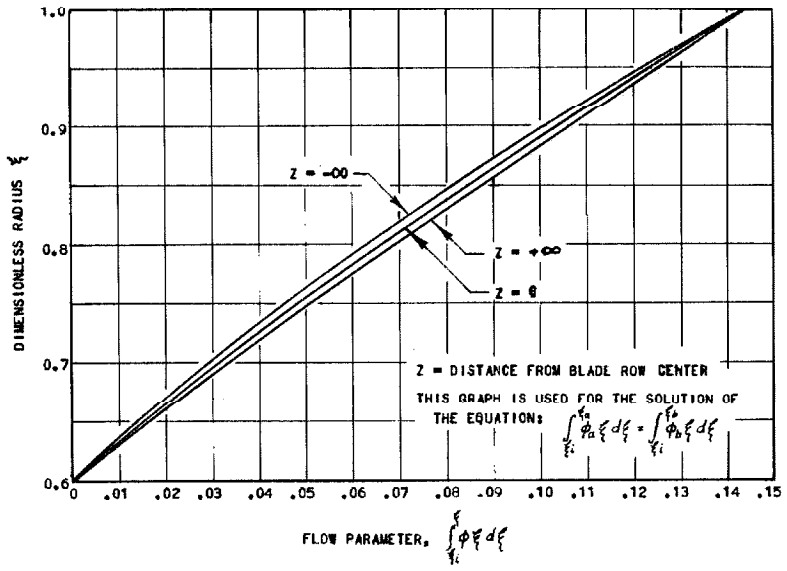

FIG. 46a

SOLID BODY BLADING
FLOW THROUGH ROTOR OR STATOR BLADES
DETERMINATION OF STREAM TUBE RADIUS

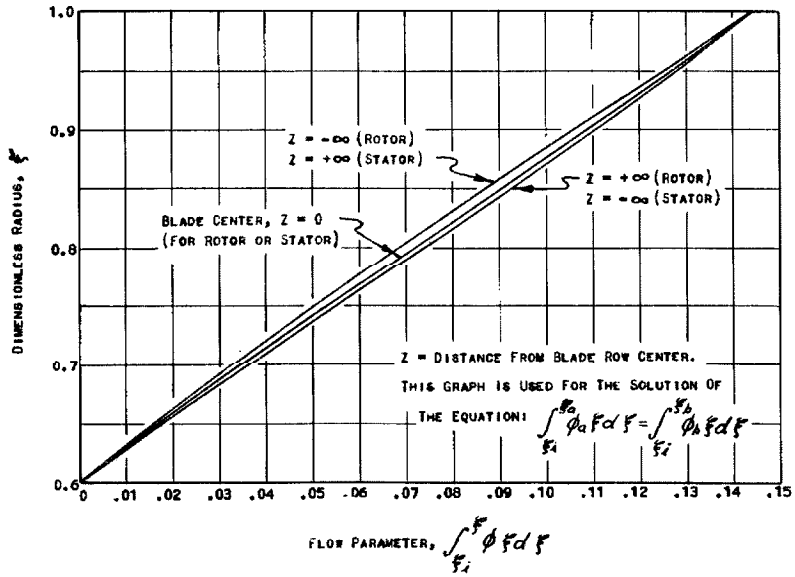

FIG. 46b

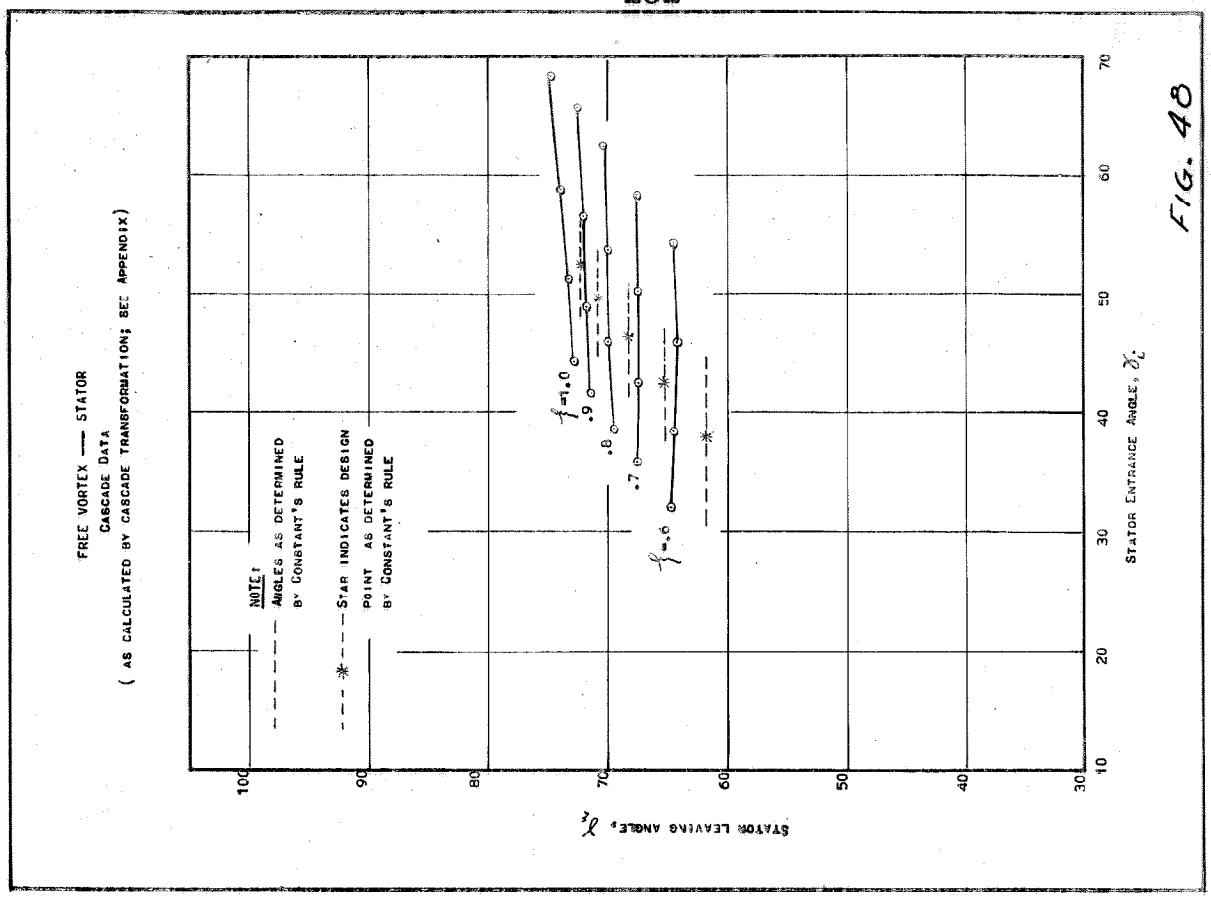
FREE VORTEX — STATOR
CASCADE DATA
(AS CALCULATED BY CASCADE TRANSFORMATION; SEE APPENDIX)
NOTE:
ANGLES AS DETERMINED BY CONSTANT'S RULE
STAR INDICATES DESIGN POINT AS DETERMINED BY CONSTANT'S RULE
STATOR LEAVING ANGLE, γ_2
STATOR ENTRANCE ANGLE, γ_1
$i=1.0$
.9
.8
.7
$i=.6$

FIG. 48

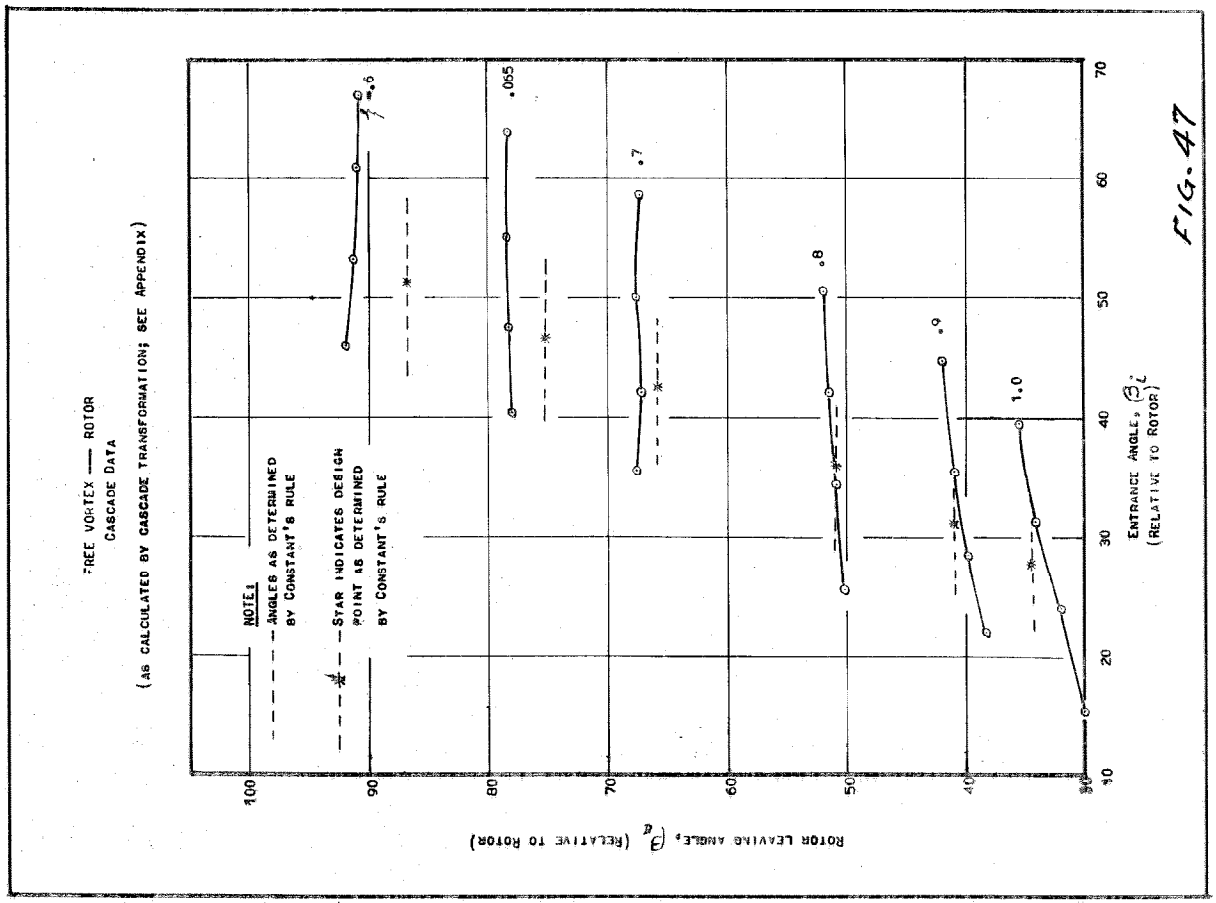
FREE VORTEX — ROTOR
CASCADE DATA
(AS CALCULATED BY CASCADE TRANSFORMATION; SEE APPENDIX)
NOTE:
ANGLES AS DETERMINED BY CONSTANT'S RULE
STAR INDICATES DESIGN POINT AS DETERMINED BY CONSTANT'S RULE
ROTOR LEAVING ANGLE, β_2 (RELATIVE TO ROTOR)
ENTRANCE ANGLE, β_1 (RELATIVE TO ROTOR)
$i=.6$
.065
.7
.8
.9
1.0

FIG. 47

SOLID BODY BLADING - ROTOR

CASCADE DATA

(AS CALCULATED BY CASCADE TRANSFORMATION)

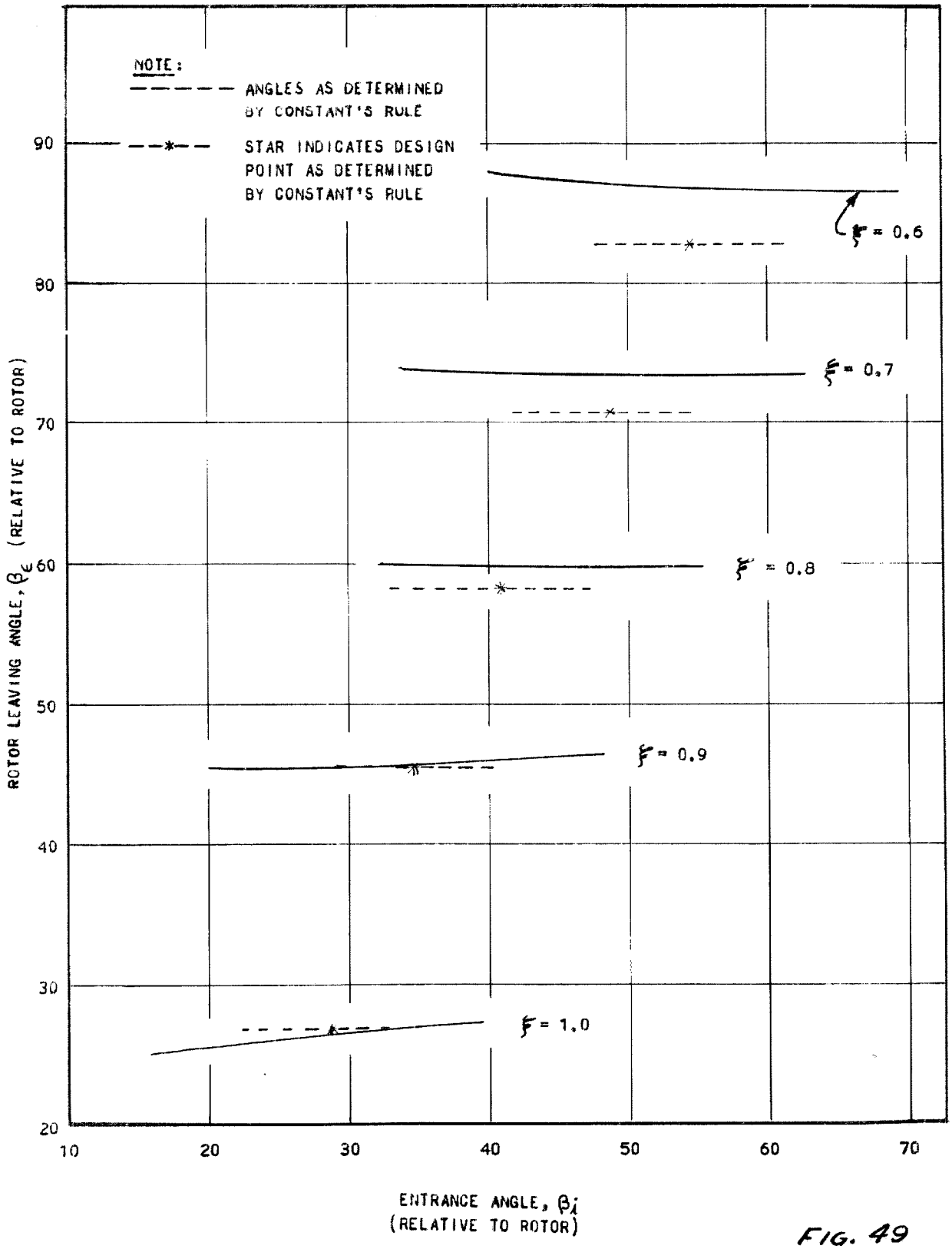

FIG. 49

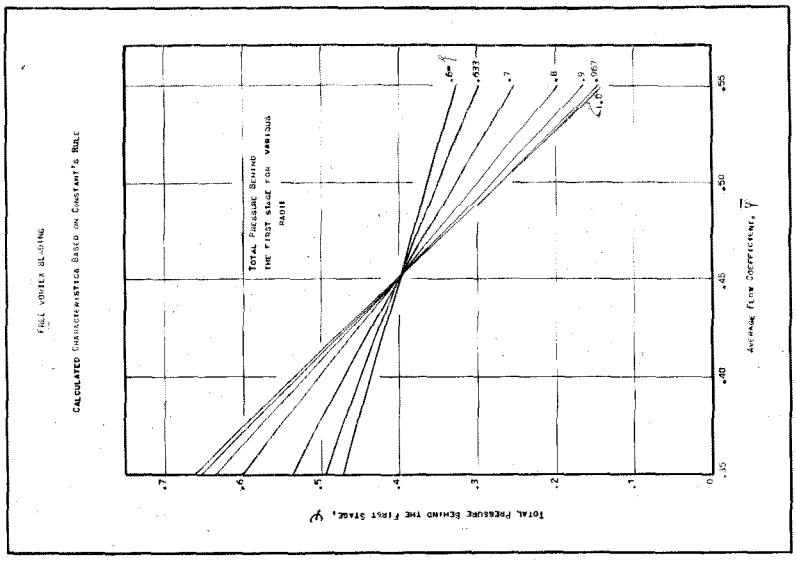

FIG. 52

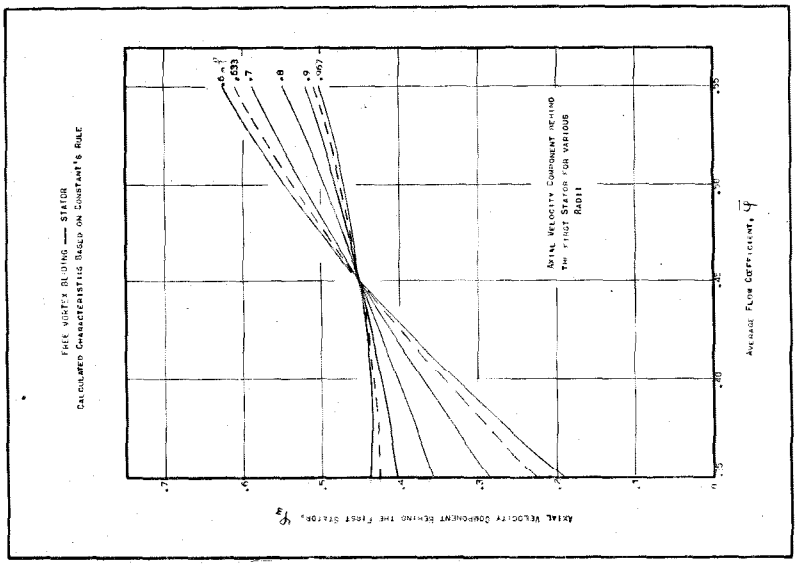

FIG. 51

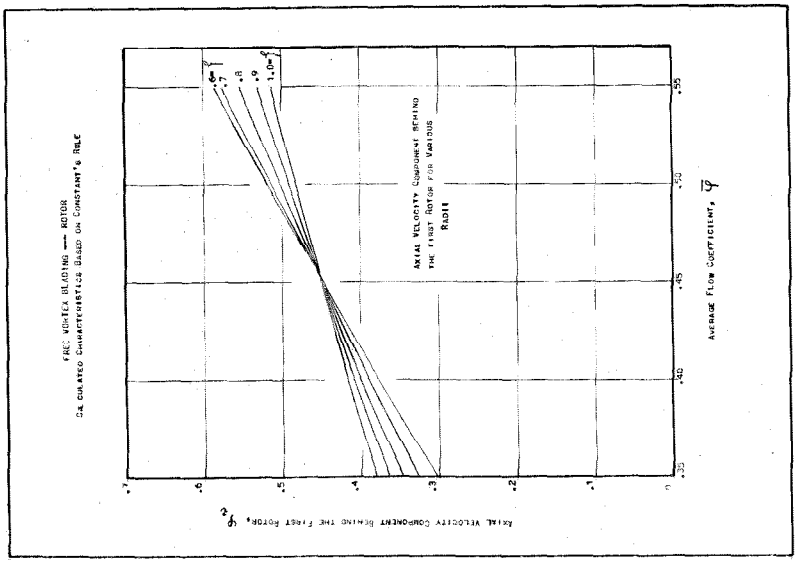

FIG. 50

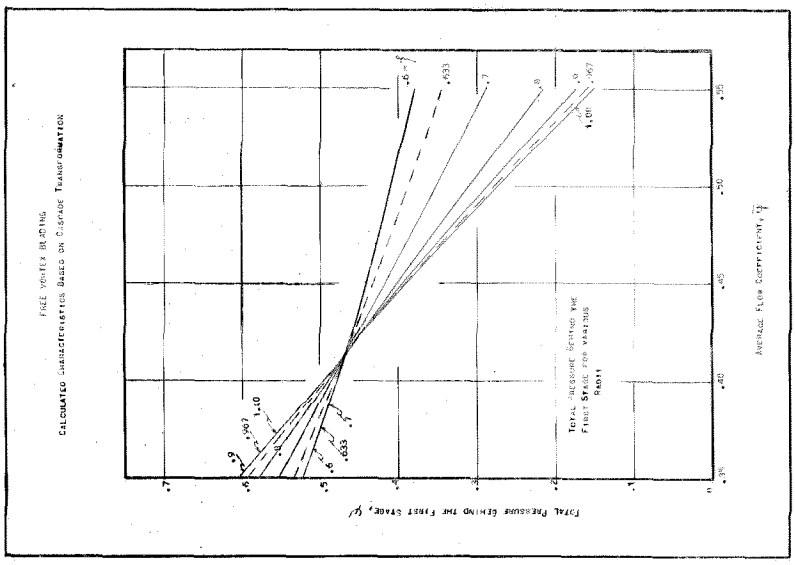

FIG. 55

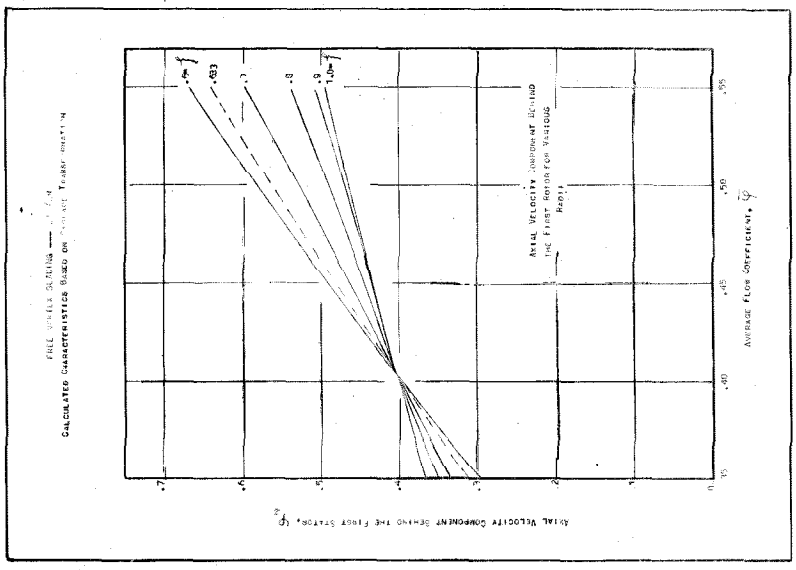

FIG. 54

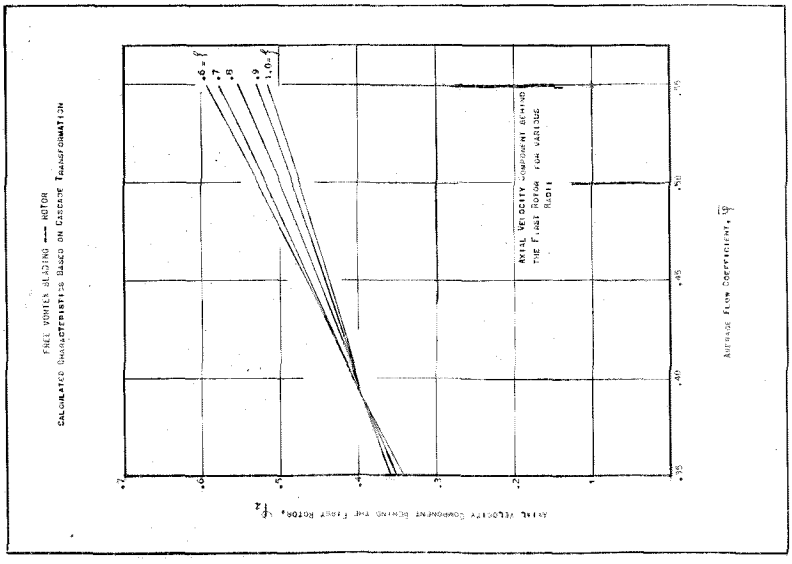

FIG. 53

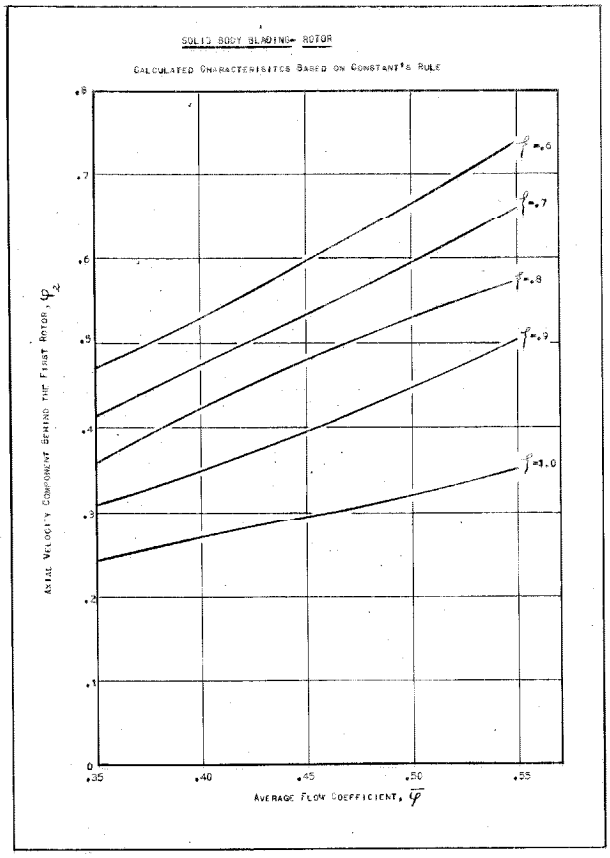

FIG. 56

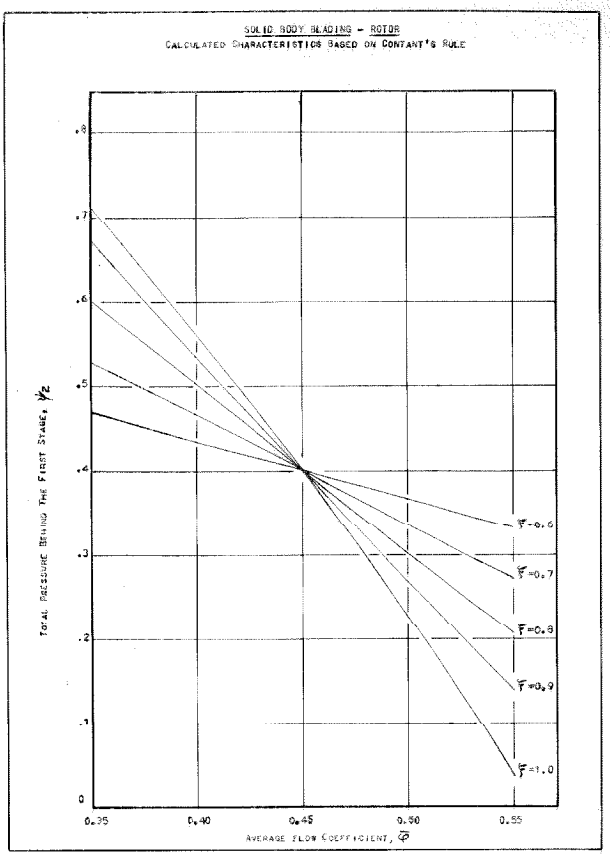

FIG. 57

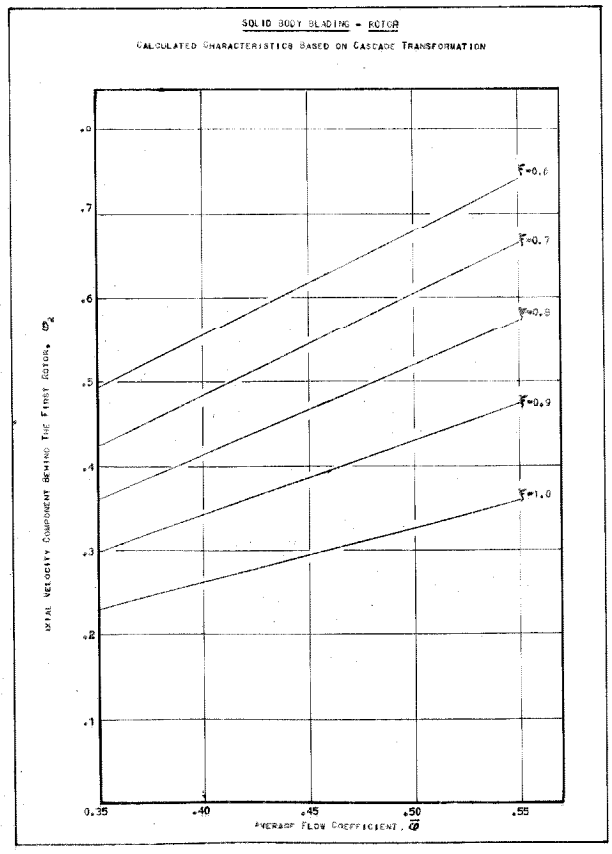

FIG. 58

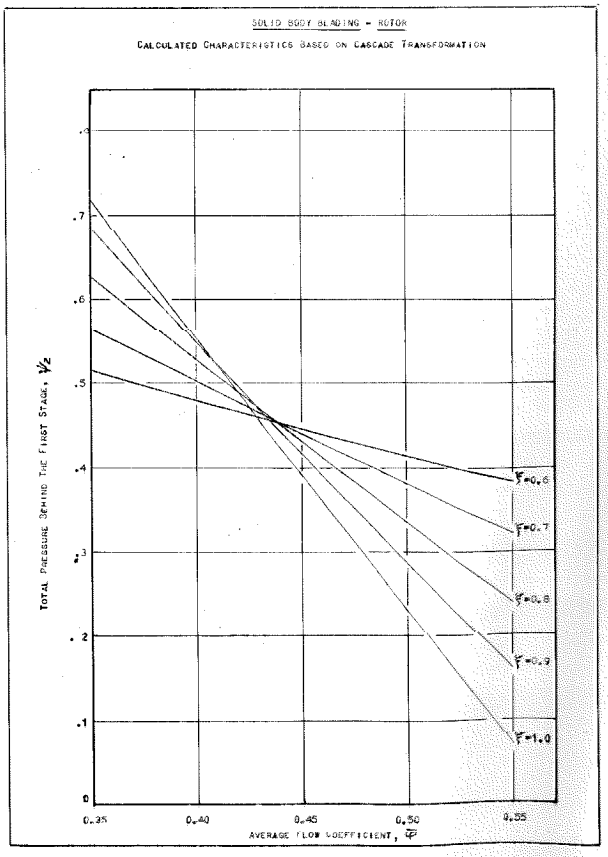

FIG. 59

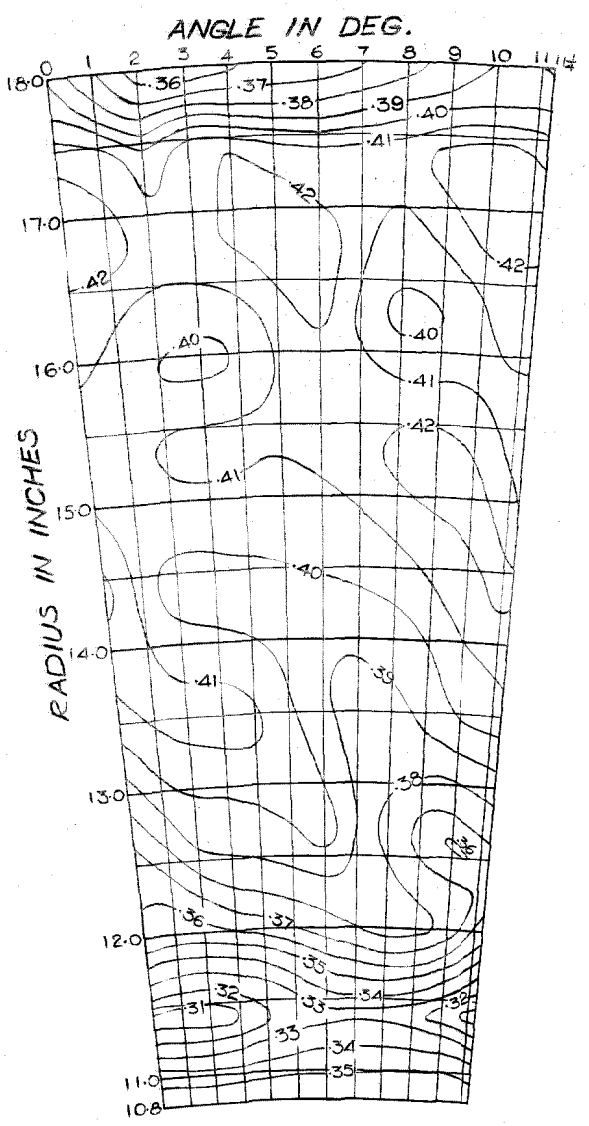

A) DOWNSTREAM OF 1ST ROTOR

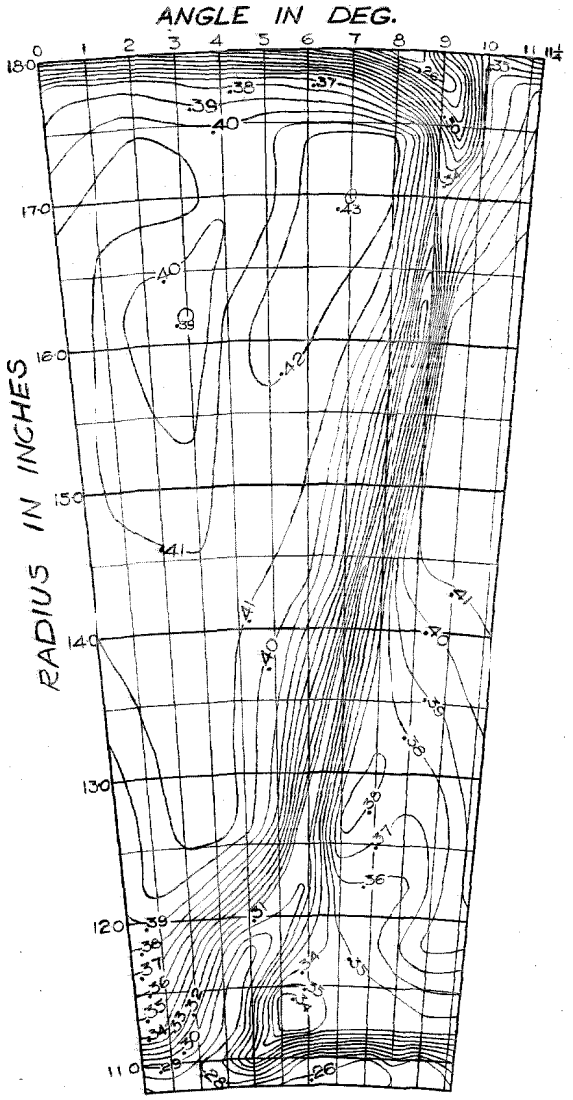

B) DOWNSTREAM OF 1ST STATOR

NOTE:

A) CONTOURS ARE LINES OF $\psi' = const.$ where

$$\psi' = \frac{P_t - P_s}{\frac{1}{2}\rho u_o^2}$$

B) THE ANGLE 11¼° IS EQUIVALENT TO ONE STATOR BLADE PITCH (32 BLADES). PATTERNS REPEAT AROUND COMPLETE ANNULUS.

FIG. 60 TOTAL PRESSURE CONTOUR PLOTS

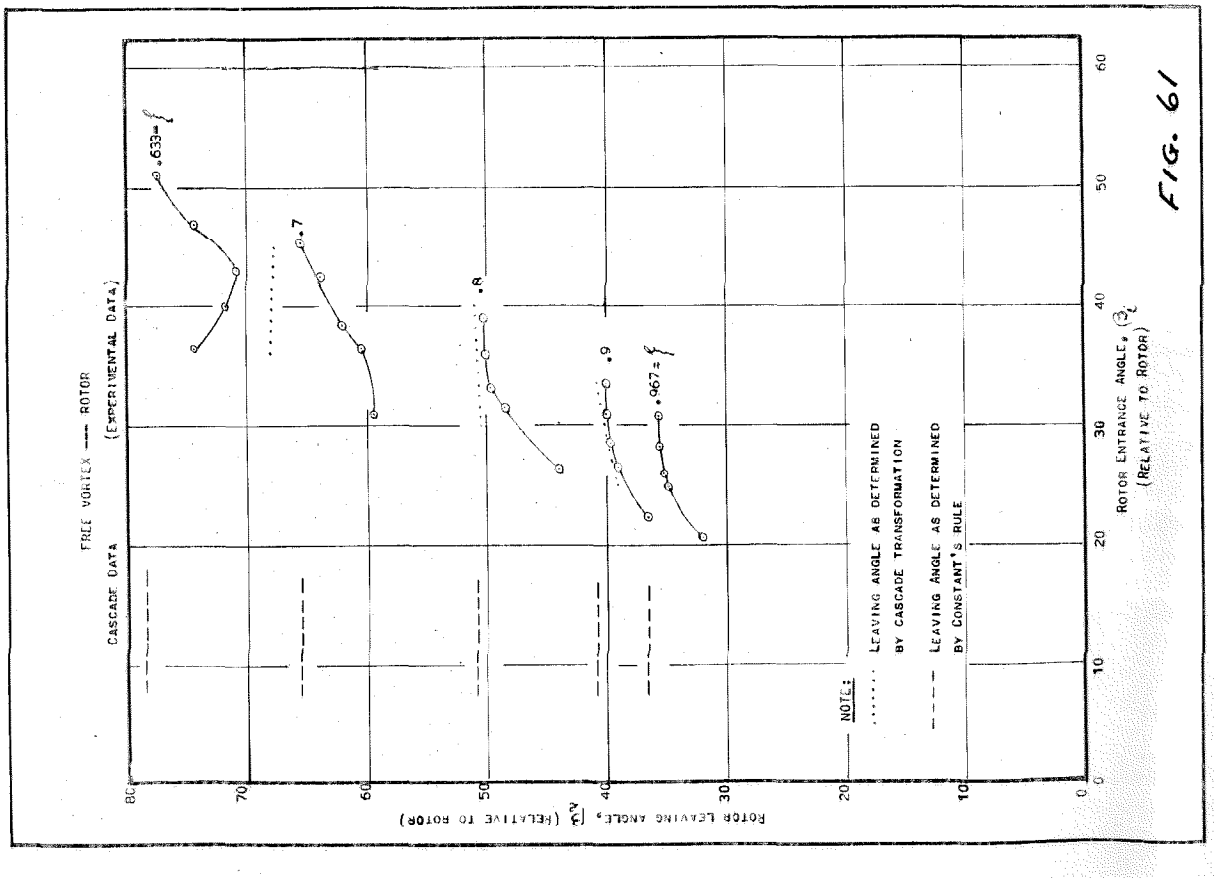
FREE VORTEX — ROTOR
CASCADE DATA (EXPERIMENTAL DATA)
ROTOR LEAVING ANGLE, β_2 (RELATIVE TO ROTOR)
ROTOR ENTRANCE ANGLE, β_1 (RELATIVE TO ROTOR)
NOTE:
..... LEAVING ANGLE AS DETERMINED BY CASCADE TRANSFORMATION
— — — LEAVING ANGLE AS DETERMINED BY CONSTANT'S RULE
.633
.7
.8
.9
.967

FIG. 61

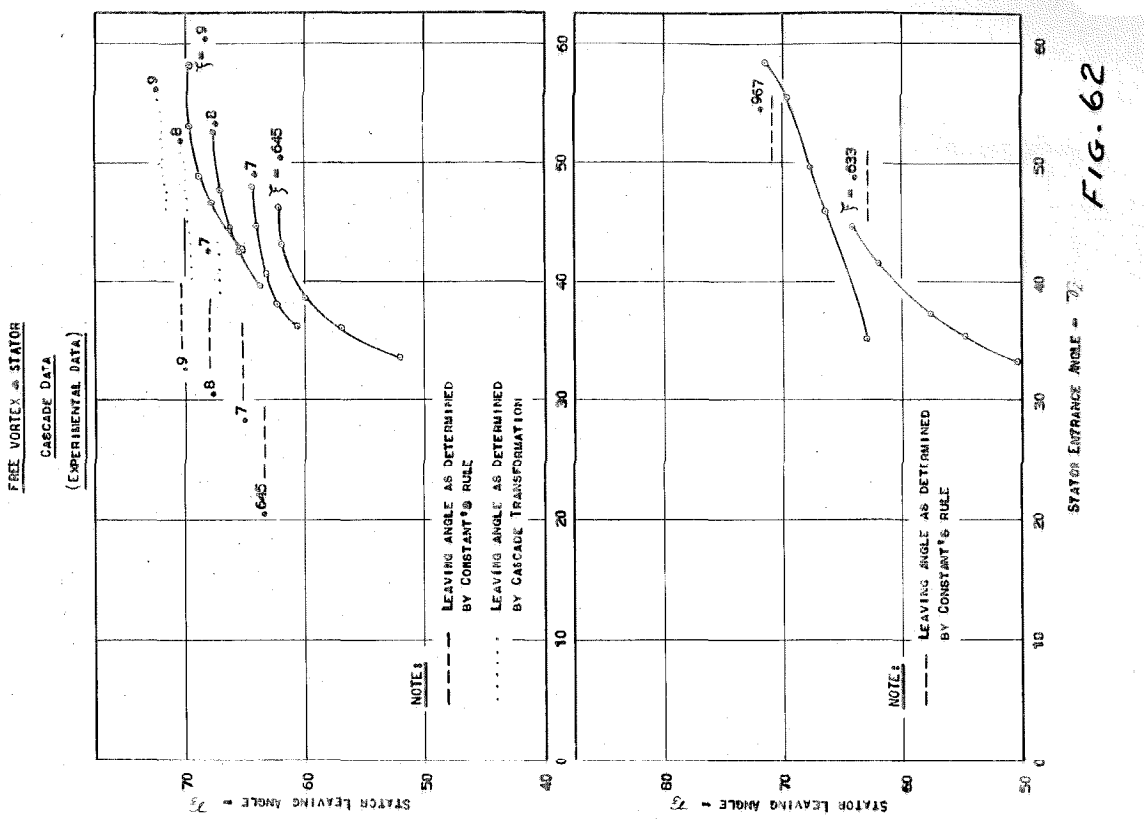
FREE VORTEX — STATOR
CASCADE DATA
(EXPERIMENTAL DATA)
STATOR LEAVING ANGLE = β_2
STATOR ENTRANCE ANGLE = β_1
NOTE:
— — — LEAVING ANGLE AS DETERMINED BY CONSTANT'S RULE
..... LEAVING ANGLE AS DETERMINED BY CASCADE TRANSFORMATION
.645
.7
.8
.9
.633
.967

FIG. 62

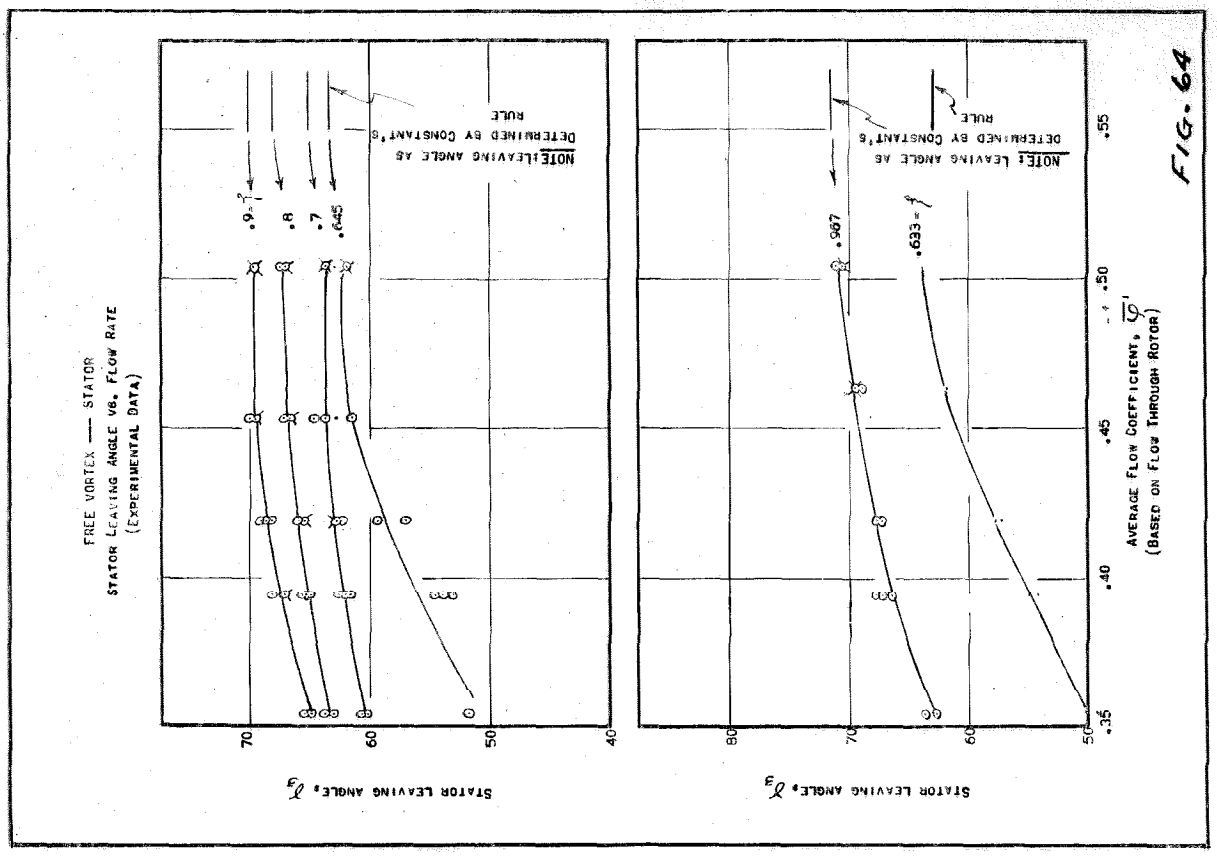
FREE VORTEX — STATOR
STATOR LEAVING ANGLE VS. FLOW RATE
(EXPERIMENTAL DATA)
NOTE: LEAVING ANGLE AS DETERMINED BY CONSTANT'S RULE
.9
.8
.7
.645
.967
.633
STATOR LEAVING ANGLE, β_3
AVERAGE FLOW COEFFICIENT, $\bar{\varphi}$
(BASED ON FLOW THROUGH ROTOR)

FIG. 64

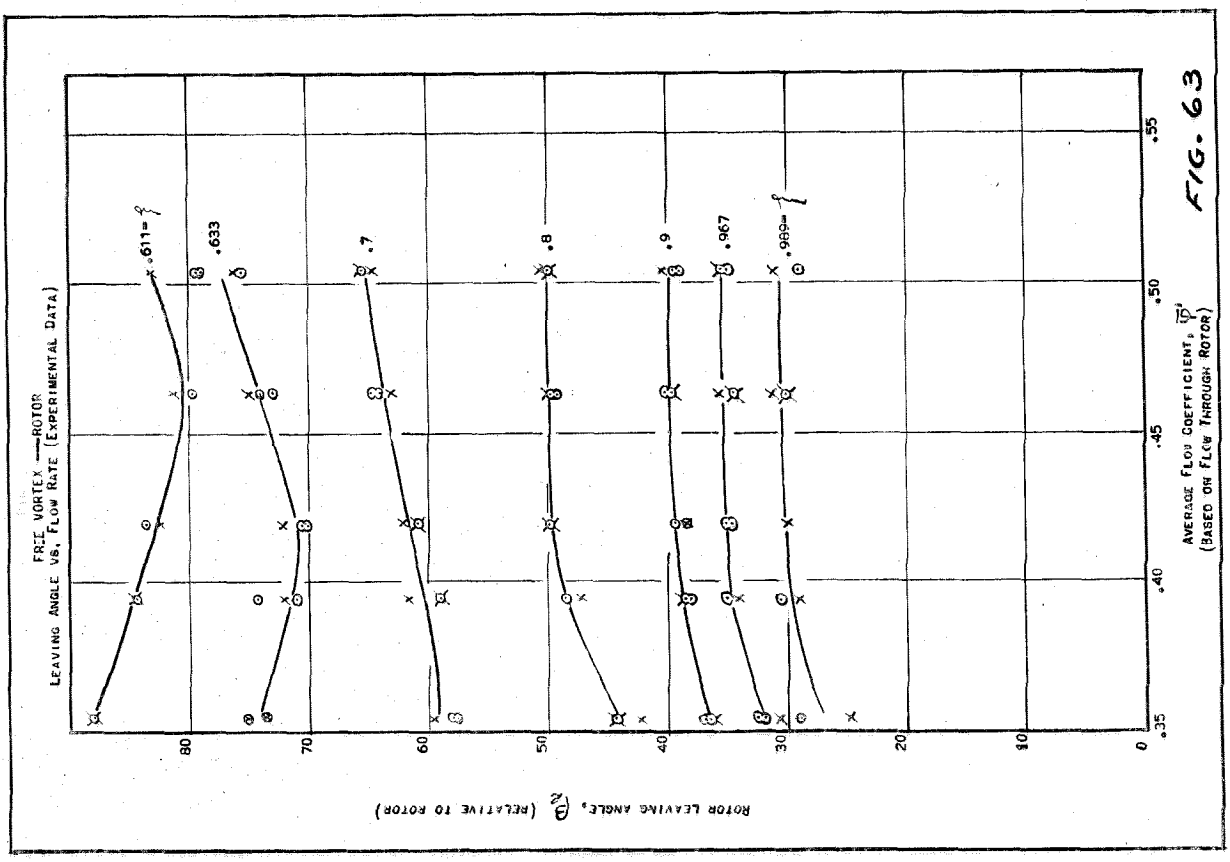
FREE VORTEX — ROTOR
LEAVING ANGLE VS. FLOW RATE (EXPERIMENTAL DATA)
.611
.633
.7
.8
.9
.967
.989
ROTOR LEAVING ANGLE, β_2 (RELATIVE TO ROTOR)
AVERAGE FLOW COEFFICIENT, $\bar{\varphi}$
(BASED ON FLOW THROUGH ROTOR)

FIG. 63

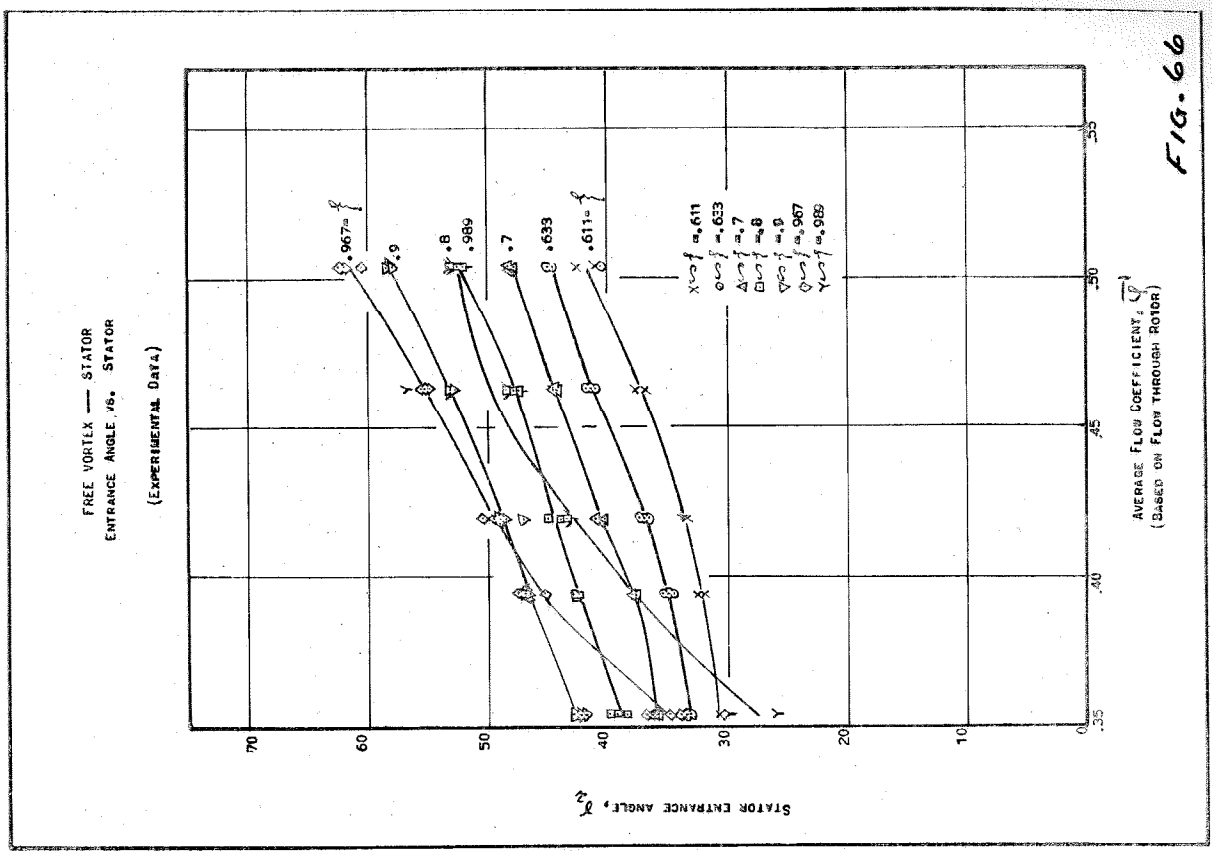
FREE VORTEX — STATOR
ENTRANCE ANGLE vs. STATOR
(EXPERIMENTAL DATA)
STATOR ENTRANCE ANGLE, β_2
AVERAGE FLOW COEFFICIENT, $\overline{\varphi}$
(BASED ON FLOW THROUGH ROTOR)
.967= f
.9
.8
.989
.7
.633
.611= f
X-○ f =.611
○-○ f =.633
△-△ f =.7
□-□ f =.8
▽-▽ f =.9
◇-◇ f =.967
Y-○ f =.989
Y
70
60
50
40
30
20
10
0
.35
.40
.45
.50
.55

FIG. 66

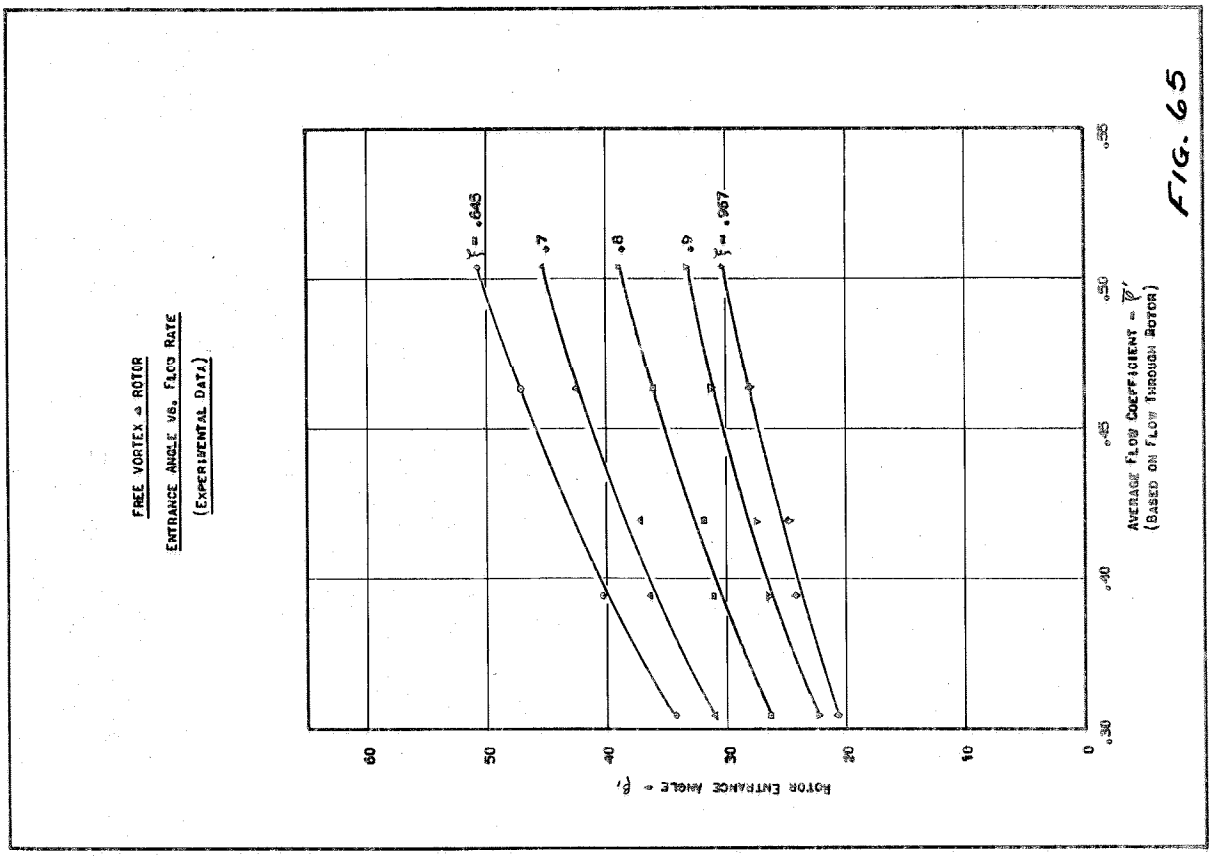
FREE VORTEX ⇒ ROTOR
ENTRANCE ANGLE vs. FLOW RATE
(EXPERIMENTAL DATA)
ROTOR ENTRANCE ANGLE = β_1'
AVERAGE FLOW COEFFICIENT = $\overline{\varphi}'$
(BASED ON FLOW THROUGH ROTOR)
Y = .645
.7
.8
.9
Y = .967
60
50
40
30
20
10
0
.30
.40
.45
.50
.55

FIG. 65

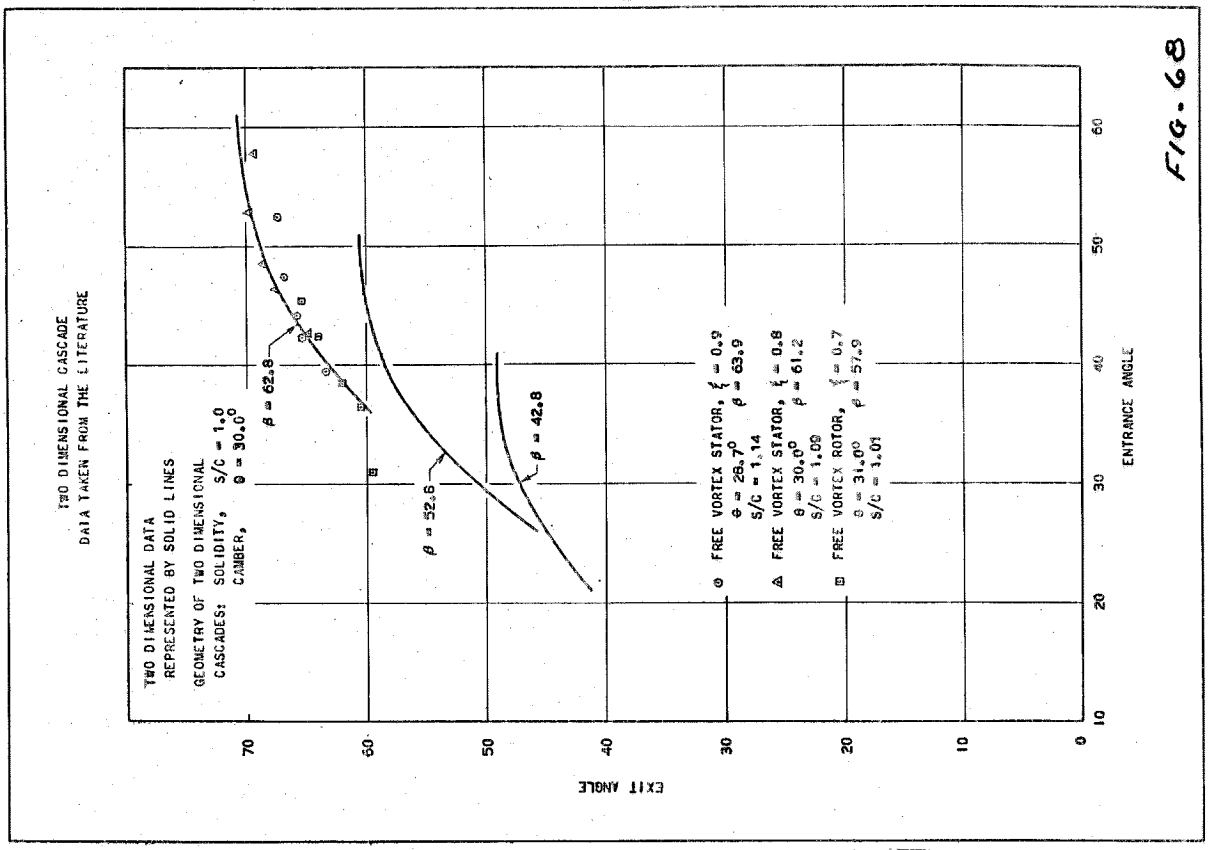
TWO DIMENSIONAL CASCADE
DATA TAKEN FROM THE LITERATURE
TWO DIMENSIONAL DATA
REPRESENTED BY SOLID LINES
GEOMETRY OF TWO DIMENSIONAL
CASCADES: SOLIDITY, S/C = 1.0
CAMBER, θ = 30.0°
β = 62.8
β = 52.6
β = 42.8
⊙ FREE VORTEX STATOR, ξ = 0.9
θ = 28.7° β = 63.9
S/C = 1.14
△ FREE VORTEX STATOR, ξ = 0.8
θ = 30.0° β = 61.2
S/C = 1.09
□ FREE VORTEX ROTOR, ξ = 0.7
θ = 31.0° β = 57.9
S/C = 1.01
EXIT ANGLE
ENTRANCE ANGLE
0
10
20
30
40
50
60
70

FIG. 68

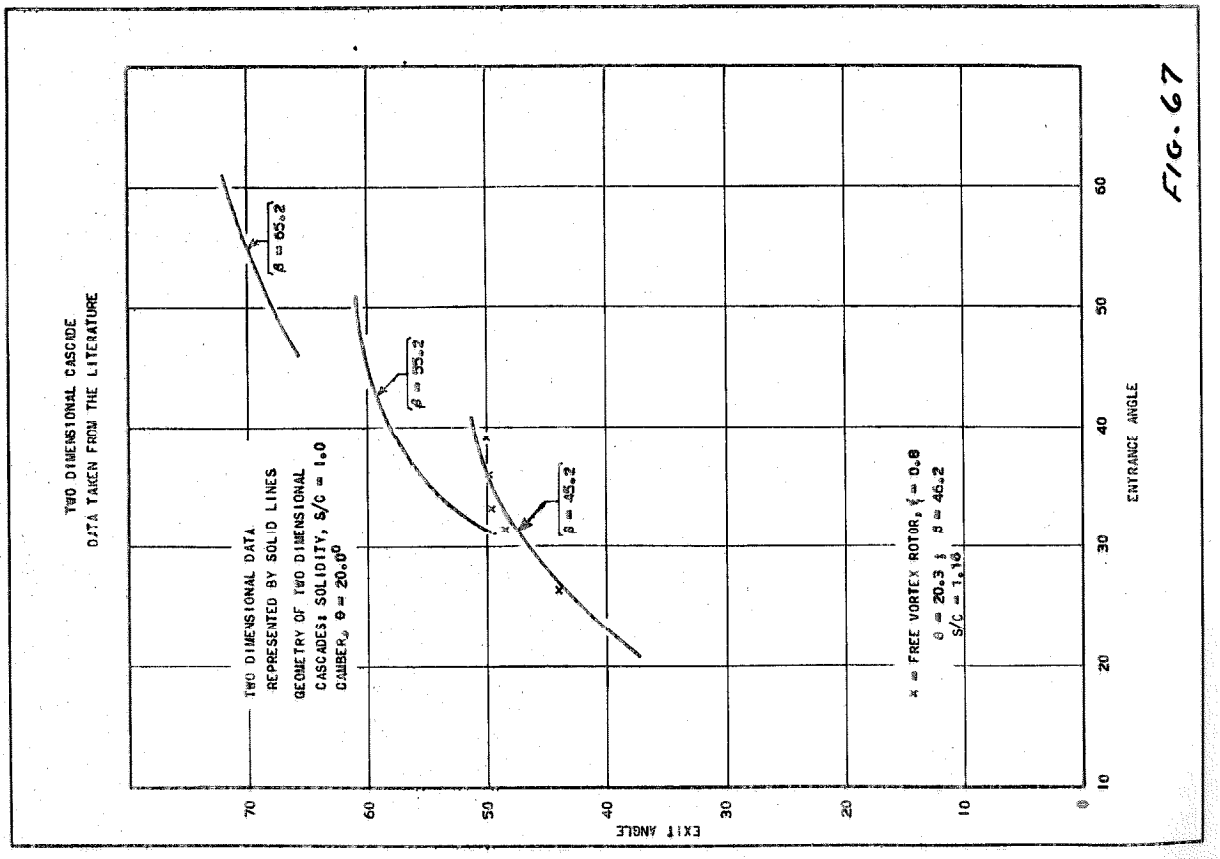
TWO DIMENSIONAL CASCADE
DATA TAKEN FROM THE LITERATURE
TWO DIMENSIONAL DATA
REPRESENTED BY SOLID LINES
GEOMETRY OF TWO DIMENSIONAL
CASCADES: SOLIDITY, S/C = 1.0
CAMBER, θ = 20.0°
β = 65.2
β = 55.2
β = 45.2
× = FREE VORTEX ROTOR, ξ = 0.8
θ = 20.3 β = 45.2
S/C = 1.16
EXIT ANGLE
ENTRANCE ANGLE
0
10
20
30
40
50
60
70

FIG. 67

FREE VORTEX ENTRANCE VANES

LEAVING ANGLE VS. RADIUS

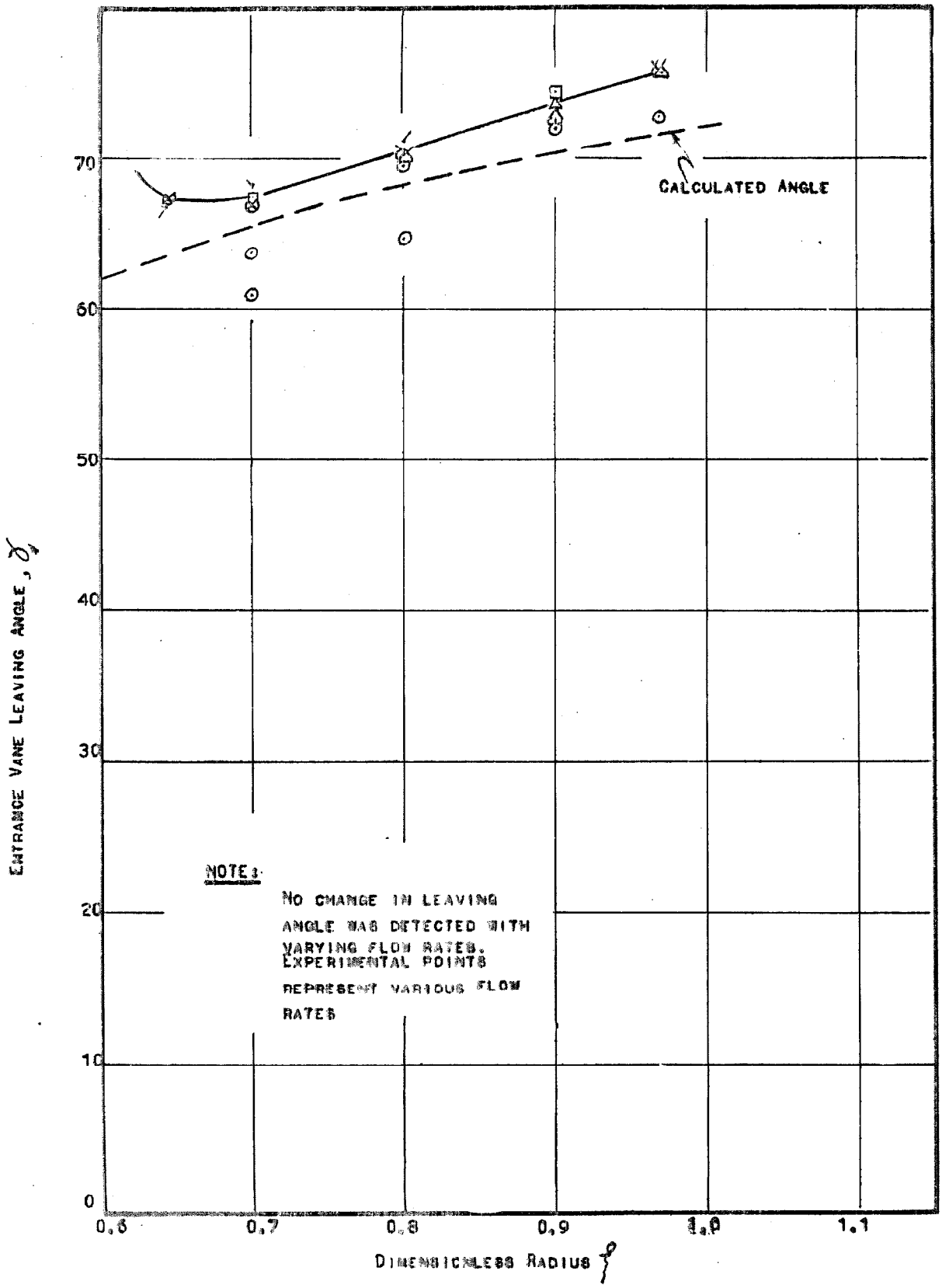

FIG. 69

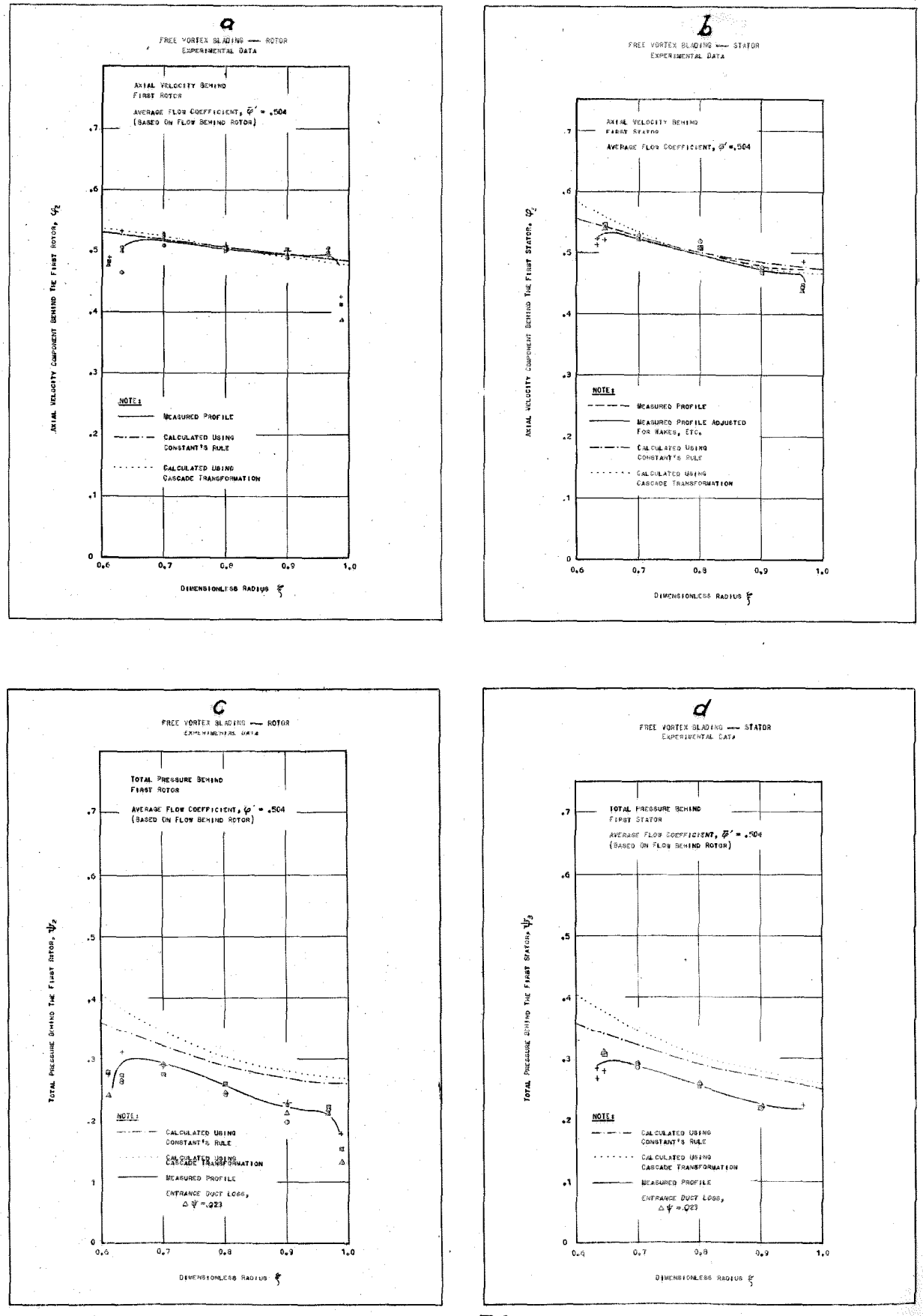
a
FREE VORTEX BLADING — ROTOR
EXPERIMENTAL DATA
AXIAL VELOCITY BEHIND
FIRST ROTOR
AVERAGE FLOW COEFFICIENT, $\bar{\varphi}' = .504$
(BASED ON FLOW BEHIND ROTOR)
AXIAL VELOCITY COMPONENT BEHIND THE FIRST ROTOR, φ_2
NOTE:
MEASURED PROFILE
CALCULATED USING CONSTANT'S RULE
CALCULATED USING CASCADE TRANSFORMATION
DIMENSIONLESS RADIUS ξ
b
FREE VORTEX BLADING — STATOR
EXPERIMENTAL DATA
AXIAL VELOCITY BEHIND
FIRST STATOR
AVERAGE FLOW COEFFICIENT, $\bar{\varphi}' = .504$
AXIAL VELOCITY COMPONENT BEHIND THE FIRST STATOR, φ_2
NOTE:
MEASURED PROFILE
MEASURED PROFILE ADJUSTED FOR WAKES, ETC.
CALCULATED USING CONSTANT'S RULE
CALCULATED USING CASCADE TRANSFORMATION
DIMENSIONLESS RADIUS ξ
c
FREE VORTEX BLADING — ROTOR
EXPERIMENTAL DATA
TOTAL PRESSURE BEHIND
FIRST ROTOR
AVERAGE FLOW COEFFICIENT, $\bar{\varphi}' = .504$
(BASED ON FLOW BEHIND ROTOR)
TOTAL PRESSURE BEHIND THE FIRST ROTOR, ψ_2
NOTE:
CALCULATED USING CONSTANT'S RULE
CALCULATED USING CASCADE TRANSFORMATION
MEASURED PROFILE
ENTRANCE DUCT LOSS, $\Delta\psi = .023$
DIMENSIONLESS RADIUS ξ
d
FREE VORTEX BLADING — STATOR
EXPERIMENTAL DATA
TOTAL PRESSURE BEHIND
FIRST STATOR
AVERAGE FLOW COEFFICIENT, $\bar{\varphi}' = .504$
(BASED ON FLOW BEHIND ROTOR)
TOTAL PRESSURE BEHIND THE FIRST STATOR, ψ_3
NOTE:
CALCULATED USING CONSTANT'S RULE
CALCULATED USING CASCADE TRANSFORMATION
MEASURED PROFILE
ENTRANCE DUCT LOSS, $\Delta\psi = .023$
DIMENSIONLESS RADIUS ξ

FIG. 70

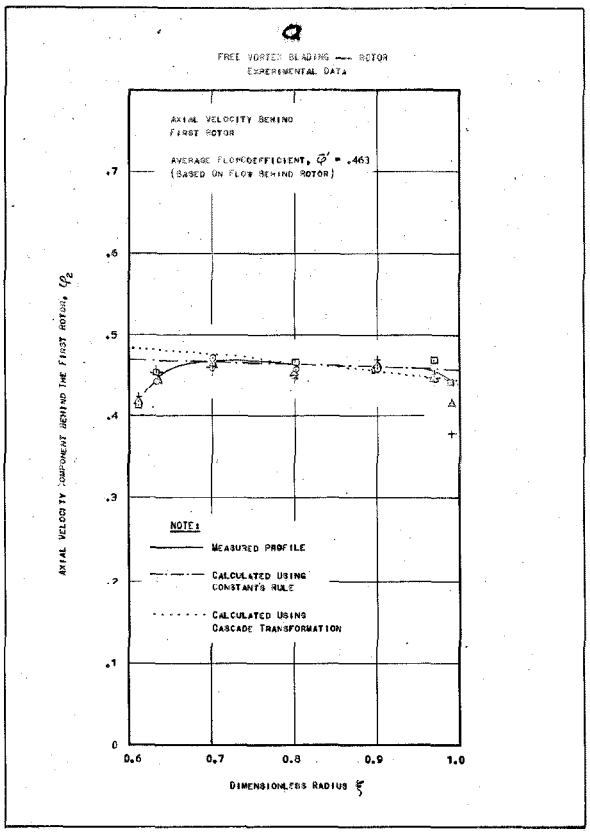
a
FREE VORTEX BLADING — ROTOR
EXPERIMENTAL DATA
AXIAL VELOCITY BEHIND FIRST ROTOR
AVERAGE FLOW COEFFICIENT, $\bar{\varphi}'$ = .463
(BASED ON FLOW BEHIND ROTOR)
NOTE:
MEASURED PROFILE
CALCULATED USING CONSTANT'S RULE
CALCULATED USING CASCADE TRANSFORMATION
AXIAL VELOCITY COMPONENT BEHIND THE FIRST ROTOR, φ_2
DIMENSIONLESS RADIUS ξ

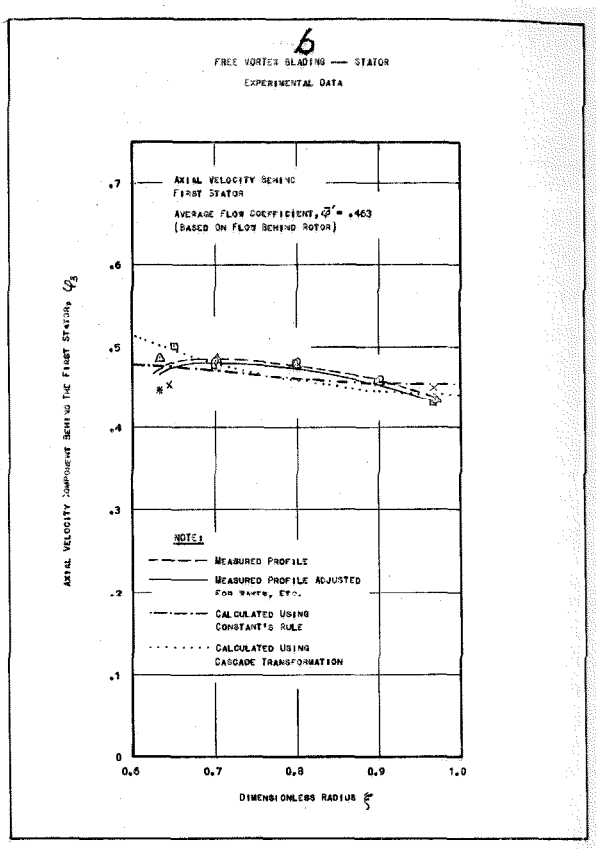
b
FREE VORTEX BLADING — STATOR
EXPERIMENTAL DATA
AXIAL VELOCITY BEHIND FIRST STATOR
AVERAGE FLOW COEFFICIENT, $\bar{\varphi}'$ = .463
(BASED ON FLOW BEHIND ROTOR)
NOTE:
MEASURED PROFILE
MEASURED PROFILE ADJUSTED FOR WAKES, ETC.
CALCULATED USING CONSTANT'S RULE
CALCULATED USING CASCADE TRANSFORMATION
AXIAL VELOCITY COMPONENT BEHIND THE FIRST STATOR, φ_3
DIMENSIONLESS RADIUS ξ

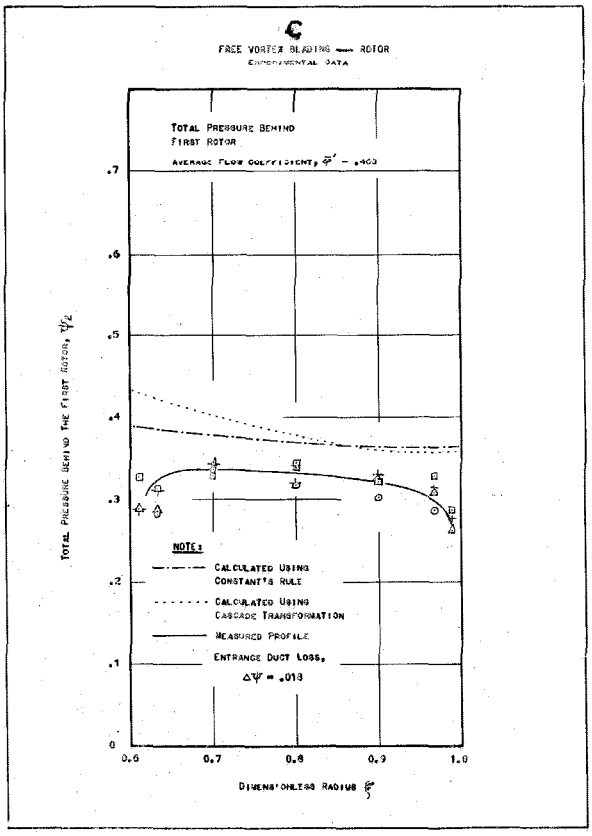
c
FREE VORTEX BLADING — ROTOR
EXPERIMENTAL DATA
TOTAL PRESSURE BEHIND FIRST ROTOR
AVERAGE FLOW COEFFICIENT, $\bar{\varphi}'$ = .463
NOTE:
CALCULATED USING CONSTANT'S RULE
CALCULATED USING CASCADE TRANSFORMATION
MEASURED PROFILE
ENTRANCE DUCT LOSS, $\Delta\Psi$ = .018
TOTAL PRESSURE BEHIND THE FIRST ROTOR, Ψ_2
DIMENSIONLESS RADIUS ξ

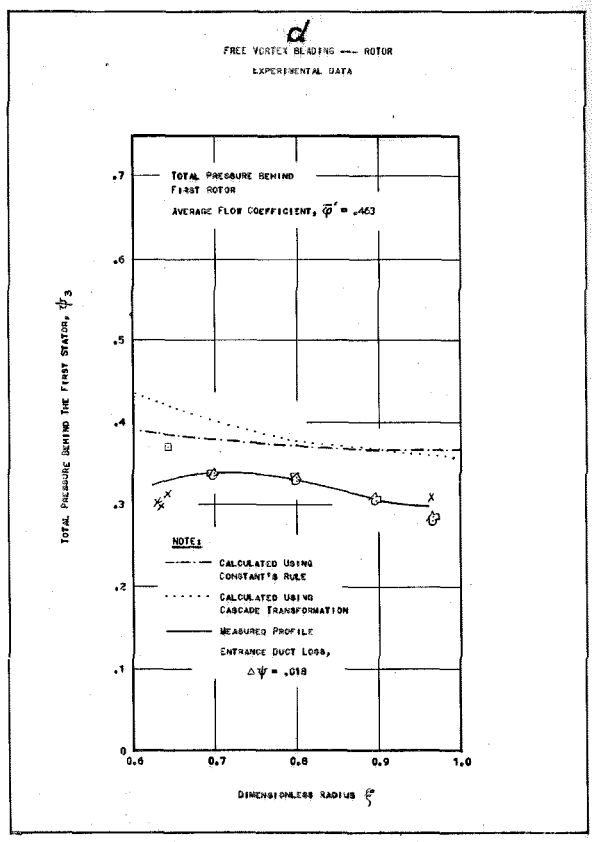
d
FREE VORTEX BLADING — ROTOR
EXPERIMENTAL DATA
TOTAL PRESSURE BEHIND FIRST ROTOR
AVERAGE FLOW COEFFICIENT, $\bar{\varphi}'$ = .463
NOTE:
CALCULATED USING CONSTANT'S RULE
CALCULATED USING CASCADE TRANSFORMATION
MEASURED PROFILE
ENTRANCE DUCT LOSS, $\Delta\Psi$ = .018
TOTAL PRESSURE BEHIND THE FIRST STATOR, Ψ_3
DIMENSIONLESS RADIUS ξ

FIG. 71

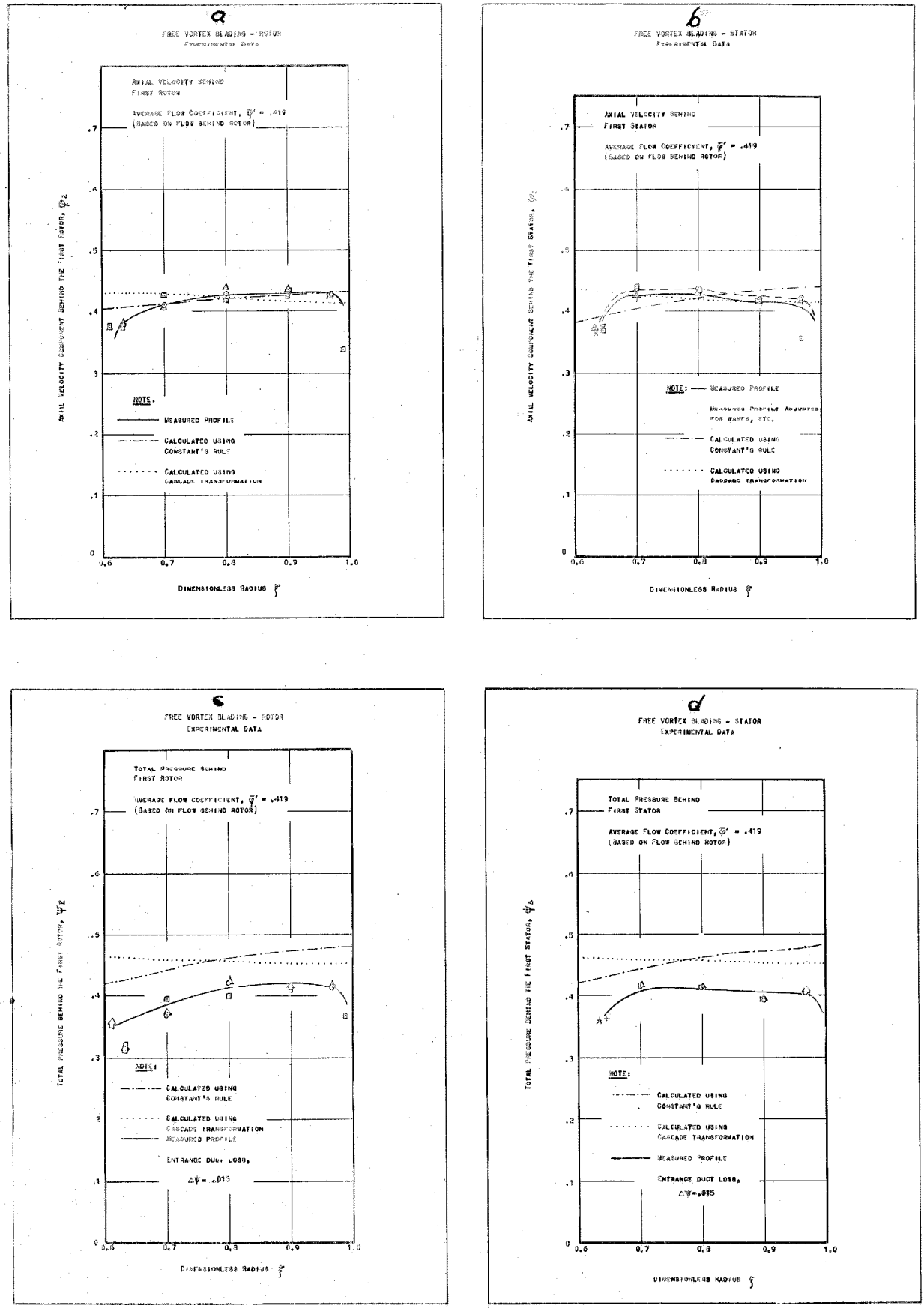
a
FREE VORTEX BLADING - ROTOR
EXPERIMENTAL DATA
AXIAL VELOCITY BEHIND FIRST ROTOR
AVERAGE FLOW COEFFICIENT, $\bar{\phi}'$ = .419
(BASED ON FLOW BEHIND ROTOR)
AXIAL VELOCITY COMPONENT BEHIND THE FIRST ROTOR, ϕ_2
NOTE:
MEASURED PROFILE
CALCULATED USING CONSTANT'S RULE
CALCULATED USING CASCADE TRANSFORMATION
DIMENSIONLESS RADIUS $\bar{r}$
b
FREE VORTEX BLADING - STATOR
EXPERIMENTAL DATA
AXIAL VELOCITY BEHIND FIRST STATOR
AVERAGE FLOW COEFFICIENT, $\bar{\phi}'$ = .419
(BASED ON FLOW BEHIND ROTOR)
AXIAL VELOCITY COMPONENT BEHIND THE FIRST STATOR, ϕ_3
NOTE: MEASURED PROFILE
MEASURED PROFILE ADJUSTED FOR WAKES, ETC.
CALCULATED USING CONSTANT'S RULE
CALCULATED USING CASCADE TRANSFORMATION
DIMENSIONLESS RADIUS $\bar{r}$
c
FREE VORTEX BLADING - ROTOR
EXPERIMENTAL DATA
TOTAL PRESSURE BEHIND FIRST ROTOR
AVERAGE FLOW COEFFICIENT, $\bar{\phi}'$ = .419
(BASED ON FLOW BEHIND ROTOR)
TOTAL PRESSURE BEHIND THE FIRST ROTOR, Ψ_2
NOTE:
CALCULATED USING CONSTANT'S RULE
CALCULATED USING CASCADE TRANSFORMATION
MEASURED PROFILE
ENTRANCE DUCT LOSS, $\Delta\Psi$ = .015
DIMENSIONLESS RADIUS $\bar{r}$
d
FREE VORTEX BLADING - STATOR
EXPERIMENTAL DATA
TOTAL PRESSURE BEHIND FIRST STATOR
AVERAGE FLOW COEFFICIENT, $\bar{\phi}'$ = .419
(BASED ON FLOW BEHIND ROTOR)
TOTAL PRESSURE BEHIND THE FIRST STATOR, Ψ_3
NOTE:
CALCULATED USING CONSTANT'S RULE
CALCULATED USING CASCADE TRANSFORMATION
MEASURED PROFILE
ENTRANCE DUCT LOSS, $\Delta\Psi$=.015
DIMENSIONLESS RADIUS $\bar{r}$

FIG. 72

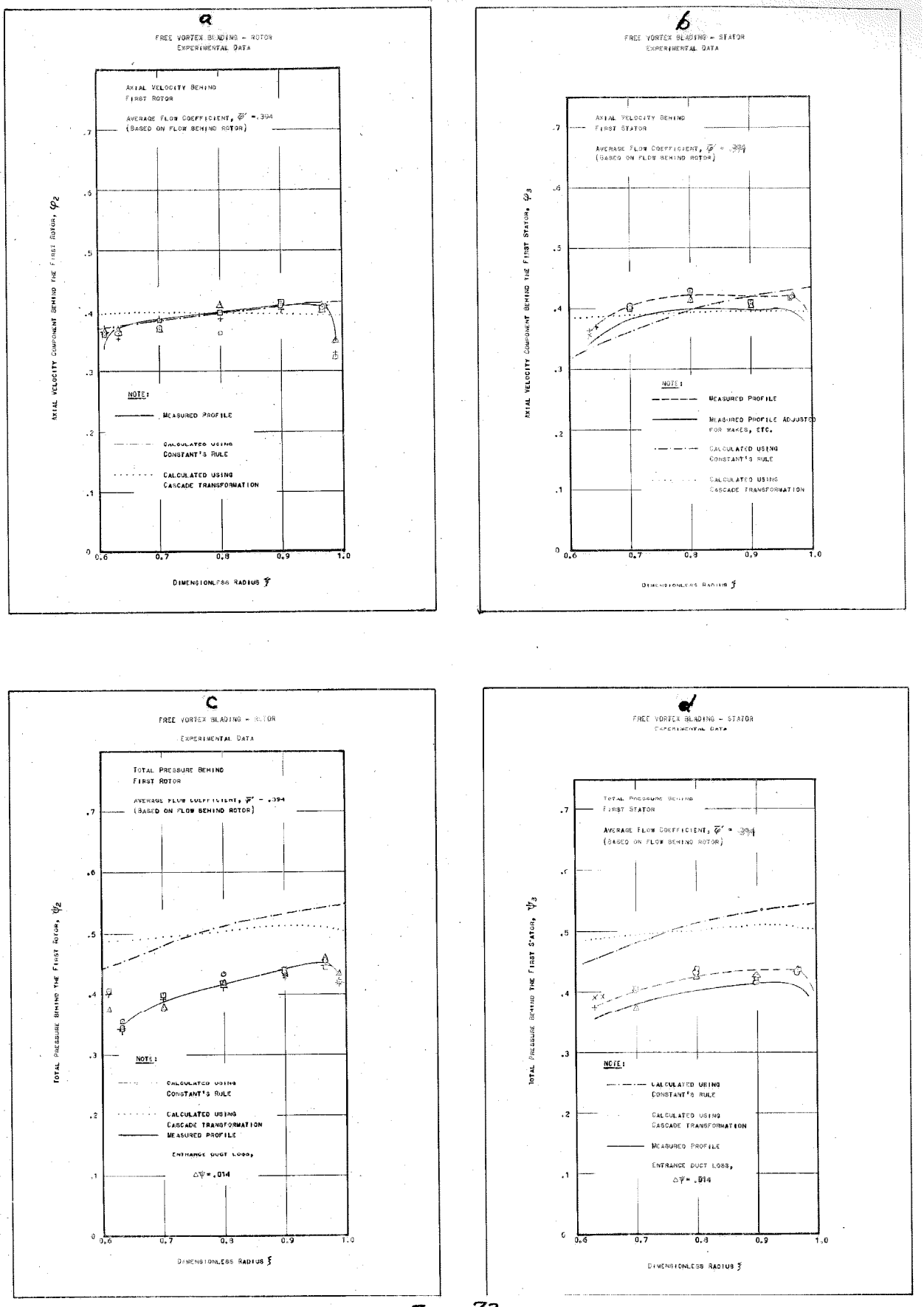
a
FREE VORTEX BLADING - ROTOR
EXPERIMENTAL DATA
AXIAL VELOCITY BEHIND
FIRST ROTOR
AVERAGE FLOW COEFFICIENT, $\bar{\varphi}'$ = .394
(BASED ON FLOW BEHIND ROTOR)
AXIAL VELOCITY COMPONENT BEHIND THE FIRST ROTOR, φ_2
NOTE:
MEASURED PROFILE
CALCULATED USING CONSTANT'S RULE
CALCULATED USING CASCADE TRANSFORMATION
DIMENSIONLESS RADIUS $\bar{r}$
b
FREE VORTEX BLADING - STATOR
EXPERIMENTAL DATA
AXIAL VELOCITY BEHIND
FIRST STATOR
AVERAGE FLOW COEFFICIENT, $\bar{\varphi}'$ = .394
(BASED ON FLOW BEHIND ROTOR)
AXIAL VELOCITY COMPONENT BEHIND THE FIRST STATOR, φ_3
NOTE:
MEASURED PROFILE
MEASURED PROFILE ADJUSTED FOR WAKES, ETC.
CALCULATED USING CONSTANT'S RULE
CALCULATED USING CASCADE TRANSFORMATION
DIMENSIONLESS RADIUS $\bar{r}$
c
FREE VORTEX BLADING - ROTOR
EXPERIMENTAL DATA
TOTAL PRESSURE BEHIND
FIRST ROTOR
AVERAGE FLOW COEFFICIENT, $\bar{\varphi}'$ = .394
(BASED ON FLOW BEHIND ROTOR)
TOTAL PRESSURE BEHIND THE FIRST ROTOR, ψ_2
NOTE:
CALCULATED USING CONSTANT'S RULE
CALCULATED USING CASCADE TRANSFORMATION
MEASURED PROFILE
ENTRANCE DUCT LOSS, $\Delta\bar{\psi}$ = .014
DIMENSIONLESS RADIUS $\bar{r}$
d
FREE VORTEX BLADING - STATOR
EXPERIMENTAL DATA
TOTAL PRESSURE BEHIND
FIRST STATOR
AVERAGE FLOW COEFFICIENT, $\bar{\varphi}'$ = .394
(BASED ON FLOW BEHIND ROTOR)
TOTAL PRESSURE BEHIND THE FIRST STATOR, ψ_3
NOTE:
CALCULATED USING CONSTANT'S RULE
CALCULATED USING CASCADE TRANSFORMATION
MEASURED PROFILE
ENTRANCE DUCT LOSS, $\Delta\bar{\psi}$ = .014
DIMENSIONLESS RADIUS $\bar{r}$

FIG. 73

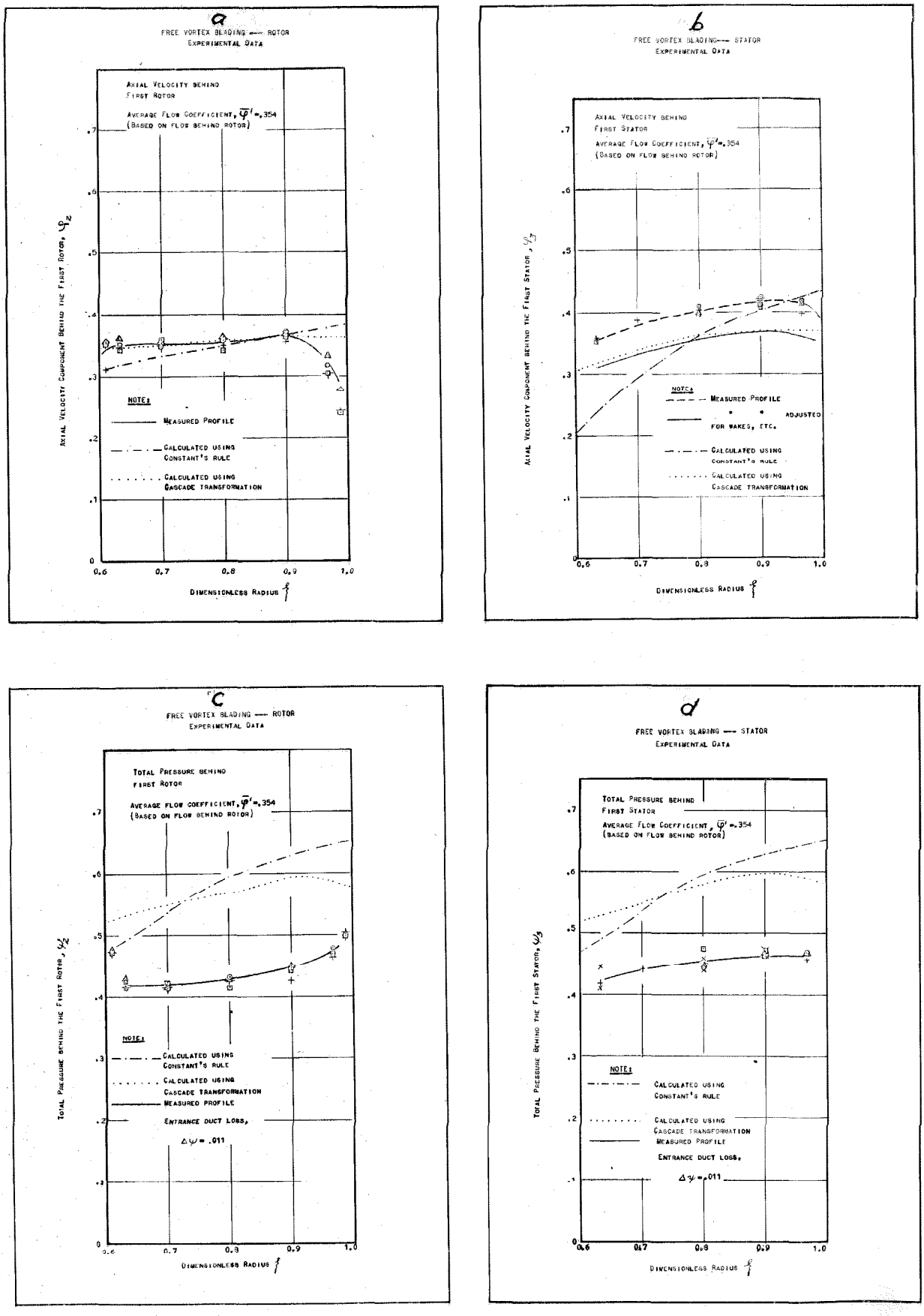
a
FREE VORTEX BLADING — ROTOR
EXPERIMENTAL DATA
AXIAL VELOCITY BEHIND
FIRST ROTOR
AVERAGE FLOW COEFFICIENT, $\bar{\varphi}' = .354$
(BASED ON FLOW BEHIND ROTOR)
AXIAL VELOCITY COMPONENT BEHIND THE FIRST ROTOR, ψ_2
NOTE:
MEASURED PROFILE
CALCULATED USING CONSTANT'S RULE
CALCULATED USING CASCADE TRANSFORMATION
DIMENSIONLESS RADIUS $\bar{r}$
b
FREE VORTEX BLADING — STATOR
EXPERIMENTAL DATA
AXIAL VELOCITY BEHIND
FIRST STATOR
AVERAGE FLOW COEFFICIENT, $\bar{\varphi}' = .354$
(BASED ON FLOW BEHIND ROTOR)
AXIAL VELOCITY COMPONENT BEHIND THE FIRST STATOR, ψ_3
NOTE:
MEASURED PROFILE
ADJUSTED FOR WAKES, ETC.
CALCULATED USING CONSTANT'S RULE
CALCULATED USING CASCADE TRANSFORMATION
DIMENSIONLESS RADIUS $\bar{r}$
c
FREE VORTEX BLADING — ROTOR
EXPERIMENTAL DATA
TOTAL PRESSURE BEHIND
FIRST ROTOR
AVERAGE FLOW COEFFICIENT, $\bar{\varphi}' = .354$
(BASED ON FLOW BEHIND ROTOR)
TOTAL PRESSURE BEHIND THE FIRST ROTOR, ψ_2
NOTE:
CALCULATED USING CONSTANT'S RULE
CALCULATED USING CASCADE TRANSFORMATION
MEASURED PROFILE
ENTRANCE DUCT LOSS, $\Delta\psi = .011$
DIMENSIONLESS RADIUS $\bar{r}$
d
FREE VORTEX BLADING — STATOR
EXPERIMENTAL DATA
TOTAL PRESSURE BEHIND
FIRST STATOR
AVERAGE FLOW COEFFICIENT, $\bar{\varphi}' = .354$
(BASED ON FLOW BEHIND ROTOR)
TOTAL PRESSURE BEHIND THE FIRST STATOR, ψ_3
NOTE:
CALCULATED USING CONSTANT'S RULE
CALCULATED USING CASCADE TRANSFORMATION
MEASURED PROFILE
ENTRANCE DUCT LOSS, $\Delta\psi = .011$
DIMENSIONLESS RADIUS $\bar{r}$

FIG. 74

a

SUMMARY GRAPH

AXIAL VELOCITY COMPONENT BEHIND FIRST ROTOR

FREE VORTEX BLADING

(CALCULATED DATA - CONSTANT'S RULE)

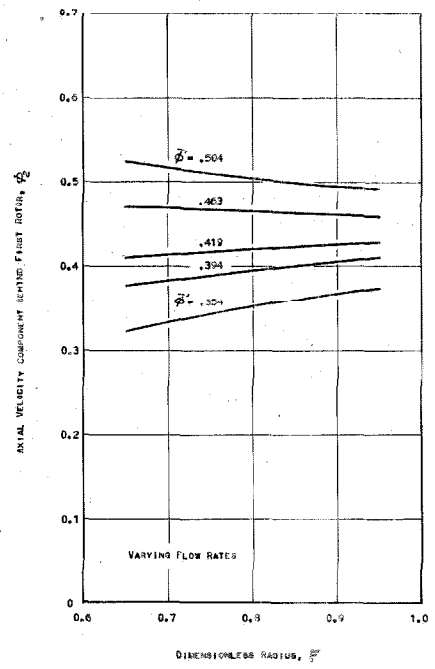

b

SUMMARY GRAPH

AXIAL VELOCITY COMPONENT BEHIND FIRST ROTOR

FREE VORTEX BLADING

(MEASURED DATA)

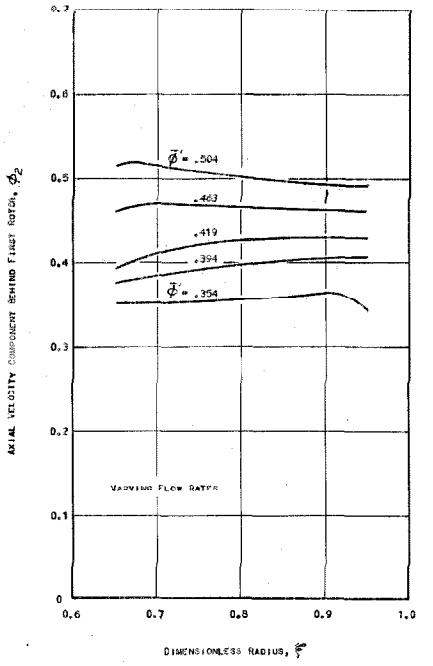

c

SUMMARY GRAPH

TOTAL PRESSURE BEHIND FIRST STAGE

FREE VORTEX BLADING

(CALCULATED DATA - CONSTANT'S RULE)

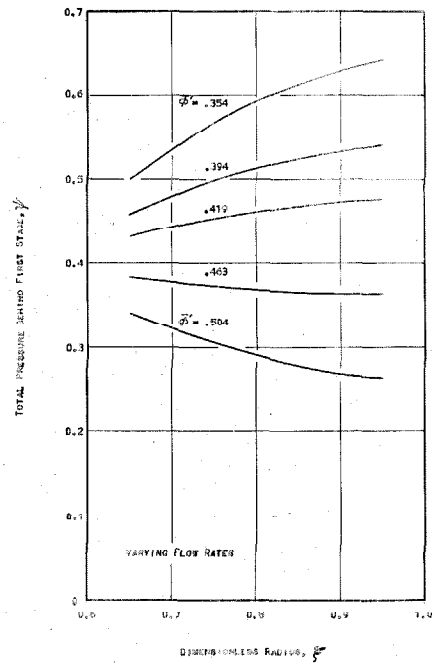

d

SUMMARY GRAPH

TOTAL PRESSURE BEHIND FIRST ROTOR

FREE VORTEX BLADING

(MEASURED DATA)

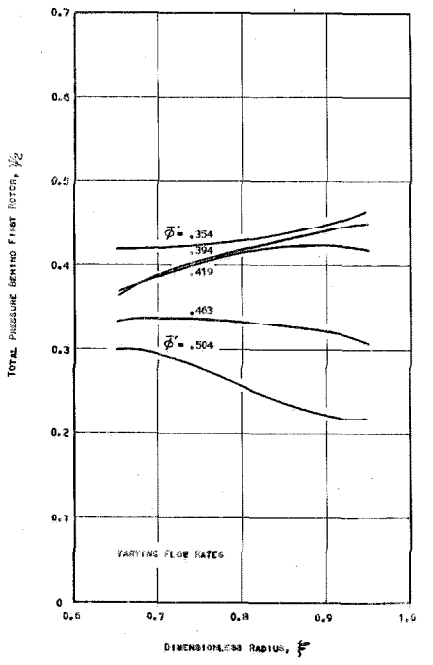

NOTE: ENTRANCE DUCT LOSS TO BE ADDED

Fig. 75

a

SUMMARY GRAPH

AXIAL VELOCITY COMPONENT BEHIND FIRST STATOR

FREE VORTEX BLADING

(CALCULATED DATA - CONSTANT'S RULE)

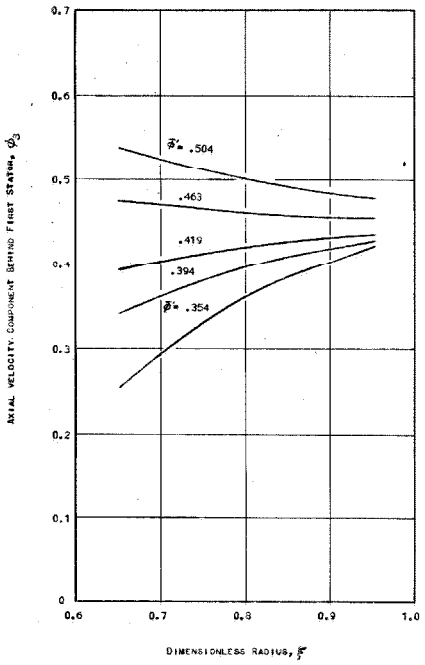

b

SUMMARY GRAPH

AXIAL VELOCITY COMPONENT BEHIND FIRST STATOR

FREE VORTEX BLADING

(MEASURED DATA)

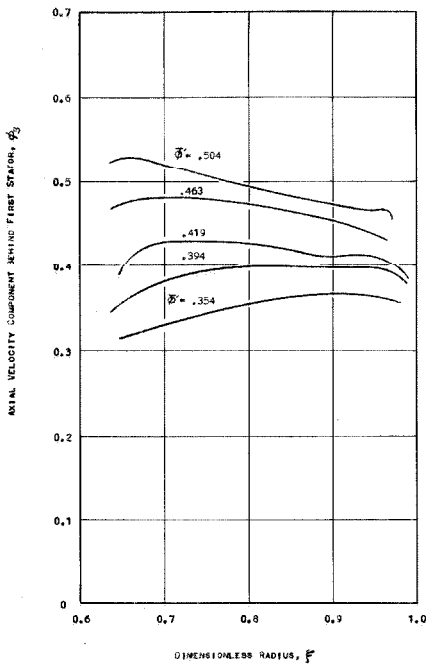

c

SUMMARY GRAPH

TOTAL PRESSURE BEHIND FIRST STAGE

FREE VORTEX BLADING

(CALCULATED DATA - CONSTANT'S RULE)

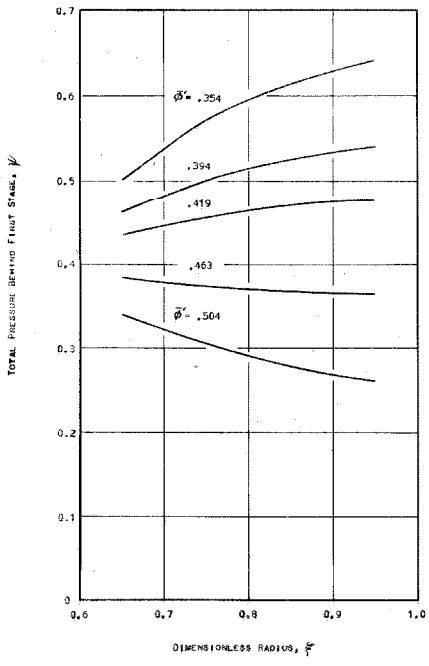

d

SUMMARY GRAPH

TOTAL PRESSURE BEHIND FIRST STATOR

FREE VORTEX BLADING

(MEASURED DATA)

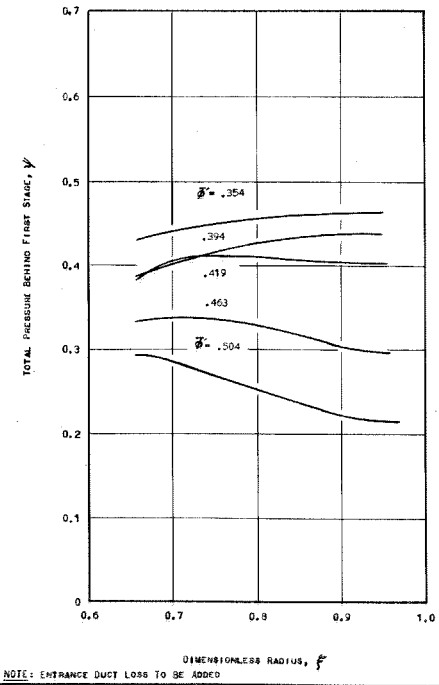

NOTE: ENTRANCE DUCT LOSS TO BE ADDED

FIG. 76

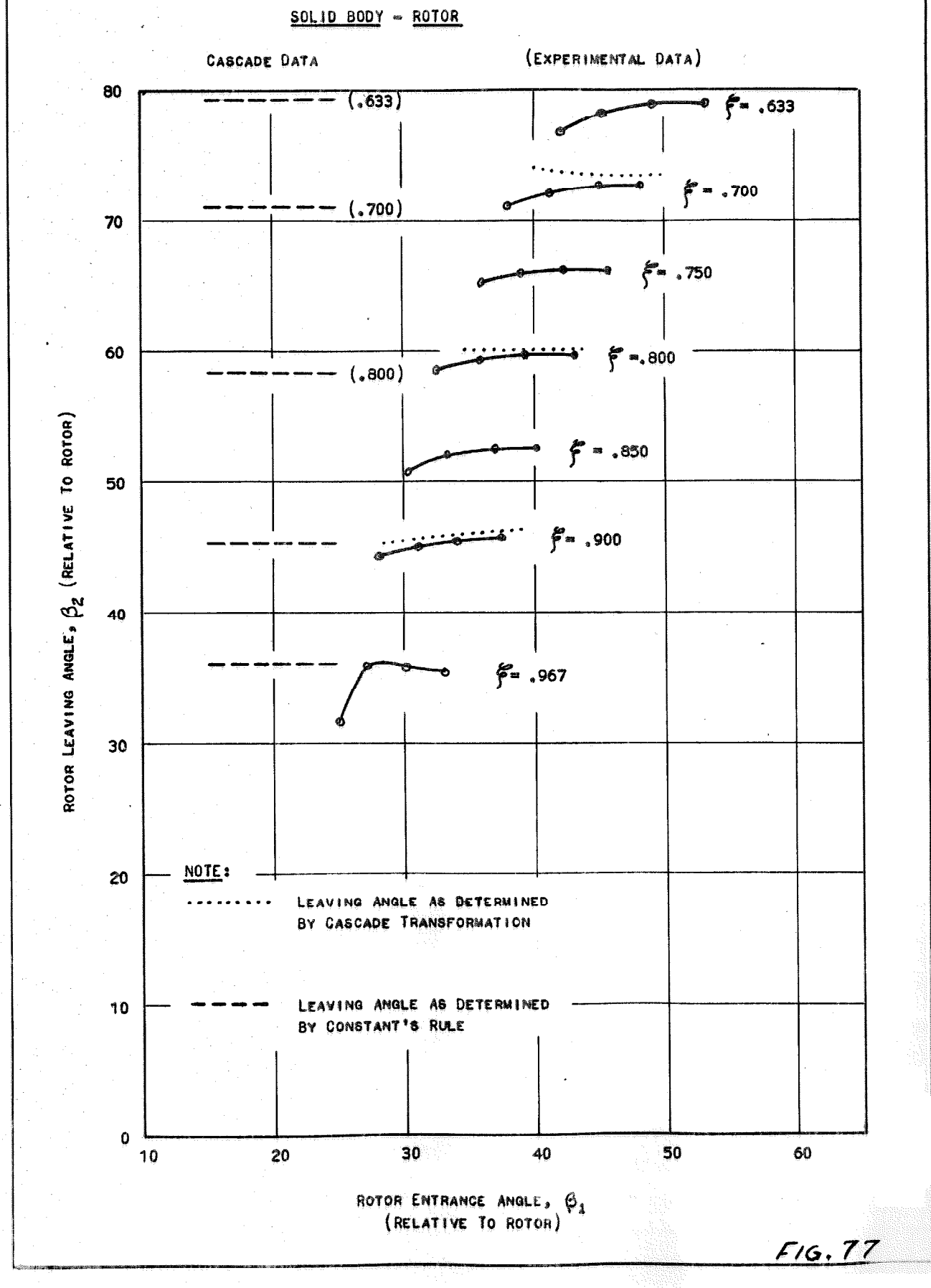
SOLID BODY - ROTOR
CASCADE DATA
(EXPERIMENTAL DATA)
(.633)
(.700)
(.800)
ξ = .633
ξ = .700
ξ = .750
ξ = .800
ξ = .850
ξ = .900
ξ = .967
ROTOR LEAVING ANGLE, β2 (RELATIVE TO ROTOR)
ROTOR ENTRANCE ANGLE, β1 (RELATIVE TO ROTOR)
0
10
20
30
40
50
60
70
80
NOTE:
LEAVING ANGLE AS DETERMINED BY CASCADE TRANSFORMATION
LEAVING ANGLE AS DETERMINED BY CONSTANT'S RULE

FIG. 77

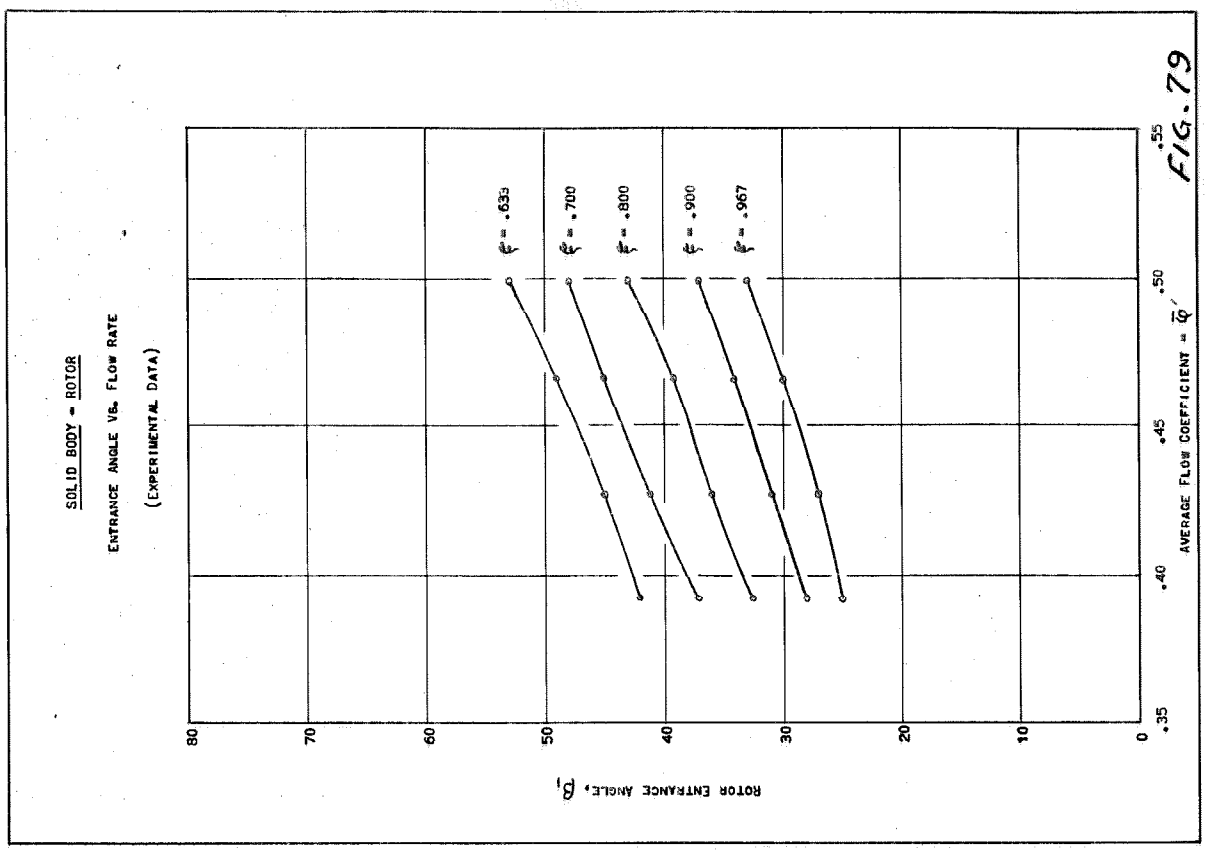
SOLID BODY - ROTOR
ENTRANCE ANGLE VS. FLOW RATE
(EXPERIMENTAL DATA)
β_f = .633
β_f = .700
β_f = .800
β_f = .900
β_f = .967
ROTOR ENTRANCE ANGLE, β_1
AVERAGE FLOW COEFFICIENT = $\bar{\varphi}'$
0
10
20
30
40
50
60
70
80
.35
.40
.45
.50
.55

FIG. 79

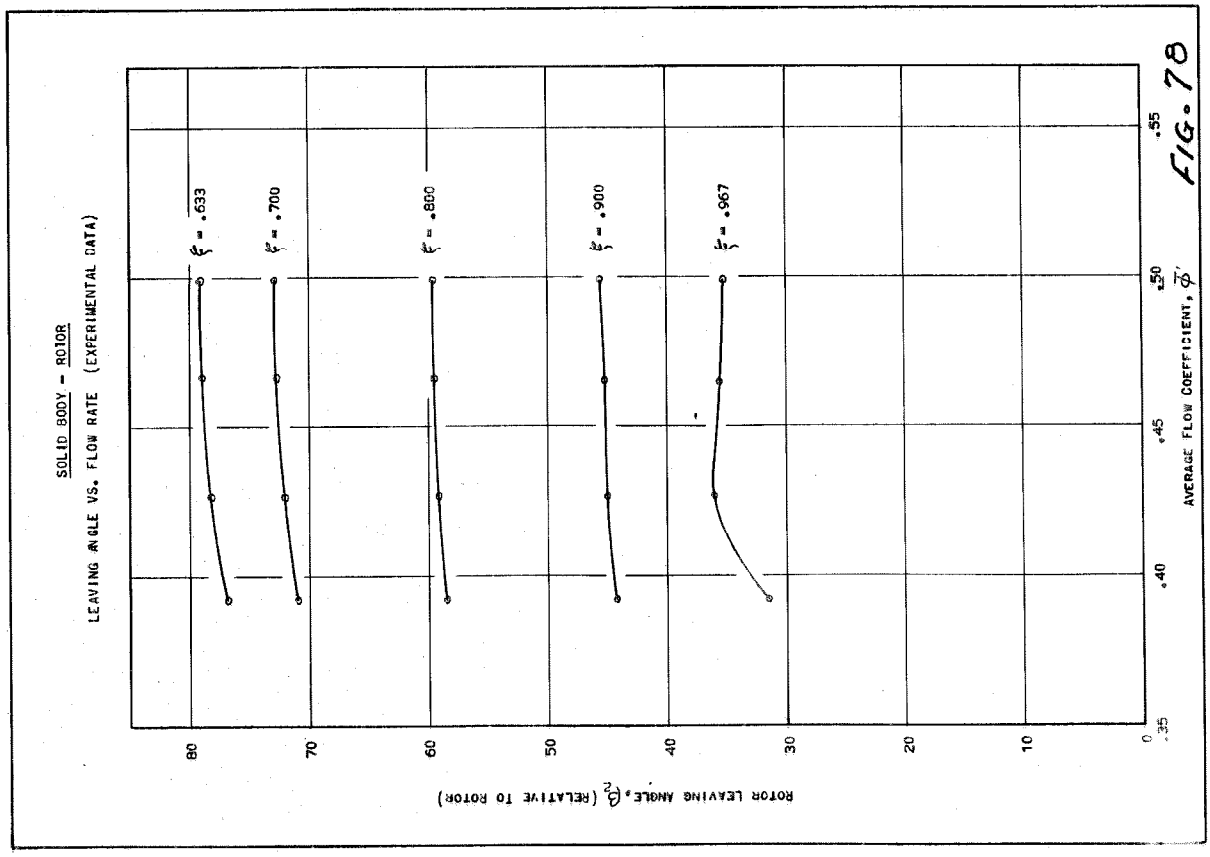
SOLID BODY - ROTOR
LEAVING ANGLE VS. FLOW RATE (EXPERIMENTAL DATA)
β_f = .633
β_f = .700
β_f = .800
β_f = .900
β_f = .967
ROTOR LEAVING ANGLE, β_2 (RELATIVE TO ROTOR)
AVERAGE FLOW COEFFICIENT, $\bar{\varphi}'$
0
10
20
30
40
50
60
70
80
.35
.40
.45
.50
.55

FIG. 78

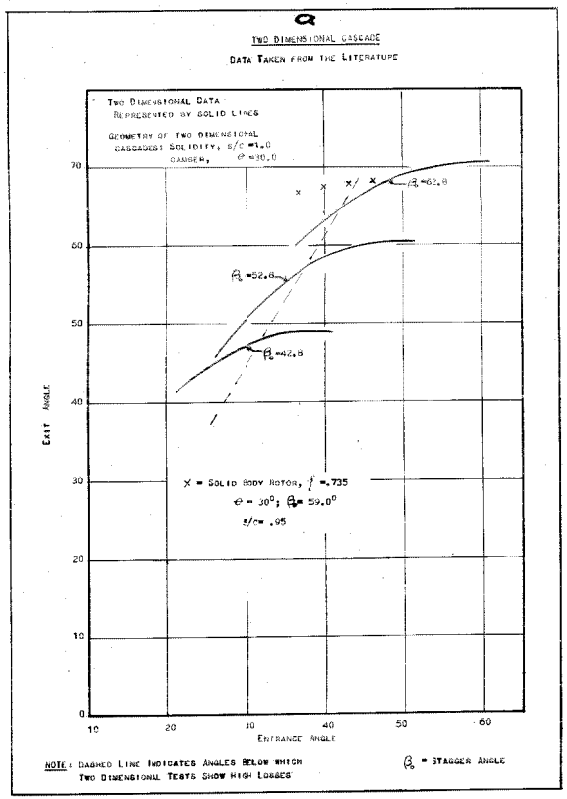
a
TWO DIMENSIONAL CASCADE
DATA TAKEN FROM THE LITERATURE
TWO DIMENSIONAL DATA REPRESENTED BY SOLID LINES
GEOMETRY OF TWO DIMENSIONAL CASCADES: SOLIDITY, s/c =1.0
CAMBER, θ =30.0
β₂=62.8
β₂=52.6
β₂=42.8
X = SOLID BODY ROTOR, f =.735
θ = 30°; β₀= 59.0°
s/c= .95
EXIT ANGLE
ENTRANCE ANGLE
NOTE: DASHED LINE INDICATES ANGLES BELOW WHICH TWO DIMENSIONAL TESTS SHOW HIGH LOSSES
β₀ = STAGGER ANGLE

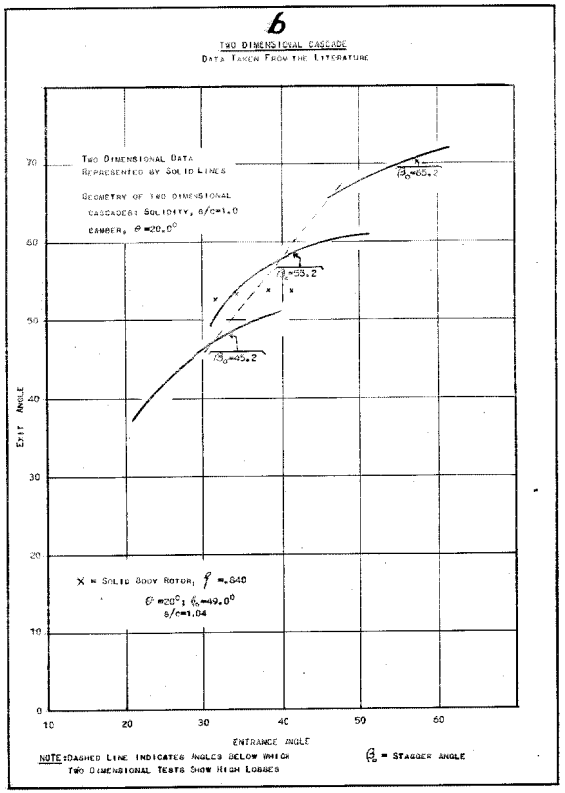
b
TWO DIMENSIONAL CASCADE
DATA TAKEN FROM THE LITERATURE
TWO DIMENSIONAL DATA REPRESENTED BY SOLID LINES
GEOMETRY OF TWO DIMENSIONAL CASCADES: SOLIDITY, s/c=1.0
CAMBER, θ =20.0°
β₂=65.2
β₂=55.2
β₂=45.2
X = SOLID BODY ROTOR, f =.640
θ =20°; β₀=49.0°
s/c=1.04
EXIT ANGLE
ENTRANCE ANGLE
NOTE: DASHED LINE INDICATES ANGLES BELOW WHICH TWO DIMENSIONAL TESTS SHOW HIGH LOSSES
β₀ = STAGGER ANGLE

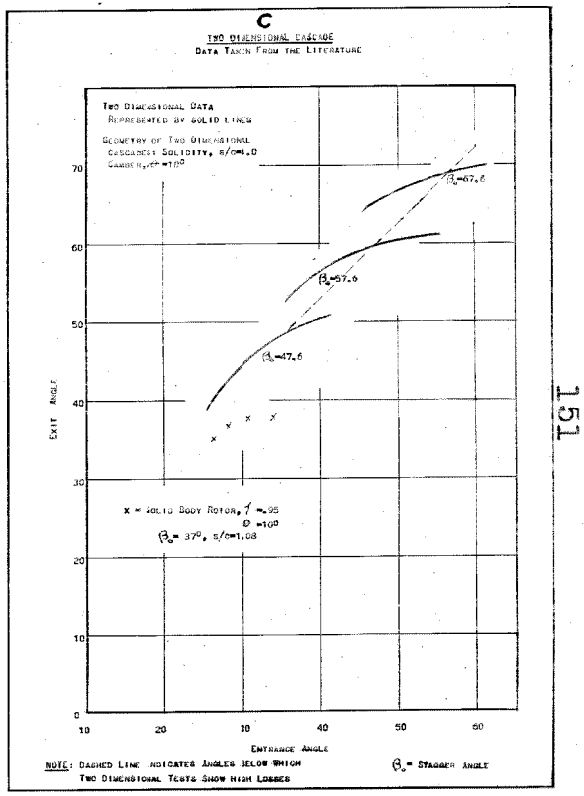
c
TWO DIMENSIONAL CASCADE
DATA TAKEN FROM THE LITERATURE
TWO DIMENSIONAL DATA REPRESENTED BY SOLID LINES
GEOMETRY OF TWO DIMENSIONAL CASCADES: SOLIDITY, s/c=1.0
β₂=67.6
β₂=57.6
β₂=47.6
X = SOLID BODY ROTOR, f =.95
θ =10°
β₀= 37°, s/c=1.08
EXIT ANGLE
ENTRANCE ANGLE
NOTE: DASHED LINE INDICATES ANGLES BELOW WHICH TWO DIMENSIONAL TESTS SHOW HIGH LOSSES
β₀ = STAGGER ANGLE

FIG. 80

SOLID BODY - ENTRANCE VANES

LEAVING ANGLE VS. RADIUS

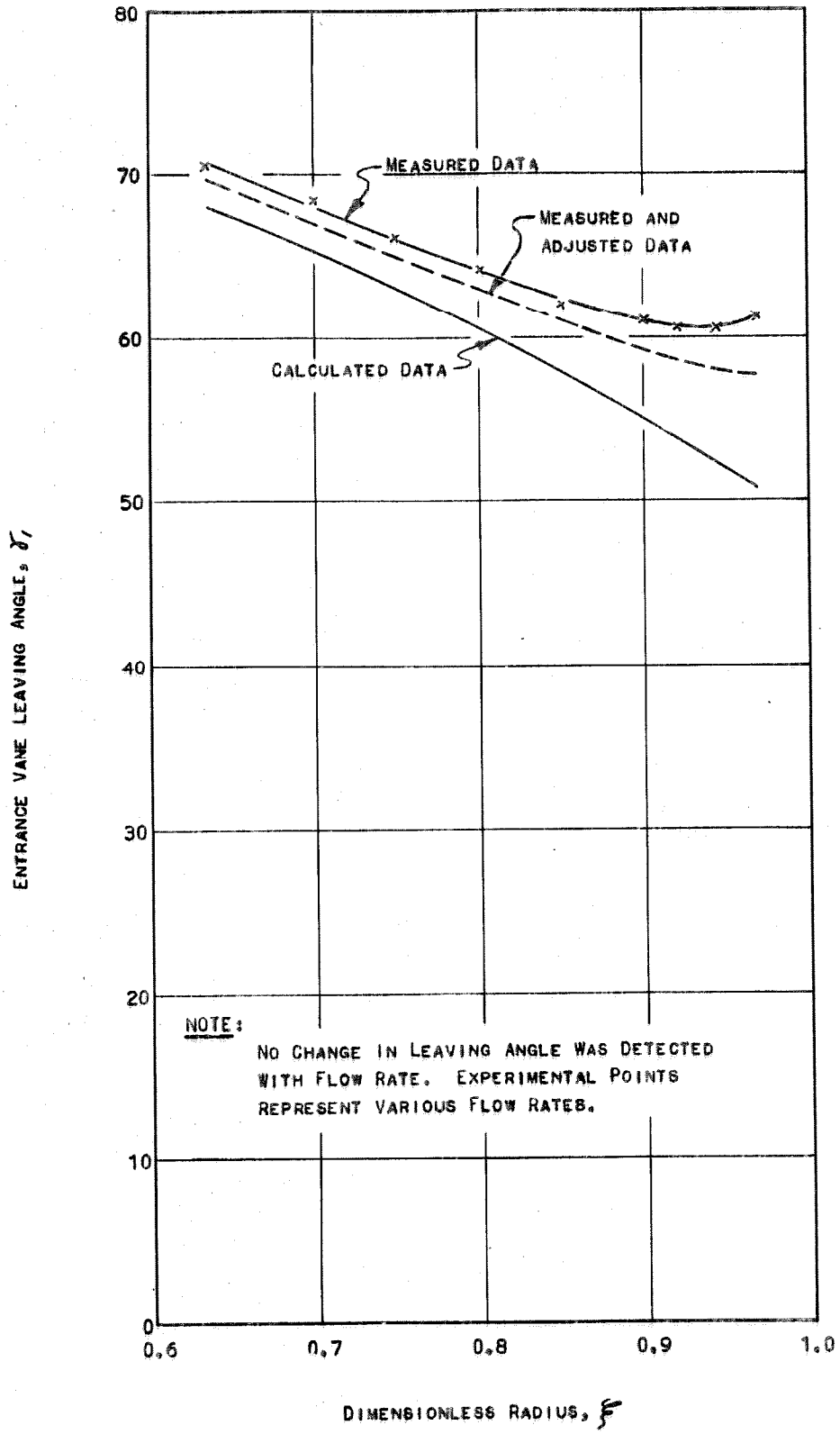

FIG. 81

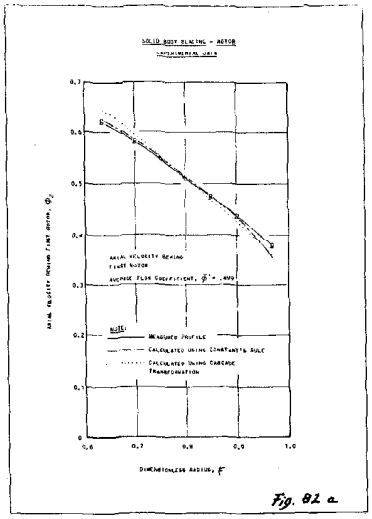

Fig. 82 a

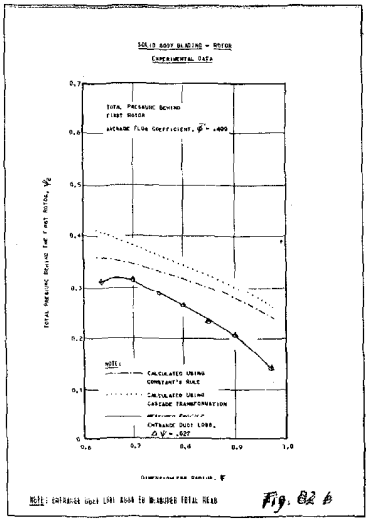

Fig. 82 b

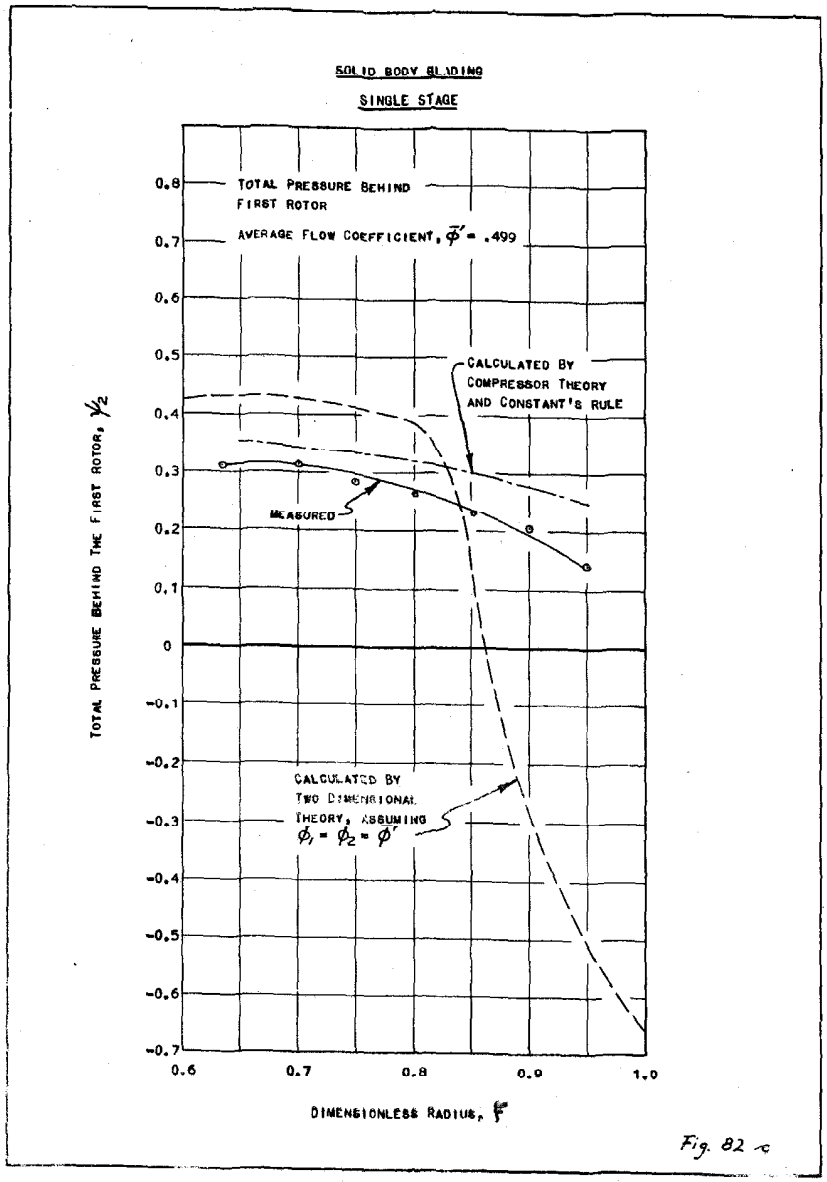

Fig. 82 c

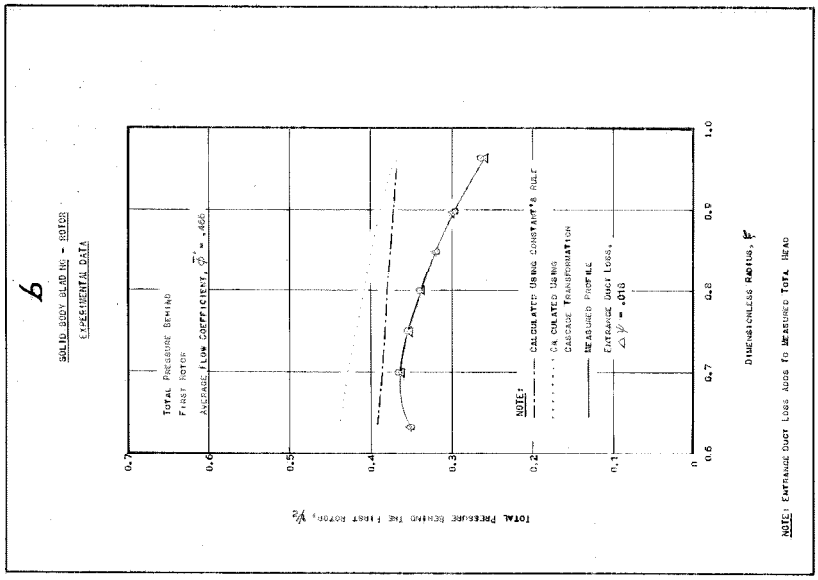
b
SOLID BODY BLADING - ROTOR
EXPERIMENTAL DATA
TOTAL PRESSURE BEHIND
FIRST ROTOR
AVERAGE FLOW COEFFICIENT, $\bar{\phi}$ = .466
TOTAL PRESSURE BEHIND THE FIRST ROTOR, $\bar{\psi}_2$
NOTE:
CALCULATED USING CONSTANT'S RULE
CALCULATED USING
CASCADE TRANSFORMATION
MEASURED PROFILE
ENTRANCE DUCT LOSS,
$\Delta\bar{\psi}$ = .010
DIMENSIONLESS RADIUS, $\bar{r}$
NOTE: ENTRANCE DUCT LOSS ADDED TO MEASURED TOTAL HEAD

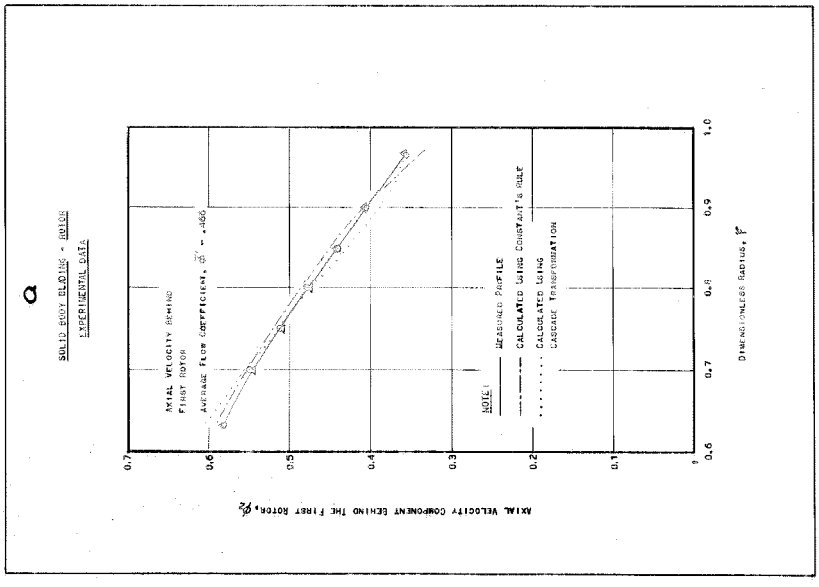
a
SOLID BODY BLADING - ROTOR
EXPERIMENTAL DATA
AXIAL VELOCITY BEHIND
FIRST ROTOR
AVERAGE FLOW COEFFICIENT, $\bar{\phi}$ = .466
AXIAL VELOCITY COMPONENT BEHIND THE FIRST ROTOR, $\bar{\phi}_2$
NOTE:
MEASURED PROFILE
CALCULATED USING CONSTANT'S RULE
CALCULATED USING
CASCADE TRANSFORMATION
DIMENSIONLESS RADIUS, $\bar{r}$

FIG. 83

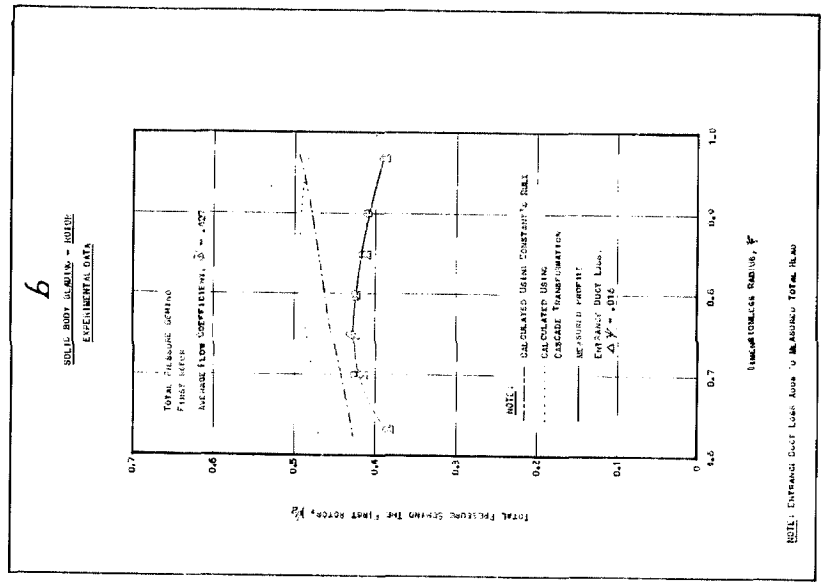
b
SOLID BODY BLADING - ROTOR
EXPERIMENTAL DATA
TOTAL PRESSURE BEHIND THE FIRST ROTOR, $\bar{p}_2$
DIMENSIONLESS RADIUS, $\bar{r}$
NOTE: ENTRANCE DUCT LOSS ADDED TO MEASURED TOTAL HEAD
a
SOLID BODY BLADING - ROTOR
EXPERIMENTAL DATA
AXIAL VELOCITY COMPONENT BEHIND THE FIRST ROTOR, $\bar{c}_{z_2}$
DIMENSIONLESS RADIUS, $\bar{r}$

FIG. 84

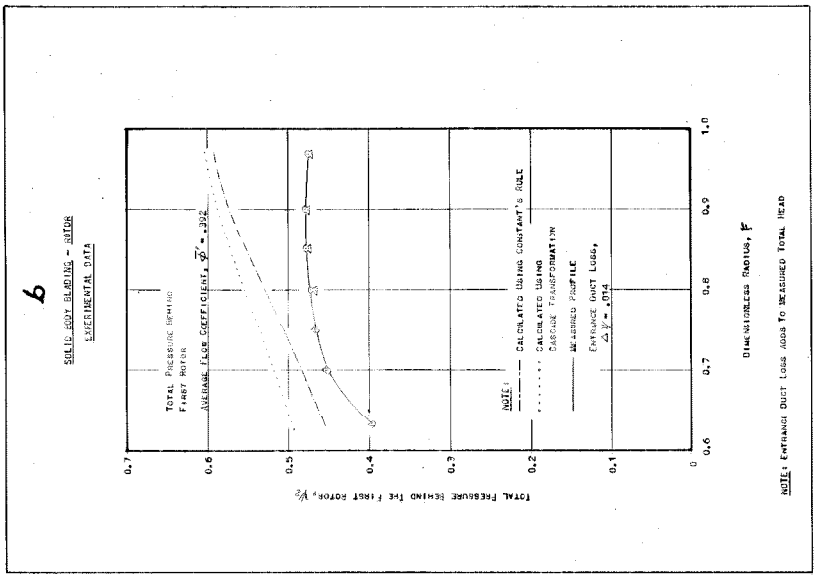
b
SOLID BODY BLADING - ROTOR
EXPERIMENTAL DATA
TOTAL PRESSURE BEHIND FIRST ROTOR
AVERAGE FLOW COEFFICIENT, $\bar{\phi} = .392$
NOTE:
CALCULATED USING CONSTANT'S RULE
CALCULATED USING CASCADE TRANSFORMATION
MEASURED PROFILE
ENTRANCE DUCT LOSS, $\Delta \bar{y} = .014$
TOTAL PRESSURE BEHIND THE FIRST ROTOR, $\bar{y}_2$
DIMENSIONLESS RADIUS, $\bar{r}$
NOTE: ENTRANCE DUCT LOSS ADDED TO MEASURED TOTAL HEAD

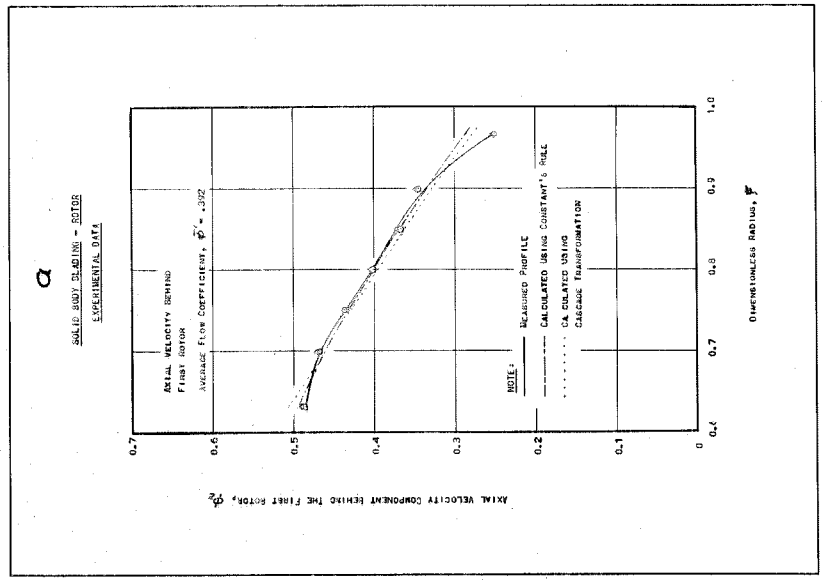
a
SOLID BODY BLADING - ROTOR
EXPERIMENTAL DATA
AXIAL VELOCITY BEHIND
FIRST ROTOR
AVERAGE FLOW COEFFICIENT, $\bar{\phi} = .392$
NOTE:
MEASURED PROFILE
CALCULATED USING CONSTANT'S RULE
CALCULATED USING CASCADE TRANSFORMATION
AXIAL VELOCITY COMPONENT BEHIND THE FIRST ROTOR, $\bar{\phi}_2$
DIMENSIONLESS RADIUS, $\bar{r}$

FIG. 85

a

SUMMARY GRAPH

AXIAL VELOCITY COMPONENT BEHIND FIRST ROTOR

SOLID BODY BLADING

(CALCULATED DATA - CONSTANT'S RULE)

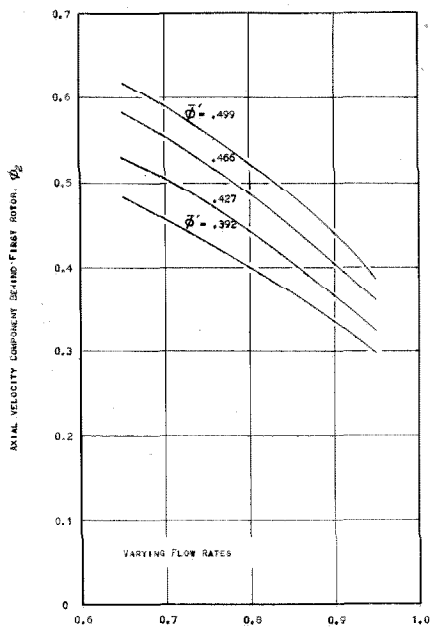

b

SUMMARY GRAPH

AXIAL VELOCITY COMPONENT BEHIND FIRST ROTOR

SOLID BODY BLADING

(MEASURED DATA)

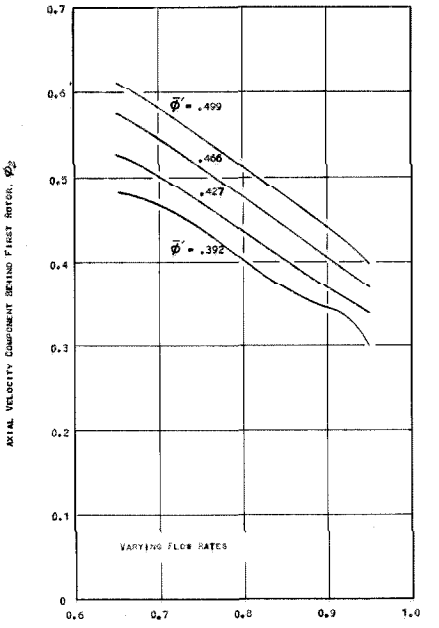

c

SUMMARY GRAPH

TOTAL PRESSURE BEHIND FIRST ROTOR

SOLID BODY BLADING

(CALCULATED DATA - CONSTANT'S RULE)

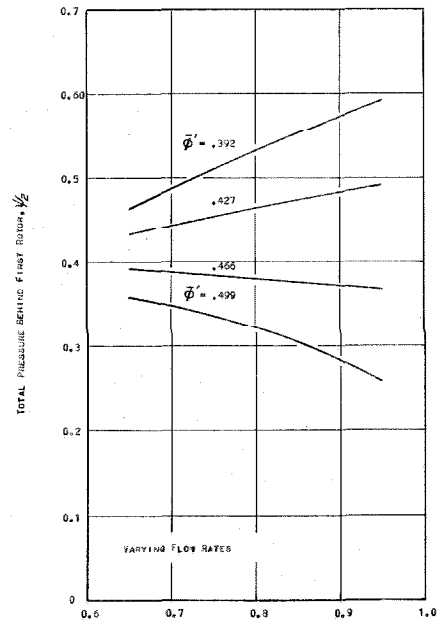

d

SUMMARY GRAPH

TOTAL PRESSURE BEHIND FIRST ROTOR

SOLID BODY BLADING

(MEASURED DATA)

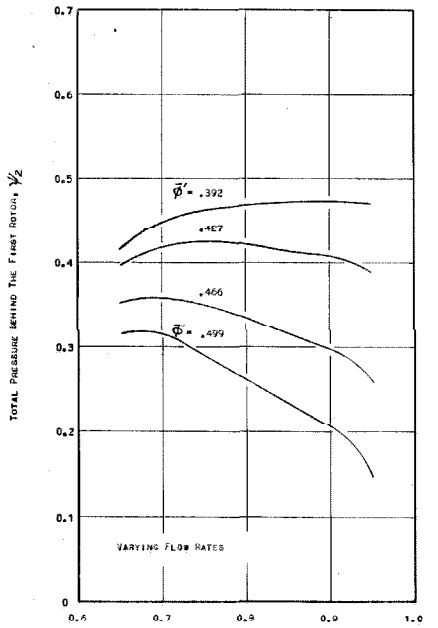

NOTE: ENTRANCE DUCT LOSS TO BE ADDED

FIG. 86

Fig. 87

FREE VORTEX BLADING - OVERALL PERFORMANCE

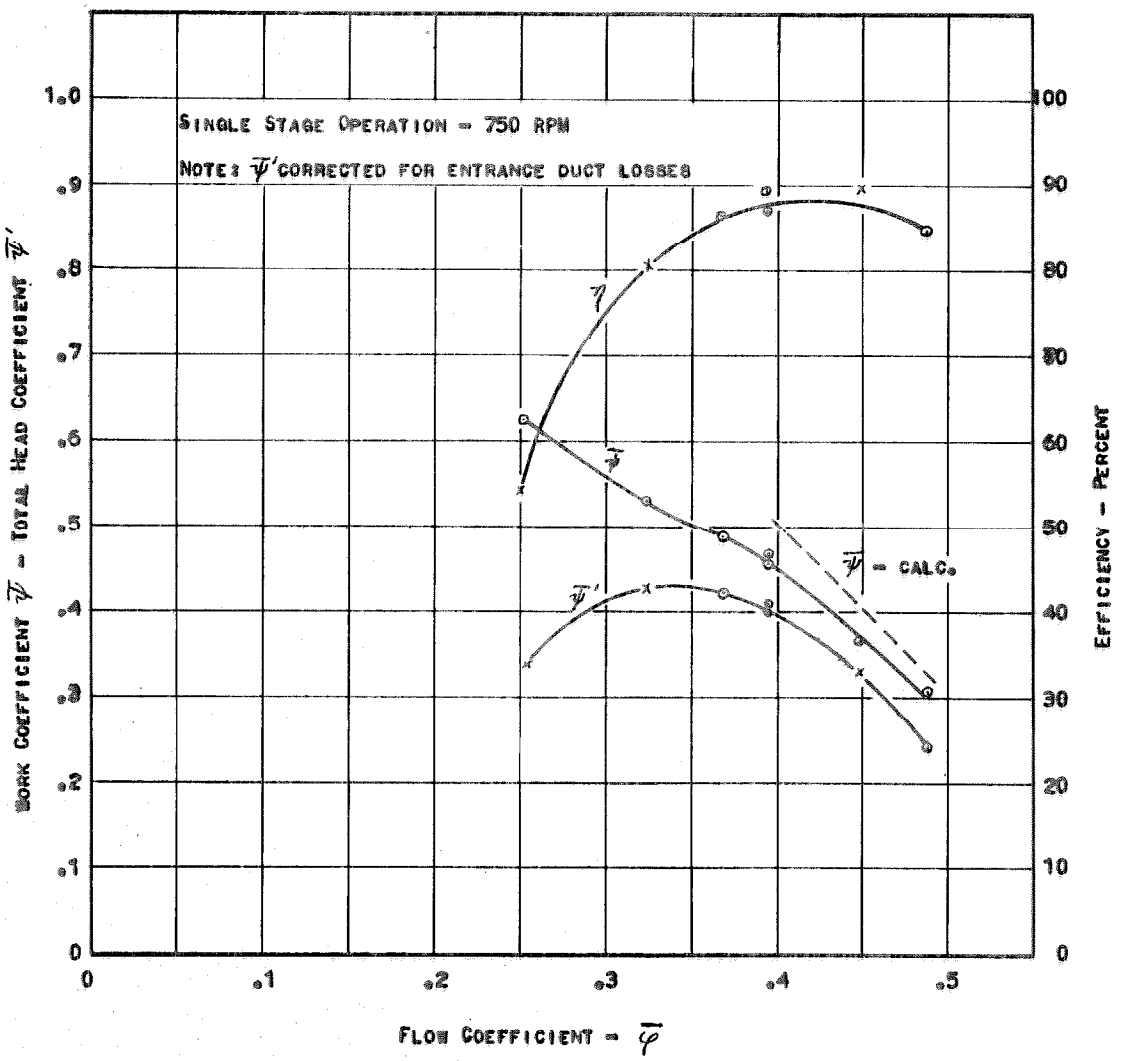

SOLID BODY BLADING - OVERALL PERFORMANCE

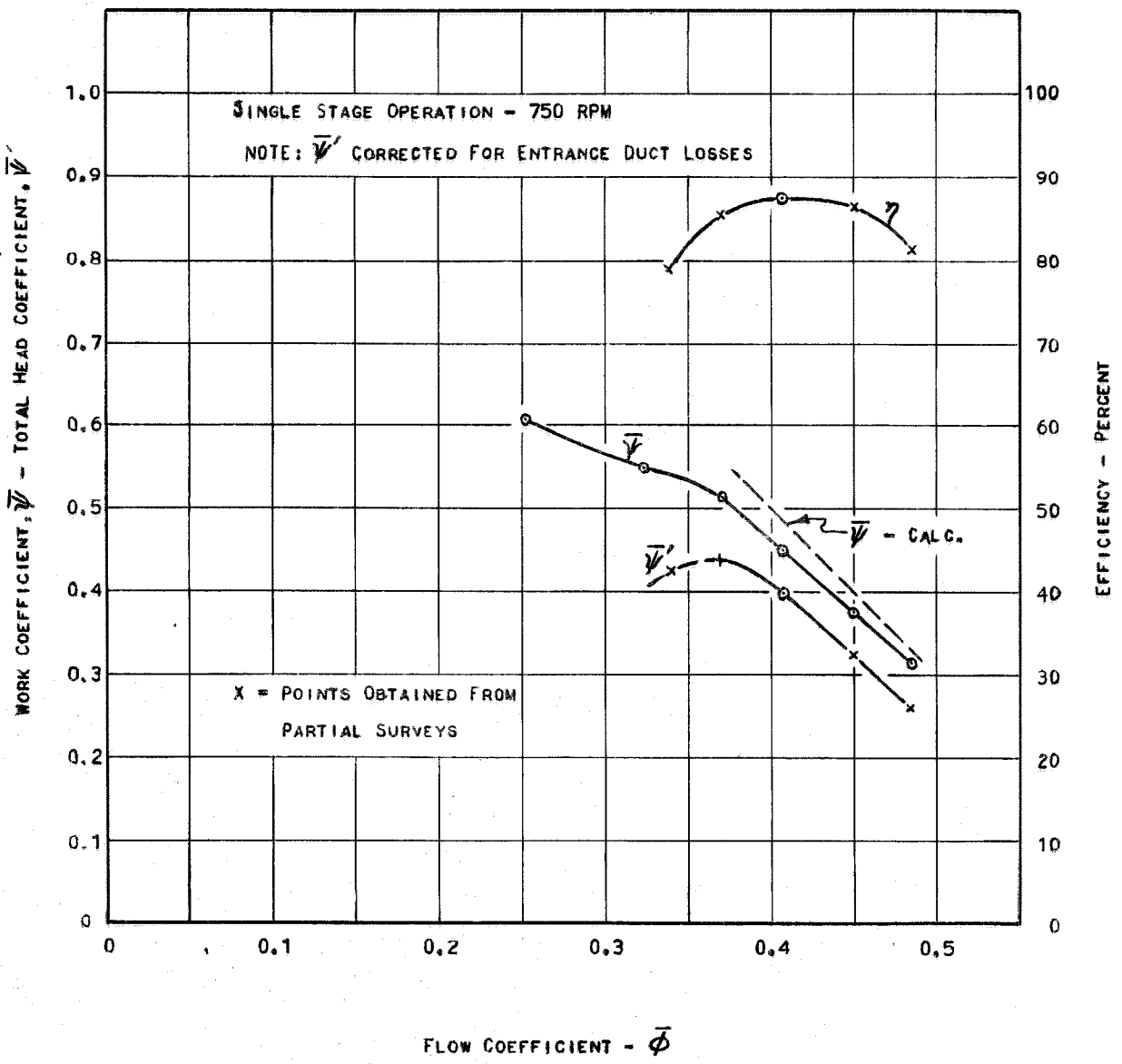

FIG. 88

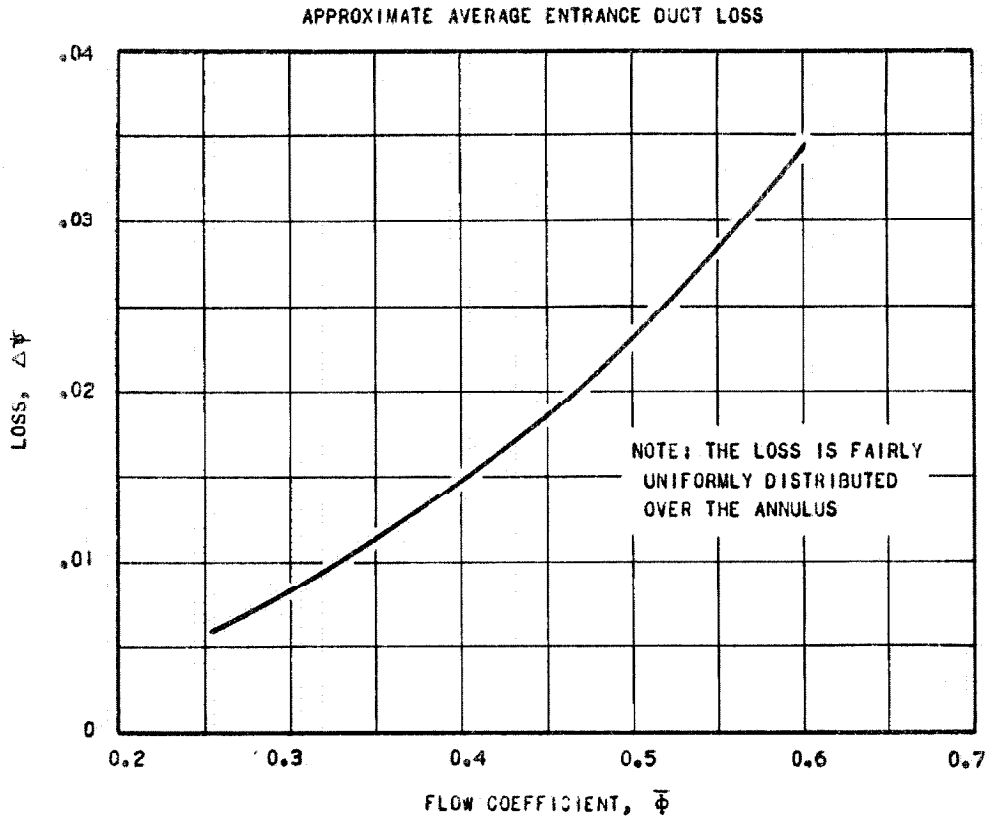
APPROXIMATE AVERAGE ENTRANCE DUCT LOSS
.04
.03
.02
.01
0
LOSS, Δψ
0.2
0.3
0.4
0.5
0.6
0.7
FLOW COEFFICIENT, Φ
NOTE: THE LOSS IS FAIRLY UNIFORMLY DISTRIBUTED OVER THE ANNULUS

FIG. 89

Fig. 90

MAXIMUM COMPRESSOR EFFICIENCY vs. REYNOLDS NUMBER

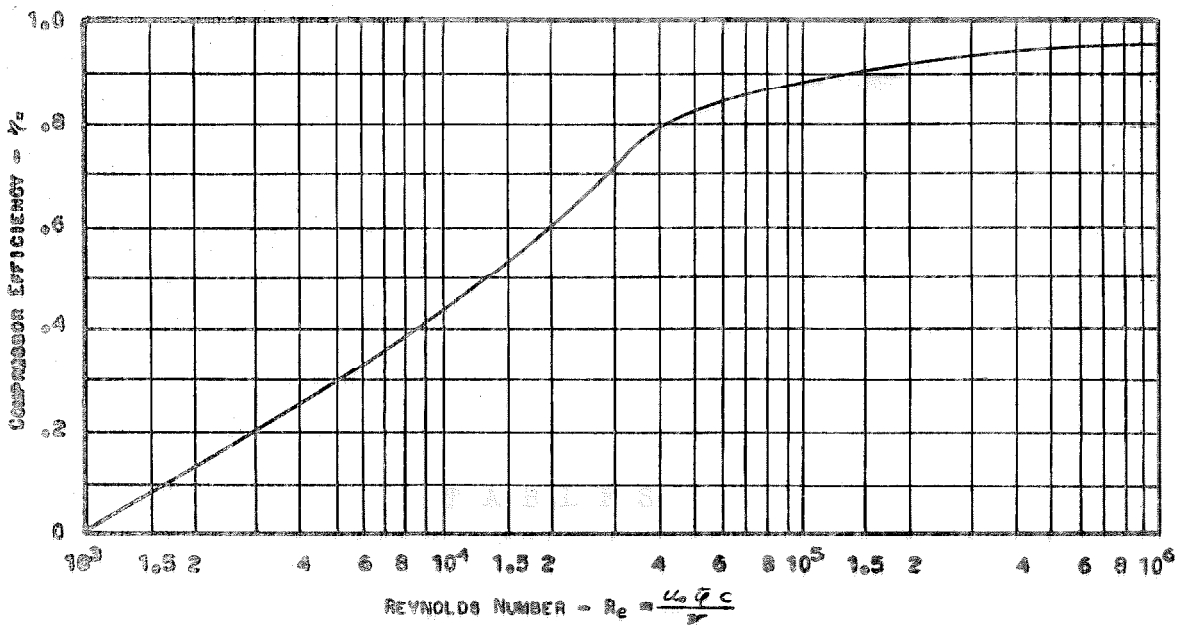

NOTE: CURVE SHOWN IS ENVELOPE OF A NUMBER OF EFFICIENCY CURVES. REPRODUCED FROM ECKERT'S REPORT (REF. 32)

T A B L E S

TABLE I

ELECTRICAL SPECIFICATIONS

DYNAMOMETER

ELECTRIC PRODUCTS CO., D.C. MOTOR (REBUILT), TYPE 1-7264, STABILIZED SHUNT WOUND, 250 VOLTS, 450 AMPS., MAX. SPEED 2000 R.P.M.

MOTOR GENERATOR SET

DRIVING MOTOR: ELECTRIC MACHINERY MFG. CO., SYNCHRONOUS MOTOR, SERIAL NO. 83382, THREE PHASE, 60 CYCLES, 125 H.P., 2400 VOLTS, 32 AMPS., SPEED 1200 R.P.M.

GENERATORS (2): TROY ENGINE AND MACHINE CO., DIRECT CURRENT GENERATOR (REBUILT), COMPOUND WOUND, 60 K.W., 120 VOLTS, 500 AMPS., SPEED 1200 R.P.M.

TABLE 2

AIRFOIL CALCULATIONS:

STATOR BLADE SECTION III

(ζ =.80)

PARABOLIC CAMBER LINE:

$\theta/2 = 14^\circ 59'$

TAN $\theta/2$ = .26764

c = 2.600 INCHES

TAN $\phi = \frac{dy_c}{dx}$

MAXIMUM THICKNESS = 10% CHORD

$\frac{x}{c}$	$1 - \frac{2x}{c}$	TAN ϕ	SIN ϕ	COS ϕ	$\frac{y_T}{c}$	$\frac{y_T}{c}$ SIN ϕ (3)	$\frac{y_T}{c}$ COS ϕ (4)	$1 - \frac{x}{c}$	$\frac{x}{c}\left(1 - \frac{x}{c}\right)$	$\frac{y_c}{c}$ (2)
0	1	.26764	.25854	.96600	0	0	0	1	0	0
.0050	.9900	.26496	.25601	.96667	.00850	.00218	.00822	.9950	.00498	.00133
.0100	.9800	.26229	.25376	.96727	.01222	.00310	.01182	.9900	.00990	.00265
.0200	.9600	.25693	.24897	.96851	.01667	.00415	.01615	.9800	.01960	.00524
.0300	.9400	.25158	.24390	.96980	.02084	.00508	.02021	.9700	.02910	.00779
.0400	.9200	.24623	.23910	.97100	.02317	.00554	.02250	.9600	.03400	.00910
.0500	.9000	.24088	.23429	.97217	.02542	.00596	.02471	.9500	.04750	.01271
.0600	.8800	.23552	.22920	.97338	.02772	.00635	.02698	.9400	.05640	.01509
.0700	.8600	.23017	.22438	.97450	.02970	.00666	.02894	.9300	.06510	.01742
.0800	.8400	.22482	.21928	.97566	.03147	.00690	.03070	.9200	.07360	.01970
.0900	.8200	.21946	.21445	.97673	.03311	.00710	.03234	.9100	.08190	.02192
.1000	.8000	.21411	.20933	.97784	.03463	.00725	.03386	.9000	.09000	.02409
.1500	.7000	.18735	.18424	.98288	.04044	.00745	.03975	.8500	.12750	.03412
.2000	.6000	.16058	.15845	.98737	.04460	.00707	.04404	.8000	.16000	.04282
.2500	.5000	.13382	.13354	.99118	.04744	.00634	.04702	.7500	.18750	.05018
.3000	.4000	.10706	.10655	.99431	.04938	.00526	.04910	.7000	.21000	.05620
.3500	.3000	.08029	.07991	.99680	.05000	.00400	.04984	.6500	.22750	.06089
.4000	.2000	.05353	.05346	.99857	.04937	.00264	.04930	.6000	.24000	.06423
.4500	.1000	.02676	.02675	.99964	.04784	.00128	.04782	.5500	.24750	.06624
.5000	0	0	0	1.00000	.04516	0	.04516	.5000	.25000	.06691
.5500	- .1000	-.02676	-.02675	.99964	.04148	-.00111	.04147	.4500	.24750	.06624
.6000	- .2000	-.05353	-.05346	.99857	.03712	-.00198	.03707	.4000	.24000	.06423
.6500	- .3000	-.08029	-.07991	.99680	.03222	-.00251	.03212	.3500	.22750	.06089
.7000	- .4000	-.10706	-.10655	.99431	.02687	-.00286	.02672	.3000	.21000	.05620
.7500	- .5000	-.13382	-.13354	.99118	.02109	-.00282	.02090	.2500	.18750	.05018
.8000	- .6000	-.16058	-.15845	.98737	.01600	-.00254	.01580	.2000	.16000	.04280
.8500	- .7000	-.18735	-.18424	.98288	.01140	-.00210	.01120	.1500	.12750	.03412
.9000	- .8000	-.21411	-.20933	.97784	.00719	-.00151	.00703	.1000	.09000	.02409
.9500	- .9000	-.24088	-.23429	.97217	.00372	-.00087	.00362	.0500	.04750	.01271
1.0000	-1.0000	-.26764	-.25854	.96600	.00111	-.00029	.00107	0	0	0

TABLE 2 (CONT)

(1)		(1)-(3)	(2)+(4)	(1)+(3)	(2)-(4)					
$\frac{X}{C}$	Y_C INCHES	$\frac{X_U}{C}$	$\frac{Y_U}{C}$	$\frac{X_\ell}{C}$	$\frac{Y_\ell}{C}$	X_U INCHES	Y_U INCHES	X_ℓ INCHES	Y_ℓ INCHES	X INCHES
0	0	0	0	0	0	0	0	0	0	0
.0050	.00346	.00282	.00955	.00718	-.00689	.00733	.02483	.01867	-.01791	.01300
.0100	.00689	.00690	.01447	.01310	-.00917	.01794	.03762	.03406	-.02384	.02600
.0200	.01362	.01585	.02139	.02415	-.01091	.04121	.05561	.06279	-.02837	.05200
.0300	.02025	.02492	.02800	.03508	-.01242	.06479	.07280	.09121	-.03229	.07800
.0400	.02366	.03446	.03160	.04554	-.01340	.08960	.08216	.11840	-.03484	.10400
.0500	.03305	.04404	.03742	.05596	-.01200	.11450	.09729	.14550	-.03120	.13000
.0600	.03923	.05365	.04159	.06635	-.01189	.13949	.10813	.17251	-.03091	.15600
.0700	.04529	.06334	.04636	.07666	-.01152	.16468	.12054	.19932	-.02995	.18200
.0800	.05122	.07310	.05040	.08690	-.01100	.19006	.13104	.22594	-.02860	.20800
.0900	.05699	.08290	.05426	.09710	-.01042	.21554	.14108	.25246	-.02709	.23400
.1000	.06263	.09275	.05795	.10725	-.00977	.24115	.15067	.27885	-.02540	.26000
.1500	.08871	.14255	.07387	.15745	-.00563	.37063	.19206	.40937	-.01464	.39000
.2000	.11133	.19293	.08686	.20707	-.00122	.50162	.22584	.53838	-.00317	.52000
.2500	.13047	.24366	.09720	.25634	.00316	.63352	.25272	.66648	.00822	.65000
.3000	.14612	.29474	.10530	.30526	.00710	.76632	.27378	.79368	.01846	.78000
.3500	.15831	.34600	.11073	.35400	.01105	.89960	.28790	.92040	.02873	.91000
.4000	.16700	.39736	.11353	.40264	.01493	1.03314	.29518	1.04686	.03882	1.04000
.4500	.17222	.44872	.11406	.45128	.01842	1.16667	.29656	1.17333	.04789	1.17000
.5000	.17397	.50000	.11207	.50000	.02175	1.30000	.29138	1.30000	.05655	1.30000
.5500	.17222	.55111	.10771	.54889	.02477	1.43289	.28095	1.42711	.06440	1.43000
.6000	.16700	.60198	.10130	.59802	.02716	1.56515	.26338	1.55485	.07062	1.56000
.6500	.15831	.65257	.09301	.64743	.02877	1.69668	.24183	1.68332	.07480	1.69000
.7000	.14612	.70286	.08292	.69714	.02948	1.82744	.21559	1.81256	.07665	1.82000
.7500	.13047	.75282	.07108	.74718	.02928	1.95739	.18481	1.94267	.07613	1.95000
.8000	.11133	.80254	.05860	.79746	.02700	2.08660	.15236	2.07340	.07020	2.08000
.8500	.08871	.85210	.04532	.84790	.02292	2.21546	.11783	2.20454	.05959	2.21000
.9000	.06263	.90151	.03112	.89849	.01706	2.34393	.08091	2.33607	.04436	2.34000
.9500	.03305	.95087	.01633	.94913	.00909	2.47226	.04246	2.46774	.02363	2.47000
1.0000	0	1.00029	.00107	.99971	-.00107	2.60075	.00278	2.59925	-.00278	2.60000

TABLE 3

COMPARISON OF FLOW RATE MEASUREMENTS

THE FOLLOWING DATA GIVE A COMPARISON BETWEEN THE FLOW COEFFICIENT DETERMINED FROM ENTRANCE DUCT MEASUREMENTS, AND FROM COMPLETE SURVEYS BEHIND THE BLADE ROWS. THE CLOSE AGREEMENT AND THE RANDOM SCATTER GIVE A CHECK ON THE ACCURACY OF THE SURVEY MEASUREMENTS AND INDICATE THAT THERE IS NO SYSTEMATIC ERROR DUE TO WAKE FLUCTUATIONS.

STATION	$\bar{\phi}_w$ FLOW COEFF. FROM ENTR. DUCT	$\bar{\phi}_s$ FLOW COEFF. FROM SURVEYS	$\frac{\bar{\phi}_w}{\bar{\phi}_s}$
BEHIND 1ST STATOR	.393	.392	1.003
BEHIND 1ST STATOR	.366	.382	.958
BEHIND 1ST STATOR	.487	.492	.990
BEHIND 1ST ROTOR	.394	.399	.987
BEHIND 1ST ROTOR	.392	.387	1.013

TABLE 4

CHARACTERISTICS OF VARIOUS BLADE TYPES*

		BLADE TYPE				
RADIAL POSITION ξ		$\frac{\alpha}{\xi^2}$	$\frac{\alpha}{\xi}$	α	$\alpha\xi$	$\alpha\xi^2$
RELATIVE VELOCITY (ROTOR)	0.6	0.40	0.51	0.61	0.65	0.72
	0.8	0.70	0.70	0.70	0.71	0.72
	1.0	0.96	0.91	0.84	0.76	0.69
RELATIVE VELOCITY (STATOR)	0.6	0.88	0.84	0.81	0.81	0.80
	0.8	0.70	0.69	0.69	0.69	0.70
	1.0	0.63	0.61	0.60	0.61	0.61
ROTOR CHORD TWIST		64.3	48.0	41.2	38.7	42.0
STATOR CHORD TWIST		-33.1	-13.2	4.1	21.7	37.6
AIR TURNING ANGLE (ROTOR)	0.6	51.8	39.9	33.3	30.8	29.2
	0.8	17.9	17.9	17.9	18.2	18.1
	1.0	8.3	9.1	6.2	2.5	-8.5
AIR TURNING ANGLE (STATOR)	0.6	15.7	18.1	19.9	20.4	21.9
	0.8	17.8	17.9	17.9	18.5	17.4
	1.0	17.9	17.9	17.7	19.6	24.4
(P) PERCENT REACTION	0.6	-0.008	0.113	0.175	0.163	0.200
	0.8	0.503	0.500	0.500	0.485	0.472
	1.0	0.685	0.680	0.693	0.693	0.690
CAVITATION COEFFICIENT	0.6	1.03	1.19	1.27	1.32	1.42
	0.8	0.79	1.18	1.19	1.21	1.25
	1.0	1.91	1.79	1.66	1.51	1.33

ALL ANGLES GIVEN IN DEGREES. ALL VELOCITIES GIVEN IN TERMS OF TIP SPEED.

*) TANGENTIAL VELOCITY IN FRONT OF ROTOR MIDSECTION (λ_1) WAS TAKEN EQUAL FOR ALL TYPES EXCEPT FOR A SLIGHT CHANGE FOR THE TYPE "$\alpha\xi^2$".

TABLE 5

TABULATION OF BLADE TYPES IN ORDER

OF THEIR SUITABILITY FOR VARIOUS CRITERIA

RELATIVE VELOCITY		BLADE TWIST		AIR TURNING		PERCENT REACTION		CAVITATION COEFFICIENT	
MAGNITUDE	BLADE TYPE	MAGNITUDE	BLADE TYPE	MAGNITUDE	BLADE TYPE	MAGNITUDE	BLADE TYPE	MAGNITUDE	BLADE TYPE
		[21]	[.50/ξ]			[0.28]	[.145/ξ]		
		[30]	[.20 ξ]			[0.30]	[.20 ξ]		
0.80	$\alpha\xi^a$	39	$\alpha\xi$	29	$\alpha\xi^2$	-0.30	$\alpha\xi^2$	1.42	$\alpha\xi^3$
[0.81]	[.34 ξ]			[30]	[.34 ξ]			[1.42]	[.40 ξ]
0.91	$\alpha\xi$	41	α	31	$\alpha\xi$	-0.32	α	1.51	$\alpha\xi$
0.84	α	42	$\alpha\xi^2$	33	α	-0.34	$\alpha\xi$	1.55	α
[0.90]	[.90/ξ]			[35]	[.65/ξ]			[1.70]	[.305/ξ]
0.91	α/ξ	48	α/ξ	40	α/ξ	-0.39	α/ξ	1.79	α/ξ
0.95	α/ξ^2	54	α/ξ^2	52	α/ξ^2	-0.51	α/ξ^4	1.91	α/ξ^3

a) THE FIGURE USED HERE IS EQUAL TO (P = .50). SMALL ABSOLUTE VALUES INDICATE FAVORABLE RATIOS.

ALL ANGLES GIVEN IN DEGREES. ALL VELOCITIES GIVEN IN TERMS OF TIP SPEED.

QUANTITIES IN BRACKETS ARE OPTIMA FOR THE "FREE VORTEX" AND "SOLID BODY" BLADING RESPECTIVELY, INDEPENDENT OF LOCATION OF 50% REACTION POINT.

TABLE 6

CHARACTERISTICS OF FREE VORTEX BLADING

WITH VARIOUS LOCATIONS OF THE 50% REACTION POINT

		RADIAL POSITION OF 50% REACTION POINT				
	RADIAL POSITION $\frac{r}{R}$	0.50 (α = .025)	0.65 (α = .111)	0.70 (α = .145)	0.80 (α = .220)	0.90 (α = .305)
RELATIVE VELOCITY (ROTOR)	0.6	0.71	0.61	0.59	0.50	0.54
	0.8	0.90	0.81	0.775	0.70	0.63
	1.0	1.09	1.00	0.96	0.90	0.84
RELATIVE VELOCITY (STATOR)	0.6	0.60	0.70	0.75	0.84	0.98
	0.8	0.54	0.59	0.67	0.68	0.78
	1.0	0.50	0.55	0.55	0.63	0.69
ROTOR CHORD TWIST		21	33	38	49	63
STATOR CHORD TWIST		9	14	11	13	15
AIR TURNING ANGLE (ROTOR)	0.6	25	35	37	40	41
	1.0	5	6	7	9	11
AIR TURNING ANGLE (STATOR)	0.6	35	27	24	18	13
	1.0	23	21	19	17	16
PERCENT REACTION	0.6	0.65	0.42	0.32	0.11	-0.12
	0.8	0.81	0.67	0.62	0.50	0.37
	1.0	0.88	0.79	0.76	0.68	0.60
CAVITATION COEFF.	0.6	1.46	1.11	1.10	1.14	2.22
	0.8	1.42	1.29	1.25	1.15	1.29
	1.0	2.10	1.95	1.90	1.70	2.75

ALL ANGLES GIVEN IN DEGREES. ALL VELOCITIES GIVEN IN TERMS OF TIP SPEED.

TABLE 7

CHARACTERISTICS OF SOLID BODY BLADING WITH VARIOUS LOCATIONS OF THE 50% REACTION POINT

		RADIAL POSITION OF 50% REACTION POINT					
	RADIAL POSITION ξ	0.45 $\alpha = 0$	0.55 $\alpha = .10$	0.67 $\alpha = .20$	0.80 $\alpha = .325$	0.82 $\alpha = .344$	0.90 $\alpha = .40$
RELATIVE VELOCITY (ROTOR)	0.6	0.75	0.71	0.69		0.65	0.67
	0.8	0.94	0.85	0.79		0.71	0.68
	1.0	1.10	1.00	0.91		0.76	0.71
RELATIVE VELOCITY (STATOR)	0.6	0.55	0.62	0.70		0.81	0.90
	0.8	0.51	0.55	0.62		0.69	0.75
	1.0	0.50	0.47	0.55		0.61	0.65
ROTOR CHORD TWIST		22	28	30		40	43
STATOR CHORD TWIST		- 8	3	9		22	25
AIR TURNING ANGLE (ROTOR)	0.6	21	25	31		30	33
	0.8						
	1.0	5	2	3		3	4
AIR TURNING ANGLE (STATOR)	0.6	37	31	27		20	17
	0.8						
	1.0	23	26	23		20	24
PERCENT REACTION	0.6	0.72	0.58	0.42	0.19	0.16	-0.12
	0.8	0.84	0.75	0.64	0.50	0.49	0.40
	1.0	0.90	0.86	0.80	0.70	0.69	0.60
CAVITATION COEFF.	0.6		1.13	1.25	1.30	1.32	0.81
	0.8		1.36	1.28	1.21	1.21	0.74
	1.0		2.33	1.79	1.55	1.51	1.47

ALL ANGLES GIVEN IN DEGREES. ALL VELOCITIES GIVEN IN TERMS OF TIP SPEED.

TABLE 8

VORTEX ROTOR BLADE ANGLE CALCULATIONS

ASSUMPTIONS: $\xi_{hub} = 0.60000$, $\bar{w}_a = 0.40000$, $\bar{v}_a = 0.45000$, $\xi_1 = 0.70000$, $C_o = 0.98000$, $\frac{1}{\xi_2} = 2.2222$, $\frac{C_o - \bar{v}_a}{A} = 0.14500$, $\frac{C_o + \bar{v}_a}{A} = 0.34500$, $\frac{2D}{N} = \frac{2\pi 36}{30} = 3.7700$

SECTION	VIII	VII	VI	V	IV	III	II	I
ξ	0.60000	0.62000	0.65000	0.70000	0.75000	0.80000	0.90000	1.00000
$1/\xi$	1.6666	1.6129	1.5385	1.4286	1.3333	1.2500	1.1111	1.00000
λ_1	0.24167	0.23387	0.22380	0.20715	0.19333	0.18125	0.16111	0.14500
λ_2	0.57498	0.55645	0.53078	0.49287	0.45999	0.43125	0.38333	0.34500
$\xi - \lambda_1$	0.35833	0.38613	0.42720	0.49285	0.55667	0.61875	0.73889	0.85500
$\xi - \lambda_2$	0.02502	0.06355	0.11922	0.20713	0.29001	0.36875	0.51667	0.65500
cot β_1	0.79628	0.85806	0.94932	1.09521	1.23703	1.37497	1.64196	1.89998
cot β_2	0.05559	0.14122	0.26493	0.46028	0.64446	0.81944	1.14614	1.45554
c	2.60000	2.60000	2.60000	2.60000	2.60000	2.60000	2.60000	2.60000
s	2.26194	2.33734	2.45044	2.63893	2.82743	3.01592	3.39291	3.7699
s/c	0.86998	0.89898	0.94248	1.01497	1.08747	1.15997	1.30497	1.4500
$\sqrt{s/c}$	0.933	0.949	0.971	1.007	1.043	1.077	1.142	1.204
$0.26\sqrt{s/c}$	0.24258	0.24674	0.25246	0.26182	0.27118	0.28002	0.29692	0.31304
(EXIT) β_2	86° 49'	81° 58'	75° 10'	65° 17'	57° 12'	50° 40'	41° 3'	34° 29'
(ENTRANCE) β_1	51° 21'	49° 22'	46° 29'	42° 24'	38° 57'	36° 2'	31° 21'	27° 45'
$\theta°$	35° 28'	32° 36'	28° 41'	22° 53'	18° 15'	14° 38'	9° 42'	6° 44'
$1 - 0.26\sqrt{s/c}$	0.75742	0.75326	0.74754	0.73818	0.72882	0.71998	0.70308	0.68696
θ	46° 40'	43° 17'	38° 22'	31° 0'	25° 2'	20° 19'	13° 47'	9° 48'
β_o	98° 8'	92° 39'	84° 51'	73° 24'	63° 59'	56° 21'	45° 8'	37° 33'
$\theta/2$	23° 20'	21° 39'	19° 11'	15° 30'	12° 31'	10° 10'	6° 54'	4° 54'
β'	74° 48'	71° 1'	65° 40'	57° 54'	51° 29'	46° 12'	38° 15'	32° 36'
t_m/c	0.12	0.118	0.115	0.11	0.105	0.10	0.09	0.08

TABLE 9

VORTEX STATOR BLADE ANGLE CALCULATIONS

ASSUMPTIONS: $\bar{r}$ HUB = 0.60000, $\bar{r}_2$ = 0.40000, $\bar{r}_{2'}$ = 0.45000, $\bar{r}_1$ = 0.70000, C_a = 0.98000, $\frac{1}{\bar{r}_1}$ = 2.2222, $\frac{c_2 - \bar{r}_{2'}}{2}$ = 0.14500, $\frac{c_1 - \bar{r}_{2'}}{2}$ = 0.34500, $\frac{2\pi \times \bar{r}}{N} = \frac{2\pi \times 36}{32}$ = 3.53572

SECTION	VIII	V	III	II	I
$\bar{r}$	0.60000	0.70000	0.80000	0.90000	1.0000
$1/\bar{r}$	1.6666	1.4286	1.2500	1.1111	1.0000
λ_1	0.24167	0.20715	0.18125	0.16111	0.14500
λ_2	0.57498	0.49287	0.43125	0.38333	0.34500
$\bar{r} - \lambda_1$	0.25833	0.49285	0.61875	0.73889	0.85500
$\bar{r} - \lambda_2$	0.02502	0.20715	0.36875	0.51667	0.65500
$\cot \gamma_1$	0.55704	0.46033	0.40277	0.35802	0.32222
$\cot \gamma_2$	1.27772	1.03526	0.95832	0.85184	0.76666
c	2.20000	2.4000	2.6000	2.8000	3.0000
s	2.12432	2.47500	2.82858	3.18215	3.53572
s/c	0.965600	1.031250	1.087915	1.136482	1.178573
$0.26\sqrt{s/c}$	0.25558	0.26416	0.27118	0.27716	0.28236
γ_1 (EXIT)	61° 46'	65° 17'	68° 4'	70° 18'	72° 8'
γ_2 (ENTRANCE)	38° 3'	42° 24'	46° 13'	49° 34'	52° 31'
$\theta°$	23° 43'	22° 53'	21° 51'	20° 44'	19° 37'
$1 - 0.26\sqrt{s/c}$	0.74442	0.73584	0.72882	0.72284	0.71764
$\sqrt{s/c}$	0.983	1.016	1.043	1.066	1.086
θ	31° 53'	31° 8'	29° 59'	28° 41'	27° 20'
γ_e	69° 56'	73° 30'	76° 12'	78° 15'	79° 51'
$\theta/2$	15° 57'	15° 33'	14° 59'	14° 21'	13° 40'
γ	54° 0'	57° 57'	61° 12'	63° 55'	66° 11'
t_m/c	.10	.10	.10	.10	.10

TABLE 10

SOLID BODY ROTOR BLADE ANGLE CALCULATIONS

ASSUMPTIONS: $\bar{r}_{HUB} = 0.60000$, $\bar{\psi}_a = 0.40000$, $\bar{\phi}_a = 0.45000$, $\bar{r}_1 = 0.80000$, $\lambda_1 = 0.26000$

$\alpha = 0.32500$, $k_1 = 0.34800$, $k_2 = 0.29800$, $\pi D/N = 3.7699$

SECTION	VIII	VII	VI	V	IV	III	II	I
$\bar{r}$	0.60000	0.62000	0.65000	0.70000	0.75000	0.80000	0.90000	1.00000
$\lambda_1 = \alpha \bar{r}$	0.19500	0.20150	0.21125	0.22750	0.24375	0.26000	0.29250	0.32500
$\lambda_2 = \bar{\psi}_a/2\bar{r} + \lambda_1$	0.52833	0.52408	0.51894	0.51321	0.51042	0.51000	0.51472	0.52500
$\phi_1 = \sqrt{k_1 - 2\alpha^2\bar{r}^2}$	0.52150	0.51654	0.50868	0.49446	0.47872	0.46131	0.42058	0.36980
$\phi_2 = \sqrt{k_2 - 2\bar{\psi}_a\alpha\ln\bar{r} - 2\alpha^2\bar{r}^2}$	0.59425	0.58405	0.56636	0.53595	0.50398	0.46991	0.39280	0.29454
$\bar{r} - \lambda_1$	0.40500	0.41850	0.43875	0.47250	0.50625	0.54000	0.60750	0.67500
$\bar{r} - \lambda_2$	0.07167	0.09592	0.13106	0.18679	0.23958	0.29000	0.38528	0.47500
$\tan\beta_1 = \phi_1/(\bar{r} - \lambda_1)$	1.2876	1.2343	1.1594	1.0465	0.94562	0.85428	0.69231	0.54785
$\tan\beta_2 = \phi_2/(\bar{r} - \lambda_2)$	8.2915	6.0889	4.3124	2.8693	2.1036	1.6204	1.0195	0.62008
C	2.6000	2.6400	2.7000	2.8000	2.9000	3.0000	3.2000	3.4000
$S = \pi D/N \times \bar{r}$	2.2619	2.3373	2.4504	2.6389	2.8274	3.0159	3.3929	3.7699
S/C	0.86996	0.88534	0.90756	0.94246	0.97403	1.0053	1.0603	1.1088
$\sqrt{S/C}$	0.93272	0.94092	0.95266	0.97080	0.98692	1.0026	1.0297	1.0530
$.26\sqrt{S/C}$	0.24251	0.24464	0.24769	0.25241	0.25660	0.26068	0.26772	0.27378
$1 - .26\sqrt{S/C}$	0.75749	0.75536	0.75231	0.74759	0.74340	0.73932	0.73228	0.72622
β_1 (Ent. $\angle$)	52°10'	50° 59'	49° 13'	46° 18'	43° 24'	40° 30'	34° 42'	28° 43'
β_2 (Exit $\angle$)	83° 7'	80° 40'	76° 57'	70° 47'	64° 34'	58° 19'	45° 33'	31° 48'
$\theta^{(0)} = \beta_2 - \beta_1$	30° 57'	29° 41'	27° 44'	24° 29'	21° 10'	17° 49'	10° 51'	3° 5'
$\theta_h = \theta^{(0)}/(1 - .26\sqrt{S/C})$	40° 52'	39° 18'	36° 52'	32° 45'	28° 28'	24° 6'	14° 49'	4° 15'
$\beta_c = \beta_1 + \theta_h$	93° 2'	90° 17'	86° 5'	79° 3'	71° 52'	64° 36'	49° 31'	32° 58'
$\theta_h/2$	20° 26'	19° 39'	18° 26'	16° 23'	14° 14'	12° 3'	7° 25'	2° 8'
$\beta = \beta_1 + \theta_h/2$	72° 36'	70° 38'	67° 39'	62° 41'	57° 38'	52° 33'	42° 7'	30° 51'

TABLE 11

SOLID BODY STATOR BLADE ANGLE CALCULATIONS

ASSUMPTIONS: $\bar{f}_{HUB} = 0.60000$, $\bar{\psi}_d = 0.40000$, $\bar{\phi}_d = 0.45000$, $f_1 = 0.80000$, $\lambda_1 = 0.26000$, $\alpha = 0.32500$, $k_1 = 0.34800$, $k_2 = 0.29800$, $\pi D/N = 3.53429$

SECTION	VIII	V	III	II	I
$\bar{f}$	0.60000	0.70000	0.80000	0.90000	1.00000
λ_1	0.19500	0.22750	0.26000	0.29250	0.32500
λ_2	0.52833	0.51321	0.51000	0.51472	0.52500
ϕ_1	0.52150	0.49446	0.46131	0.42058	0.36980
ϕ_2	0.59425	0.53595	0.46991	0.39280	0.29454
$\tan\gamma_1 = \phi_1/\lambda_1$	2.6744	2.1735	1.7743	1.4379	1.1379
$\tan\gamma_2 = \phi_2/\lambda_2$	1.1248	1.0443	0.92140	0.76313	0.56104
C	2.2000	2.4000	2.6000	2.8000	3.0000
$S = \pi D/N \times \bar{f}$	2.1206	2.4740	2.8274	3.1809	3.5343
S/C	0.06391	1.0308	1.0875	1.1360	1.1781
$\sqrt{S/C}$	0.98180	1.0153	1.0434	1.0658	1.0854
$.26\sqrt{S/C}$	0.25527	0.26398	0.27128	0.27711	0.28220
$1 - .26\sqrt{S/C}$	0.74473	0.73602	0.72872	0.72289	0.71780
γ_1 (EXIT ∠)	69° 30'	65° 18'	60° 36'	55° 11'	48° 41'
γ_2 (ENT. ∠)	48° 22'	46° 15'	42° 40'	37° 21'	29° 18'
$\theta^{(o)} = \gamma_1 - \gamma_2$	21° 8'	19° 3'	17° 56'	17° 50'	19° 23'
$\theta_S = \theta^{(o)}/(1-.26\sqrt{S/C})$	28° 23'	25° 53'	24° 37'	24° 42'	27° 0'
$\gamma_\varepsilon = \gamma_2 + \theta_S$	76° 45'	72° 8'	67° 17'	62° 3'	56° 18'
$\theta_S/2$	14° 12'	12° 57'	12° 19'	12° 21'	13° 30'
$\gamma = \gamma_\varepsilon + \theta_S/2$	62° 34'	59° 12'	54° 59'	49° 42'	42° 48'

TABLE 12

FREE VORTEX BLADING - FLOW THROUGH STATOR

AVERAGE FLOW COEFFICIENT: $\bar{\phi} = 0.35$

SAMPLE CALCULATIONS, USING CONSTANT'S RULE FOR THE DETERMINATION OF THE LEAVING ANGLES

1	ξ	0.600	0.700	0.800	0.900	1.000
2	λ_2	.583	.550	.516	.479	.444
3	ϕ_2	.304	.327	.347	.367	.382
4	$\lambda_2^2 + \phi_2^2$	.432	.410	.387	.364	.343
5	$\frac{1}{2}\frac{d}{d\xi}(\lambda_2^2+\phi_2^2)$	-.110	-.110	-.110	-.109	-.099
6	$[5]+\lambda_2^2/\xi = F$	.457	.323	.223	.145	.098
7	F/ϕ_2	1.502	.988	.643	.396	.257
8	γ_1	61.8	65.3	68.1	70.3	72.1
9	$(\cos^2\gamma_1)/\xi$	.3723	.2494	.1739	.1262	.0945
10	$\int[9]\,d\xi$	.0000	.0304	.0514	.0662	.0770
11	$e^{[10]}$	1.000	1.031	1.053	1.068	1.080
12	$\sin\gamma_1$	.881	.909	.928	.942	.952
13	$[11]\sin\gamma_1 \times F/\phi_2$	1.325	.926	.628	.398	.264
14	$\int[13]\,d\xi$	.0000	.1126	.1898	.2455	.2777
15	$(\sin\gamma_1)/[11] = B$	.881	.881	.881	.881	.881
16	$[14]\times[15] = A$	.0000	.0994	.1670	.2315	.2445
17	κB	.188	.188	.188	.188	.188
18	$A+\kappa B = \phi_3$	.188	.287	.355	.402	.433
19	$\phi_3 \cot\gamma_1 = \lambda_1$	.107	.132	.143	.144	.140

K IS CALCULATED FROM:

$$\int_{\xi_0}^{\xi_1} \phi_3 \xi\, d\xi = \int_{\xi_0}^{\xi_1} (A+\kappa B)\xi\, d\xi = \int_{\xi_0}^{\xi_1} A\xi\, d\xi + \kappa \int_{\xi_0}^{\xi_1} B\xi\, d\xi = \bar{\phi}\int_{\xi_0}^{\xi_1} \xi\, d\xi = .1120$$

$$\kappa = \frac{.1120 - \int_{\xi_0}^{\xi_1} A\xi\, d\xi}{\int_{\xi_0}^{\xi_1} B\xi\, d\xi} = \frac{.1120 - .0519}{.282} = .213$$

NUMERICAL INTEGRATIONS DONE BY SIMPSON'S RULE AND GRAPHICALLY.

TABLE 13

FREE VORTEX BLADING - FLOW THROUGH STATOR

AVERAGE FLOW COEFFICIENT: $\bar{\phi} = 0.35$

SAMPLE CALCULATIONS, USING CASCADE TRANSFORMATION FOR THE DETERMINATION OF THE LEAVING ANGLES

1	ξ	0.6	0.7	0.8	0.9	1.0
2	λ_2	.624	.560	.502	.459	.404
3	ϕ_2	.343	.351	.357	.357	.362
4	$\lambda_2^2+\phi_2^2$	.508	.437	.379	.337	.294
5	$\frac{1}{2}\frac{d}{d\xi}(\lambda_2^2+\phi_2^2)$	-.425	-.350	-.250	-.200	-.175
6	$[5]+\lambda_2^2/\xi = F$	.225	.099	.065	.033	-.012
7	$\phi_2/\lambda_2 = \tan\gamma_2$	.551	.627	.711	.778	.895
8	γ_2	28.9	32.0	35.4	37.9	41.8
9	γ_1	65.0	67.3	69.2	71.1	72.7
10	$(\cos^2\gamma_1)/\xi$	.297	.213	.157	.117	.088
11	$\int[10]\,d\xi$	0	.0249	.0431	.0568	.0670
12	$e^{[11]}$	1	1.025	1.044	1.058	1.069
13	$[12]\sin\gamma_1 \times F/\phi_2$	.595	.266	.178	.093	-.0336
14	$\int[13]\,d\xi$	0	.0400	.0616	.0756	.0790
15	$(\sin\gamma_1)/[11] = B$	.906	.900	.895	.894	.890
16	$[14]\times[15] = A$	0	.0360	.0552	.0676	.0703
17	KB	.299	.297	.295	.295	.294
18	$A+KB = \phi_3$	.299	.333	.350	.363	.364

K IS CALCULATED FROM:

$$\int_{\xi_0}^{\xi_1}\phi_3\,\xi\,d\xi = \int_{\xi_0}^{\xi_1}(A+KB)\,\xi\,d\xi = \int_{\xi_0}^{\xi_1}A\xi\,d\xi + K\int_{\xi_0}^{\xi_1}B\xi\,d\xi = \bar{\phi}\int_{\xi_0}^{\xi_1}\xi\,d\xi = .1120$$

$$\therefore\quad K = \frac{.1120-\int_{\xi_0}^{\xi_1}A\xi\,d\xi}{\int_{\xi_0}^{\xi_1}B\xi\,d\xi} = \frac{.1120-.0169}{.288} = .330$$

NUMERICAL INTEGRATIONS DONE BY SIMPSON'S RULE AND GRAPHICALLY.